

UNIVERSITY OF SOUTHERN QUEENSLAND
FACULTY OF ENGINEERING AND SURVEYING

DEVELOPMENT OF AN
ELECTRONICALLY CONTROLLED
THRUSTER

A DISSERTATION SUBMITTED BY

DOUGLAS JAMES JESSHOPE

IN FULFILMENT OF THE REQUIREMENTS OF

COURSE ENG4111 AND 4112 RESEARCH
PROJECT

TOWARDS THE DEGREE OF

BACHELOR OF ENGINEERING (MECHANICAL) /
BACHELOR OF SCIENCE (PHYSICS)

SUBMITTED: OCTOBER, 2012

Abstract

The aim of this project was to investigate the aerodynamic and structural effects of modifying a Carbon Fibre Toyota Supra TRD 3000 GT Wing to perform dynamic angle of attack updates. These angular updates have been based on an ideal aerodynamic phenomena required under different operating conditions. High speed cornering would see the wing produce maximum downforce, while heavy braking can be enhanced by using the wing blade to create maximum drag.

The realizable $k - \varepsilon$ turbulence model was used in a two dimensional representation of the problem within ANSYS FLUENT. This analysis determined that for all speeds, maximum downforce was achieved at a -15° angle of attack. Maximum drag occurred on the wing when it was deployed at -60° , while minimum drag was achieved at 0° .

The magnitudes of the forces obtained from the FLUENT analysis were then compared to data released for the standard Toyota Supra wing. This comparison showed that the downforce was increased by 46.97% over the standard wing.

A near field strain analysis was performed in order to ensure that the carbon fibre wing was capable of withstanding the added forces. An existing wing was loaded with weights in a fibre composite laboratory, while strain gauges measured the amount of strain present in the surface fibres.

Computer based finite element analysis was then used to conform to these strain values. Once the computer model demonstrated the same properties as the real specimen, it was loaded with the maximum FLUENT forces which determined that the wing blade had the ability to operate under the new conditions.

University of Southern Queensland
Faculty of Engineering and Surveying

ENG4111 & ENG4112 Research Project

Limitations of Use

The Council of the University of Southern Queensland, its Faculty of Engineering and Surveying, and the staff of the University of Southern Queensland, do not accept any responsibility for the truth, accuracy or completeness of material contained within or associated with this dissertation.

Persons using all or any part of this material do so at their own risk, and not at the risk of the Council of the University of Southern Queensland, its Faculty of Engineering and Surveying or the staff of the University of Southern Queensland.

This dissertation reports an educational exercise and has no purpose or validity beyond this exercise. The sole purpose of the course "Project and Dissertation" is to contribute to the overall education within the student's chosen degree programme. This document, the associated hardware, software, drawings, and other material set out in the associated appendices should not be used for any other purpose: if they are so used, it is entirely at the risk of the user.

Professor Frank Bullen

Dean

Faculty of Engineering and Surveying

Certification

I certify that the ideas, designs and experimental work, results, analyses and conclusions set out in this dissertation are entirely my own effort, except where otherwise indicated and acknowledged

I further certify that the work is original and has not been previously submitted for assessment in any other course or institution, except where specifically stated.

Douglas James Jesshope

Student Number: 0050086431

Signature

Date

Acknowledgements

I would like to acknowledge the following for their invaluable support and guidance throughout the course of this project:

- Dr Jayantha Epaarachchi, for his supervision of the overall project objectives and for his expert advice pertaining to the strain analysis section of the project.
- Dr Andrew Wandel, for his insight into the theory behind Computational Fluid Dynamics and for his generous support in developing a functioning model.
- Dr Ruth Mossad, for her advice on the reliability of the different $k - \epsilon$ models and general support provided in passing.
- Chris and Vicki Jesshope for their kind assistance in proof-reading this document.

Contents

ABSTRACT	I
CERTIFICATION	III
ACKNOWLEDGEMENTS	IV
LIST OF FIGURES	VII
LIST OF TABLES	X
1 INTRODUCTION	1
1.1 BACKGROUND	1
1.2 SCOPE AND OBJECTIVES OF PROJECT	1
1.3 RISK ASSESSMENT	3
1.4 CONSEQUENTIAL EFFECTS	4
1.4.1 Sustainability Issues	4
1.4.2 Ethical Issues	4
1.5 RESOURCE REQUIREMENTS	5
2 LITERATURE REVIEW	6
2.1 AERODYNAMICS OF ROAD VEHICLES	6
2.1.1 Drag	6
2.1.2 Lift	10
2.2 EFFECTS OF REAR WINGS ON VEHICLE DYNAMICS	13
2.3 ACTIVE AERODYNAMIC AIDS	16
2.4 COMPUTATIONAL FLUID DYNAMICS	19
2.3.1 The $k - \epsilon$ Turbulence Model	21
2.3.1.1 The Standard $k - \epsilon$ Model	22
2.3.1.2 The Renormalisation Group $k - \epsilon$ Model	24
2.3.1.3 The Realizable $k - \epsilon$ Model	25
2.3.2 The $k - \omega$ Turbulence Model	26
3 METHODOLOGY – 3D MODELLING	27
3.1 PRELIMINARY WORK	27
3.2 DEVELOPING THE WING GEOMETRY	28
3.3 DEVELOPING THE VEHICLE GEOMETRY	30
3.4 PROHIBITING FACTORS	38

4 METHODOLOGY – 2D FLUID DYNAMICS MODEL.....	39
4.1 DEVELOPING THE MODEL GEOMETRY	39
4.2 MESHING THE DOMAIN	43
4.3 MODELLING THE FLOW	47
4.3.1 <i>The FLUENT Launcher</i>	47
4.3.2 <i>Problem Setup - General</i>	47
4.3.3 <i>Problem Setup - Models</i>	48
4.3.4 <i>Problem Setup – Materials & Cell Zone Conditions</i>	50
4.3.5 <i>Problem Setup – Boundary Conditions</i>	50
4.3.6 <i>Problem Setup – Reference Values</i>	53
4.3.7 <i>Solution Setup</i>	54
5 METHODOLOGY - STRESS ANALYSIS OF WING BLADE.....	57
5.1 MATERIAL SELECTION.....	57
5.2 NEAR FIELD STRAIN MAPPING OF EXISTING WING BLADE.....	58
5.3 FINITE ELEMENT ANALYSIS OF WING BLADE.....	63
6 RESULTS AND DISCUSSION	67
6.1 COMPUTATIONAL FLUID DYNAMICS RESULTS	67
6.1.1 <i>Maximum Downforce Angle</i>	67
6.1.2 <i>Maximum Drag Angle</i>	73
6.1.3 <i>Minimum Drag Angle</i>	76
6.2 DYNAMIC EFFECT OF CHANGES.....	79
6.3 MATERIAL PERFORMANCE.....	82
6.3.1 <i>Near Field Strain Analysis</i>	82
6.3.2 <i>Finite Element Analysis</i>	83
7 CONCLUSION	86
7.2 FURTHER WORK.....	87
8 REFERENCES	89
APPENDIX A – PROJECT SPECIFICATION	91
APPENDIX B – RAW FLUENT DATA	92
APPENDIX C – DEVELOPMENT OF FORCES PER VELOCITY	96
APPENDIX D – NEAR FIELD STRAIN RESULTS.....	107
APPENDIX E – FIBRE COMPOSITE PROPERTIES	109

List of Figures

Figure 2.1 – Vehicle Frontal Area (Hucho 1987).	7
Figure 2.2 – Typical C_D Values for Common Cross Sections (Benson 2010).	8
Figure 2.3 – Flow Separation Comparison for Common Cross Sections.	8
Figure 2.4 – The Evolution of Vehicle Aerodynamics (Hucho 1987).	9
Figure 2.5 – The Effect of a Spoiler on Turbulence (Damjanović et al 2010).	12
Figure 2.6 – The Effect of a Spoiler on Drag and Lift (Hucho 1987).	12
Figure 2.7 – The Standard Toyota Supra Rear Wing.	13
Figure 2.8 – The 1955 Mercedes SLR at Le Mans.	16
Figure 2.9 – The Bugatti Veyron 16.4 and its Airbrake at 55°	17
Figure 2.10 – The Aeromotions S2 Wing with Centreplate.	18
Figure 2.11 – Boundary Layer Development on a Flat Plate.	25
Figure 3.1 – The Sketched Wing Profile.	28
Figure 3.2 – The SolidWorks Sketches.	29
Figure 3.3 – The Final Wing Model.	29
Figure 3.4 – The Initial JZA80 Supra Model.	30
Figure 3.5 – The Alias Wavefront OBJ Format.	31
Figure 3.6 – Quadratic Edge Collapse Decimation.	33
Figure 3.7 – 19,999 Face Mesh in MeshLab.	33
Figure 3.8 – 19,999 Face Part in SolidWorks.	34
Figure 3.9 – The Rhinoceros T-Splines Model.	35
Figure 3.10 – The T-Splines Function.	35
Figure 3.11 – Non-Manifold Edges.	36
Figure 3.12 – The Rhinoceros ‘NURBS’ Model.	37

Figure 3.13 – Gaps between Faces.	37
Figure 4.1 – Blueprints of the 1996-2002 Toyota Supra.	39
Figure 4.2 – The 2D SolidWorks Assembly Model.	40
Figure 4.3 – The 2D Flow Model Domain (L = 4514mm).	41
Figure 4.4 – The Overlapping STEP Imports.	42
Figure 4.5 – The Final Domain.	43
Figure 4.6 – The Vehicle Mesh.	46
Figure 4.7 – The Named Selections.	46
Figure 4.8 – The Model Menu.	48
Figure 4.9 – Contours of Y^+ in the Standard Wall Function Model.	49
Figure 4.10 – Defining the Inlet Conditions.	51
Figure 4.11 – Convergence of Scaled Residuals (818 iterations).	55
Figure 4.12 – Resultant Forces on Relevant Zones.	56
Figure 5.1 – Strain Gauge Locations – Upper Wing Surface.	59
Figure 5.2 – Strain Gauge Locations – Lower Wing Surface.	60
Figure 5.3 – Wire Structure for Gauge 3.	60
Figure 5.4 – The Strain Testing Assembly.	61
Figure 5.5 – The Half Bridge Connection.	62
Figure 5.6 – Isotropic verses Orthotropic.	63
Figure 5.7 – The Wing Mesh.	64
Figure 5.8 – The Ply Properties.	64
Figure 5.9 – The Laminate Properties.	65
Figure 5.10 – The Load Case.	66
Figure 6.1 – Force versus Wing Angle (70 m/s).	68
Figure 6.2 – Velocity Vectors Coloured By Static Pressure (Pascal).	69

Figure 6.3 – Velocity Vectors Coloured By Static Pressure (Pascal).	69
Figure 6.4 – Addition of Wheels to a car-like body (Hucho 1987 p165).	70
Figure 6.5 – Velocity Vectors Coloured By Velocity (m/s).	70
Figure 6.6 – Velocity Vectors Coloured By Velocity (m/s).	71
Figure 6.7 – Pathlines of Turbulent Intensity (%).	71
Figure 6.8 – The Maximum Downforce Wing Angle Forces (-15°).	72
Figure 6.9 – Velocity Vectors Coloured By Static Pressure (Pascal).	73
Figure 6.10 – Velocity Vectors Coloured By Static Pressure (Pascal).	74
Figure 6.11 – Velocity Vectors Coloured By Velocity (m/s).	74
Figure 6.12 – Pathlines of Turbulent Intensity (%).	75
Figure 6.13 – The Maximum Drag Wing Angle Forces (-60°).	75
Figure 6.14 – Velocity Vectors Coloured By Velocity (m/s).	76
Figure 6.15 – The Maximum Drag Wing Angle Forces (0°).	77
Figure 6.16 – Pathlines of Turbulent Intensity (%).	77
Figure 6.17 – Comparison of Vehicle Drag Forces.	78
Figure 6.18 – Strand7 Strain Plot (55 lb. Load).	83
Figure 6.19 – Strand7 Strain Plot (1337 N Load).	84
Figure 6.20 – Strand7 Displacement Plot (1337 N Load).	85

List of Tables

Table 1.1 – Details of Risk Assessment.	3
Table 3.1 – JZA80 Toyota Supra Specifications.	27
Table 3.2 – TRD 3000GT Wing Dimensions.	27
Table 4.1 – Span Angle Centre.	45
Table 4.2 – The Mesh Settings.	46
Table 4.3 – Reference Values.	53
Table 4.4 – Solution Methods.	54
Table 4.5 – Residual Monitors.	55
Table 5.1 – Selected Strain Gauges.	58
Table 6.1 – Wing Angle Data at 70 m/s.	68
Table 6.2 – Minimum Corner Radius Decrease (40.3 m/s).	81
Table 6.3 – Minimum Corner Radius Decrease (70 m/s).	81
Table 6.4 – Strain Measured Within Wing Blade (55 lb.).	82
Table 6.5 – Strain Comparison of Wing Blades (55 lb.).	84
Table 7.1 – Summary of Critical Angles.	86

1 Introduction

1.1 Background

The Toyota Supra JZA80 is an iconic Japanese sports car and was produced from 1993 to 2002 in a range of trim levels. One of these trim levels included an addition of an active aerodynamic front lip spoiler that deploys at speeds in excess of 80km/h in order to improve the flow profile over the car. This project is aimed at complimenting the effects of this spoiler with the addition of an active rear wing that can be manipulated to enhance the performance of the car.

The project objectives, shown below in Section 1.2, outline the critical deflection angles for an active spoiler such as this. Obtaining wing angles that correlate to maximum and minimum drag forces over a range of vehicle velocities is paramount to the success of this project. In theory, a wing deployed at an angle that maximises drag will allow the car to brake more quickly than an identical vehicle with a standard wing angle. In a similar scenario, a wing deployed at an angle that produces minimum drag will allow the car to travel at a higher top speed than a car without that ability.

This project will explore both scenarios and determine if the magnitude of the calculated gains justifies the application of an active rear spoiler on a Toyota Supra. Furthermore, the methodology of this project will also examine the ability of the wing to increase the vehicles rear wheel tractive forces by providing downforce.

1.2 Scope and Objectives of Project

The scope of this project can be best outlined by separation into two sections, project scope and product scope. The project scope pertains to everything report related, detailing objectives and limitations for the report write-up. The product scope

encompasses the mathematical, experimental and computational analysis stages of the dissertation.

The following should be considered for the product scope:

- The wing shall actuate to achieve maximum total drag force
- The wing shall actuate to achieve minimum total drag force
- The wing shall actuate to achieve maximum down force
- The wing actuation must not impair driver's field of vision
- The final product must be designed to withstand increased stresses
- The wing exterior profile shall be unchanged from the TRD 3000GT Model

With the preceding comments in mind, the objectives for the product aspect of the dissertation will be to:

- Create a dimensionally accurate 2D CAD profile of the supra body
- Append a 2D CAD profile of the TRD wing at a large range of attack angles
- Perform 2D aerodynamic simulations on the model to obtain proof of concept
- Develop an accurate 3D CAD TRD wing model
- Perform FEA on the 3D wing to in order determine actuation stresses.
- Experimentally calibrate/confirm model accuracy using strain gauges.

Coinciding with the product objectives are the project objectives. These are outlined below and serve to improve the accuracy of the product objective results by exploring the successes and errors of similarly scoped projects. These objectives are:

- Research general automotive aerodynamics, including current airbrake designs
- Research 2D & 3D Fluent modelling platforms and select a suitable analysis
- Research the materials commonly used in relevant aerodynamic applications
- Research vehicle dynamics and apply concepts accordingly

1.3 Risk Assessment

As with any engineering project, there are risks involved with the execution of the project and product objectives. The observed and foreseen risks have been tabulated below in order to rank their severity and offer methods of controlling, eliminating or minimising the risks.

Table 1.1 – Details of Risk Assessment

Description of Hazard	Persons at Risk	Risk Severity	Exposure to Risk	Consequences	Control Measures Taken
Eyesight damage, due to long hours spent sitting at computer desk	Myself	Slight	Frequently	Minor Injury	Avoid staring at the screen, Adjust brightness accordingly, Take 5 minute break every 60 minutes.
Injury sustained from incorrect re-assembly of external vehicle body components.	Public	Very Slight	Rarely	Major Injury/Possible Death	Avoid working when overtired; Never work on the car alone. Double-check components are secure
Repetitive Strain injury to fingers from typing	Myself	Substantial	Frequently	Minor Injury	Ensure fingers are warm and adequately stretched; Take 5 minute break every 60 minutes.
Damage to HDD and other PC Components from continuous load	Personal Computer	Significant	Continuously	Major Component Damage	Simulate processes according to ANSYS specified requirements. Regularly back-up work
Blunt force injury resulting from weights dropping from testing stands	Myself, others in laboratory	Significant	Rarely	Bruising, broken skin, broken bones	Follow WH&S Protocol in P2 Laboratory, wear safety boots, maintain clearance about weights
Inhaling of toxic fumes whilst soldering	Myself	Significant	Rarely	Damage to blood-forming, nervous & reproductive systems	Follow WH&S Protocol, wear a breathing mask when appropriate, ensure fumes can escape local proximity.
Super glued digits whilst applying strain gauges	Myself	Minor Injury	Rarely	Skin Damage	Ensure plastic aids are used to apply pressure to glued components when necessary.

1.4 Consequential Effects

1.4.1 Sustainability Issues

The product deliverable will ultimately be designed to leech electrical power from the vehicles electrical energy reserves. As such, the sustainability of running such an item shall be weighted against the amount of electrical power it consumes. Design of the electronic components should be based about electrical efficiency in order to prevent a permanent drain that exceeds the alternators regeneration capacity.

Also, the addition of aftermarket wiring into a genuine production car loom could produce problems with genuine features within range of the proposed system integration. Items such as tail lights and reverse lights should be tested post installation to ensure functionality until a fool proof wiring integration diagram is formulated.

1.4.2 Ethical Issues

The original TRD 3000GT wing for the Toyota Supra is a copyrighted item and it is therefore prohibited to manufacture and distribute replica wings under the TRD company banner, or imply that the product is associated with the company in any way. It must be clearly detailed at all stages from the initial design phase, through to the completion of a prototype wing, that the active rear wing is an aftermarket replica.

Before constructing a wing for public demonstration or sale it is necessary to properly investigate the extent of the copyright associated with a genuine TRD wing. In the event that distinctive features such as the aerofoil geometries used for the original design are covered by patents or copyright, legal counsel should be sought.

It must also be considered that a vehicular performance enhancement such as this is likely, if not specifically designed to, catch the interest of public road users. As a result, sales of this item should be restricted to off road users unless the deliverable product complies with all relevant Australian design rules and regulations.

1.5 Resource Requirements

The product and project scope objectives are heavily computer based and the resource requirements reflect this. For the project aspect of the report, a substantial amount of literature that describe the modelling, fluid dynamic analysis and finite element analysis must be discovered, interpreted and appreciated. On top of the discoverable literature resources will be the task specific knowledge that my supervisors use to guide my progress throughout the task.

The product based resource requirements are more clearly defined. In order to model the car in the required 3D manner, access to the following software packages in essential.

- Autodesk 3DStudio
- MeshLab
- Autodesk Rhinoceros
- SolidWorks 2012
- ANSYS
- Strand7

Most of these are very memory intense applications and as such a computer capable of running these is also required. The project objectives utilized an Intel i7 processor and 8GB RAM which proved sufficient. The product objectives were limited to running on significantly slower dual core computers, which greatly impacted upon processing time.

Fluid dynamic software was required to run iterations of the model over several geometry changes. This required another ANSYS product called Fluent. The university computers were sufficient to model the 2D flow in a timely fashion. It is indicated in the reviewed literature that 3D analysis of fluid flow over a meshed car body is an extremely detailed process that exceeds the abilities of these computers.

Finally, several strain gauges and associated computers were required to experimentally evaluate the forces that act on the wing at certain load conditions in order to verify the accuracy of the computational models and determine the legitimacy of the project.

2 Literature Review

A literature review was performed in order to gain a solid understanding of the theoretical, computational and practical aspects of designing an aerodynamic based vehicle component. The sources included fluid mechanics textbooks, journal articles, driver's accounts, manufacturer's specifications and fluid mechanics reference material.

2.1 Aerodynamics of Road Vehicles

Road vehicles are subject to a large range of aerodynamic effects that can greatly alter the performance and stability of the vehicular motion. Aerodynamic drag, side wind stability and tail lift are unbalanced pressure forces that act upon the shell of the vehicle and alter the dynamics of motion.

2.1.1 Drag

Of the forces listed above, aerodynamic drag is the more prominent hindrance to motion. Drag is the force that acts directly opposite to the direction of motion and is caused by a combination of friction and viscous components. The viscous component is the result of turbulence created by the vehicle body and is the most significant component when considering vehicular motion. Hucho (1987, p2) states that at a speed of 100km/h, the aerodynamic drag resisting the forward motion of a mid-sized European car of that time was in order of 80% of the vehicles total road resistance.

As a result, vehicle aerodynamicists have since focussed on decreasing the aerodynamic drag incurred while designing new motor vehicles. The equation following describes the relationship between aerodynamic drag and vehicle speed.

$$F_d = c_D A \frac{\rho}{2} V^2 \quad (2.1)$$

where

F_d	=	Drag Force	(N)
C_d	=	Drag CoEfficient	
A	=	Frontal Area	(m^2)
ρ	=	Air Density	($kg.m^{-3}$)
V	=	Velocity	($m.s^{-1}$)

This shows that the drag force that acts on the vehicle is proportional to the frontal area (A), the pressure of the air (ρ), the vehicle velocity (V) and a vehicle shape factor (c_D) called the drag coefficient. As such, the critical factors for decreasing the overall drag of a vehicle are the frontal area and drag coefficient.

The frontal area is measured as the total two-dimensional area “seen” by a viewer from the front of the car. Car designers are quite restricted when it comes to reducing this area as the ergonomics of the driver and passenger seating positions define a large percentage of the total frontal shape. This restriction is shown below.

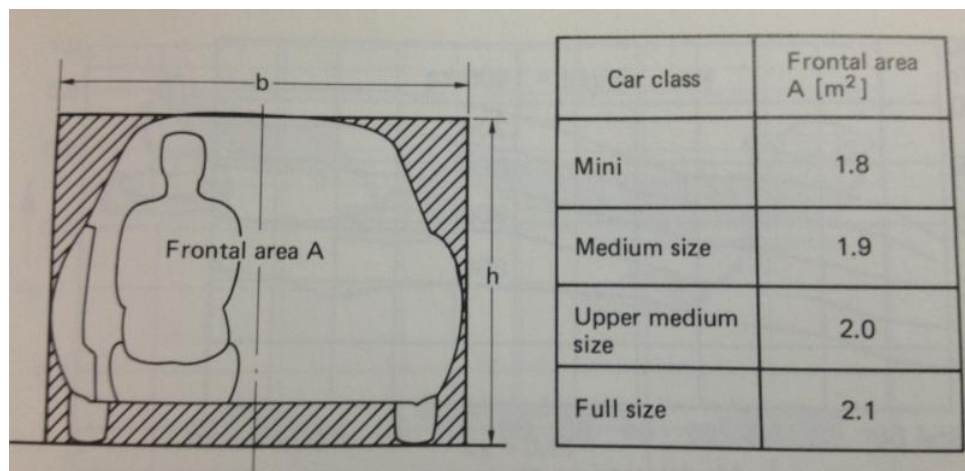


Figure 2.1 – Vehicle Frontal Area (Hucho 1987)

Therefore the most effective factor available to manipulate in Equation 2.1 is the vehicles drag coefficient. The drag co-efficient is a dimensionless factor that describes the magnitude of aerodynamic hindrance a bluff body has on the flow passing over it. The smaller the coefficient, the less air resistance that object will incur when traversing through the air.

Bluff objects with rapid geometry changes perpendicular to the flow direction, such as cubes, prisms and spheres, tend to have a high drag coefficient. Conversely, bluff objects such as aerofoils that have very small changes perpendicular to the flow direction have very small drag coefficients.



Figure 2.2 – Typical C_d Values for Common Cross Sections (Benson 2010)

Rapid changes in bluff object geometry result in separation of the flow field and the object surface. When a flow passes over a body, it attaches itself to the external contour of that shape and attempts to follow along the surface until its end. Rapid geometry changes prevent this by creating vacant zones, such as the on right hand side of the circular section below.

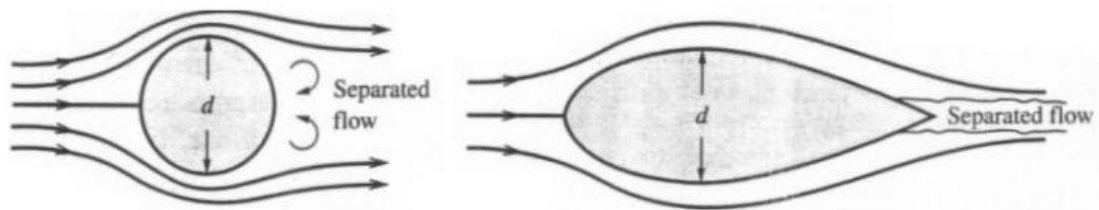


Figure 2.3 – Flow Separation Comparison for Common Cross Sections

This flow separation effect is the one of the main contributors to aerodynamic drag on motor vehicles. When the flow separates from the surface of the vehicle, pockets of air with near-atmospheric properties fill the void left between the surface and the streamlines. This air is generally turbulent and dramatically increases the drag force acting upon the vehicle.

Early motor vehicles were not designed with aerodynamics in mind and as a result they had very tall, largely angular passenger compartments. As aeronautic

technology advanced, the results slowly made their way across into the motor vehicle industry.

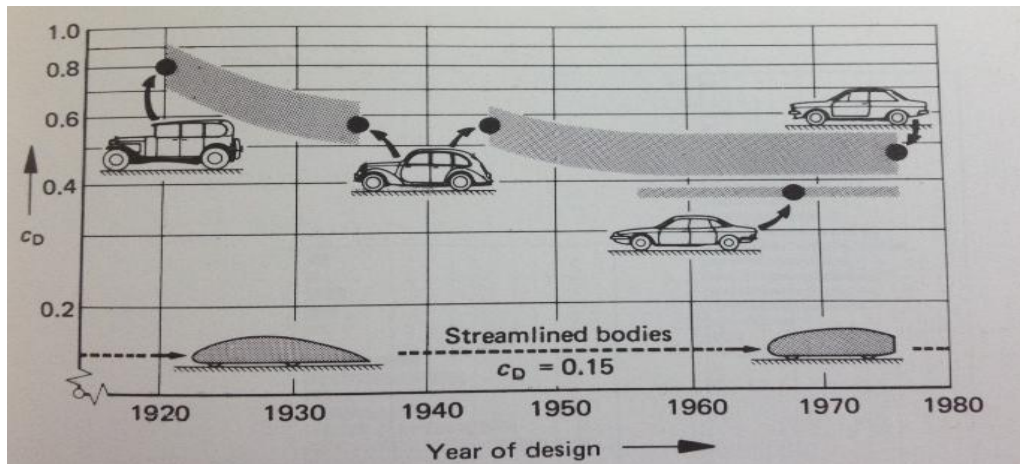


Figure 2.4 – The Evolution of Vehicle Aerodynamics (Hucho 1987)

As vehicles became faster, the aerodynamic effects on the body became more significant. As such, the tall, orthogonal body styles from the early 1920's were replaced with lowered and more streamlined designs by 1940 after the mainstream application of aerodynamic principles. Vertical windscreens were replaced with inclined examples that allowed the air flow to remain attached to the vehicle shell, resulting in significantly smaller drag coefficients.

The end of World War II brought about a new era in the development of aerodynamic shapes for vehicle design. Race engineers began experimenting with wind tunnels in order to evaluate the aerodynamic capabilities of their vehicles and aerodynamic components. These changes would eventually make their way into designs for production cars. The evolution of production cars continues to gain inspiration from competitive motorsport.

In recent years, the experimental testing of new concepts has been predominantly computer based now that the technology is available, however wind tunnels are still used for validation of computational results. These improvements have allowed the drag co-efficient of production vehicles to reach between 0.2 and 0.3, an incredible decrease when comparing to the corresponding vehicles made in the 1920's.

2.1.2 Lift

Lift is the force that acts perpendicular to the direction of vehicular motion. The lift force is similar to drag in that it is calculated from the velocity of motion and properties of the displaced fluid. In all cases, lift is measured upward with respect to the body according to the equation below.

$$F_L = c_L A \frac{\rho}{2} V^2 \quad (2.2)$$

<i>where</i>	F_L	=	<i>Lift Force</i>	(N)
	C_d	=	<i>Lift CoEfficient</i>	
	A	=	<i>Wing Area</i>	(m ²)
	ρ	=	<i>Air Density</i>	(kg.m ⁻³)
	V	=	<i>Velocity</i>	(m.s ⁻¹)

This phenomenon has a far smaller effect on production vehicles than drag as it has a very small magnitude at speeds below 100 km/h. Also, the lift force does not inhibit the motion of the vehicle. For this reason, most production vehicles do not employ aerodynamic aids that are specifically designed to develop a negative lift force. Most modern, road based vehicles use aerodynamic aids that decrease the lift co-efficient of the vehicle, while also decreasing the drag acting against the vehicle.

The name given to this common aerodynamic aid is a ‘Spoiler’. The addition of a spoiler essentially disrupts the flow over the rear end of the vehicle. The main effect of this is to spoil the high velocity nature of the airstream without increasing drag. This reduces the magnitude of the lift force created by the high velocity, low static pressure air according to Daniel Bernoulli’s equations for fluid in a streamline.

$$p + \frac{1}{2}\rho V^2 + \rho g z = Constant \quad (2.3)$$

<i>where</i>	p	=	<i>Static Pressure</i>	(Pa)
	ρ	=	<i>Fluid Density</i>	(kg/m ³)
	V	=	<i>Velocity</i>	(m/s)
	g	=	<i>Gravitational Acceleration</i>	(m/s ²)
	z	=	<i>Elevation</i>	(m)

The first term, static pressure, is measured by an instrument that is travelling with the flow. The second term is the dynamic pressure of the flow and the third term is

elevation pressure. In that case of a moving vehicle or aerofoil, it can be assumed that the elevation pressure is constant at all points along the streamline given that the elevation change will be negligible. This results in Equation 2.3.1

$$p + \frac{1}{2}\rho v^2 = Total\ Pressure \quad (2.3.1)$$

As such, when the velocity of a fluid flow increases, the static pressure that can be measured within that flow is decreased to satisfy the equation. Consider the case when a vehicle is travelling through a body of air at a constant total pressure.

The body of the air travelling along the upper side of the vehicle has significantly further to travel than the air travelling under the body. As the air on both sides of the vehicle had the same properties prior to being separated, they both have the same constant total pressure. The air that travels the furthest will be forced to accelerate to a higher velocity by the air particles that are behind it on the streamline. This faster moving air will now have a smaller static pressure value, as some of the pressure has been changed to dynamic pressure during the velocity increase. Therefore, there is a discrepancy between the static pressures of the air on the upper and lower side of the vehicle. A lift force results from this imbalance, as the high static pressure side pushes the vehicle upward, while the low static pressure side pulls the vehicle in the same upward direction.

Another effect of a spoiler is to prevent the flow from forming a large stagnant air pocket that would normally be created when the flow moves to fill the void left by the body. The act of diverting the airflow effectively increases the overall length of the vehicle and allows for a more steady integration of the vehicle airflow back into the free stream, greatly reducing drag.

Damjanović et al (2010) showed this effect quite well with the introduction of a spoiler aid to their conceptual car design. This turbulent intensity is greatly reduced at the rear of the car when the spoiler is added, with only a minor zone of turbulently intense air is created above the spoiler.

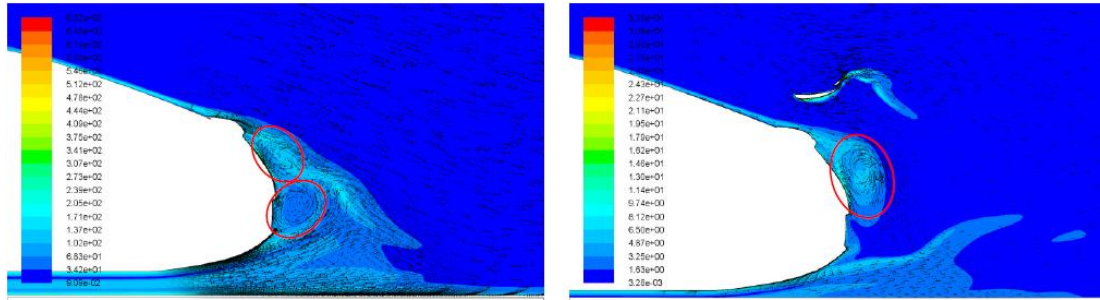


Figure 2.5 – The Effect of a Spoiler on Turbulence (Damjanović et al 2010)

The application of spoilers will have varying effects when different vehicles are considered, however the general consensus is that a correctly designed spoiler can have a dramatic effect on the drag and lift coefficients of a standard motor vehicle. Hucho (1987) showed this in his wind tunnel experiments on a Volkswagen 1600 coupe. He performed comparative testing on a number of simple aerodynamic attachments in order to gauge the effect that each had on the lift and drag forces. The results of this comparative testing to the overall lift and drag coefficients of the Volkswagen 1600 are shown below.

	c_D	c_L
A Basic configuration	0.34	0.38
B Rear spoiler	0.33	0.18

Figure 2.6 – The Effect of a Spoiler on Drag and Lift (Hucho 1987)

The lift coefficient of the vehicle was more than halved by the addition of the spoiler, while the drag coefficient also went down marginally due to the effect shown in Figure 2.5. Further research done by Wolf-Heinrich Hucho has shown that this overall vehicle lift co-efficient can be broken down and separated into wheel-axle specific coefficients in order to gauge the effect that lift forces have upon the front and rear reaction forces acting through the vehicles tyres.

2.2 Effects of Rear Wings on Vehicle Dynamics

Another common aerodynamic aid used on production vehicles is the rear wing. Often confused for a spoiler, a rear wing is actually an inverted aerofoil that is located further from the vehicle surface than a spoiler. This allows the aerofoil to interact with incoming air that has a more developed, consistent velocity.

The inverted aerofoil actually produces a localised negative lift force that pushes the rear of the car back down toward the road surface, negating the effects of the rear end lift discussed earlier. However, as a result of being employed higher within the flow, the aerofoil actually increases drag forces in many cases.



Figure 2.7 – The Standard Toyota Supra Rear Wing

An example of this rear wing attachment is the standard wing for the Toyota Supra. The cross section of this wing is a non-symmetrical inverted aerofoil with a significantly smaller vertical depth than the Toyota Racing Development replacement used in this analysis. Toyota released the aerodynamic figures relating to this wing shortly after the vehicle's release in 1993. According to their development data, the aerofoil added 66 lb. of negative lift force while the vehicle was progressing at 90 mph.

This equates to approximately 294 Newtons of downward force on the car at 145 km/h and acts directly against the rear end lift forces, pushing the rear tyres into the road surface. On Australian roads, this is much faster than the vehicle should be travelling, which means that the wing only produces a small proportion of the total

apparent vehicle mass at legal speeds. As such, the wing may provide extra stability during highway driving but it will not markedly increase the performance characteristics of the vehicle.

The addition of the rear wing to the Toyota Supra also increases the drag co-efficient of the vehicle from 0.31 to 0.33. This means that the incurred drag will increase by approximately 6.5% at all speeds, which is a significant increase when the car is not used off-road. However, if the car is used off road, the effects of the rear wing can greatly increase the downward forces at the rear of the vehicle. This is where the application of a rear wing can truly be justified.

Isaac Newton showed that a centre force acts upon a body in circular motion according to the following equation:

$$F_c = \frac{mV^2}{R} \quad (2.4)$$

<i>where</i>	F_c	=	<i>Centre Force</i>	(N)
	m	=	<i>Mass</i>	(kg)
	V	=	<i>Velocity</i>	(m/s)
	R	=	<i>Raadius of motion</i>	(m)

It is also known that a vehicle in motion can only use the frictional force to negate the outward push of the centre force. This friction force is the proportional to the coefficient of friction between the tyres and the road, while the normal force is the amount of upward reaction force pushing against the tyre.

That is:

$$F_{fric} = F_c \quad (2.5)$$

$$= \mu N$$

<i>where</i>	F_{fric}	=	<i>Friction Force</i>	(N)
	μ	=	<i>Coefficient of Friction</i>	
	N	=	<i>Normal Force</i>	(N)

<i>Therefore</i>	μN	=	$\frac{mV^2}{R}$	(2.6)
------------------	---------	---	------------------	-------

Equation 2.6 shows that for a vehicle turning a corner with a constant radius, velocity is directly proportional to the amount of normal force being applied to the vehicles tyres. At sufficient speeds, i.e. above 115 km/h, the downforce produced by the rear wing on a vehicle increases the normal force being applied to the tyres. This in turn increases the maximum speed at which the vehicle can travel around that corner.

This mathematical relationship is the basis for front and rear wing geometries being added to many classes of racing. The most elite of these racing classes is Formula 1, which allows its vehicles to employ numerous wing attachments. According to the Official F1 website (2012), modern Formula 1 vehicles are ‘capable of developing 3.5 g lateral cornering force thanks to aerodynamic downforce’.

However, this acceptance of increased grip through the use of aerodynamics has not been without critics. Sorensen et al (1999) showed the dramatic effect that increasing traction through the use of aerodynamics puts the drivers at risk of serious injury. Equation 11 of their paper states:

$$N = mg + F_{aero} \quad (2.7)$$

Through mathematical reasoning, they proceed to show that when a vehicle is travelling through a corner using increased tractive ability and vehicle control is lost, it spins and all of the aerodynamically added normal forces disappear. This results in the available friction force described in Equation 2.5 will decrease in the same proportions, assuming that the vehicle remains on the same type of ground. The work done by the friction force after control is lost is shown below:

$$W_{fric} = F_{fric} \times distance \quad (2.8)$$

This work is equivalent to the kinetic energy possessed by the spinning vehicle. This will only be changed minimally by the increased drag forces due to increased frontal area, so it can be assumed that this is constant for both cases. As such, the distance required in Equation 2.8 is greatly increased when the normal force component of the friction force is decreased. The conclusion that resulted was ‘if a car hits a barrier at some stage within this distance, the car will hit the car harder than a vehicle without aerodynamically enhanced abilities.

2.3 Active Aerodynamic Aids

The traditional approach to vehicle aerodynamics is to create a compromise between optimum performances in a certain number of scenarios. According to a release by Daimler-Chrysler (2012), the first person to implement an active aerodynamic aid on a vehicle was Alfred Neubauer when he developed the idea of an ‘airbrake’ in 1955. This concept was dreamt up by Neubauer, in his capacity at Mercedes’ Director of Motorsport, when he proposed it as a solution to overcome the excessive wear that occurred on the drum brakes of Mercedes 300 SLR Le Mans car.



Figure 2.8 – The 1955 Mercedes SLR at Le Mans

This brake is shown in Figure 2.8 and has an area of 0.7 m^2 . A hydraulic pump was used to deploy the brake when the car experienced heavy braking. The result was significant, with the brake increasing both the braking and cornering abilities of the vehicle.

Some of the first production vehicles to utilise active aerodynamic aids were the Volkswagen Corrado and the Lancia Thema from 1986. Rather than implementing a large braking aid like the Mercedes, these vehicles were designed with active rear spoilers. These spoilers are deployed electronically and act to reduce the drag acting on the vehicle when travelling at high speeds. This innovation was specifically aimed at improving the efficiency of the vehicles, rather than their sports based performances.

Several performance vehicles adopted active aerodynamic technology during the 1990's. Cars such as the Mitsubishi GTO VR4 (1991-1996), the Toyota Supra JZA80 (1995-2002) and the Nissan Skyline R32/R33 (1990-1998) all used active front spoilers that lowered below the front bumper in order to restrict the amount of air that could flow beneath the vehicle. This acted to reduce the amount of lift that was produced by high pressure systems beneath the vehicle.

The most infamous road vehicle to utilise an active aerodynamic aid is the Bugatti Veyron 16.4, released in 2005. It gained this status by becoming the first production vehicle to utilize an active aerodynamic aid that also acted as an airbrake. According to the manufacturer's website, when the Veyron is braking from very high speeds (above 200 km/h) the twin blade airbrake deploys at an angle of attack of 55°. This is shown below in Figure 2.9.



Figure 2.9 – The Bugatti Veyron 16.4 and its Airbrake at 55°

This action allows the Veyron to increase its rate of deceleration by 0.6 times Earth's gravitational pull, or 5.89 m/s^2 . To put this in perspective, that rate of deceleration is equivalent to the maximum deceleration felt by recently released small vehicle. While this addition may not prove particularly useful on a public roadway, it is an invaluable asset when used on a racetrack.

The design of this airbrake would prove difficult to reproduce when modifying a regular production vehicle. The complex hydraulic system that actuates the wing blade angles have been recessed into the rear hatch of the Bugatti, as shown in Figure

2.9. It would take a large amount of customised bodywork and manipulation of standard systems in order to retrofit the Supra with a design similar to this.

One company that recognised this fact was Aeromotions. A group of engineers from the Massachusetts Institute of Technology (MIT) developed an aftermarket dynamic rear wing for a Nissan R35 GTR through full vehicle computational fluid dynamics analysis. This allowed the company to use the MIT wind tunnel to develop an optimum blade design for high downforce and low drag forces.

The wing shown below is the Aeromotions S2 dynamic rear wing. It is constructed of high shear modulus carbon fibre and utilizes a centre plate to ensure that cross transfer of the flow cannot occur. Both the uprights and the mounting points have been moulded into teardrop shapes to minimise the drag that these features induce.



Figure 2.10 – The Aeromotions S2 Wing with Centreplate

The basic twin-turret design allows this model of wing to be retrofitted to many different vehicles with ease, while the high strength materials have allowed this wing to be approved for use in on public roads in several countries. The data speaks for itself, showing that this wing takes an average 2.29 seconds per lap off for a large range of vehicles on a track with an approximate two minute lap time.

The active version of the TRD wing should be based closely upon the geometry setup of this wing. The actuators should be hydraulic pistons that are located within the standard aerofoil shaped side turrets. Control boxes could then be located on the underside of the hatch, where wiring is already present.

2.4 Computational Fluid Dynamics

According to Bakker (2006) there are three equation forms that form the basis of computational fluid dynamics. The equations were derived from Euler's equations for the conservation of mass and momentum. These Navier-Stokes equations expand upon Euler's equations by allowing for the introduction of the fluid viscosity. The final equation used is the first law of thermodynamics that describes the conservation of energy.

The steady state equation for the conservation of mass states that the sum mass flux across Cartesian component boundaries within a control volume will be zero.

That is:

$$0 = \frac{\delta_u}{\delta_x} + \frac{\delta_v}{\delta_y} + \frac{\delta_w}{\delta_z} \quad (2.9)$$

The momentum equations apply Newton's second law of motion to each of the three dimensions and show that a change in particle momentum in a component direction will be balanced by equal and opposing changes to momentum in other directions. The equations shown below describe the conservation of momentum within a steady state reference frame.

That is:

$$M_x = \frac{\delta_u}{\delta_t} + \frac{\delta_{uu}}{\delta_x} + \frac{\delta_{uv}}{\delta_y} + \frac{\delta_{uw}}{\delta_z} \quad (2.10)$$

$$M_y = \frac{\delta_v}{\delta_t} + \frac{\delta_{uv}}{\delta_x} + \frac{\delta_{vv}}{\delta_y} + \frac{\delta_{vw}}{\delta_z} \quad (2.11)$$

$$M_z = \frac{\delta_w}{\delta_t} + \frac{\delta_{uw}}{\delta_x} + \frac{\delta_{vw}}{\delta_y} + \frac{\delta_{ww}}{\delta_z} \quad (2.12)$$

The conservation of energy equation demonstrates that energy can neither be created nor destroyed. It is merely transferred into a different form, ranging from kinetic, potential, light or heat to name a few. The Navier-Stokes representation of this principle that is specific to energy within fluid flow is shown below.

That is:

$$E = \frac{\delta_T}{\delta_t} + \frac{\delta_{uT}}{\delta_x} + \frac{\delta_{vT}}{\delta_y} + \frac{\delta_{wT}}{\delta_z} \quad (2.13)$$

Computational fluid dynamics programs can utilise all three of these Navier-Stokes equations in order to analyse the flow of a non-turbulent Newtonian fluid within a control volume. A fluid is classified as Newtonian if its properties satisfy the following equation.

$$\tau = \mu \frac{d_u}{d_y} \quad (2.14)$$

where $\tau = \text{Shear Stress} \quad (\text{Pa.s})$

$\mu = \text{Proportionality Constant} \quad (\text{Pa.s})$

$\frac{d_u}{d_y} = \text{Strain Rate (velocity gradient)} \quad (\text{s}^{-1})$

These equations are suited to the analysis used within the project, though they do not sufficiently describe the effect that turbulence can have on the flow field. As such, further equations need to be added to the analysis. There are several models available to model the turbulent flow of a Newtonian fluid. Each of these will be described in detail in the following sections.

2.3.1 The $k - \varepsilon$ Turbulence Model

The $k - \varepsilon$ turbulent model allows for the introduction two new equations that describe the turbulent nature of the flow. These equations, in parallel with the governing equations above, provide the fluid mechanics software with sufficient information to calculate an accurate flow field.

According to Scott-Pomerantz (2004) the first $k - \varepsilon$ model was by developed by Harlow and Nakayama in 1968 at the Los Alamos Science Laboratory. These equations describe the dynamic nature of turbulent flow, which led to them inheriting the functional description of ‘transport equations’. These equations are shown below.

$$k_t = \alpha \left(\frac{k^2}{\varepsilon} k_x \right)_x - \varepsilon \quad (2.15)$$

$$\varepsilon_t = \beta \left(\frac{k^2}{\varepsilon} \varepsilon_x \right)_x - \gamma \frac{\varepsilon^2}{k} \quad (2.16)$$

where

$k_t =$ Turbulent Kinetic Energy

$\varepsilon_t =$ Turbulent Dissipation Rate

$\alpha =$ Positive Constant

$\beta =$ Positive Constant

$\gamma =$ Positive Constant

According to Savli (2012) turbulent kinetic energy describes the energy contribution that turbulent eddies within a mean flow have to the overall kinetic energy of that flow. The mean kinetic energy of a flow can be calculated by taking the kinetic energy of the flow using the mean flow speed in the following equation.

$$MKE = \frac{1}{2} m (\bar{u}^2 + \bar{v}^2 + \bar{w}^2) \quad (2.17)$$

where $MKE =$ mean kinetic energy

Turbulent kinetic energy expands on this mean energy by taking the root mean square (RMS) of velocity fluctuations within the flow field. This value encompasses all the normal stresses contained within the flow and is described by the equation below.

$$TKE = \frac{1}{2}m(\overline{u'^2} + \overline{v'^2} + \overline{w'^2}) \quad (2.18)$$

where $TKE = \text{turbulent kinetic energy}$

This allows for the calculation of the turbulent intensity contained within a flow. The second equation for turbulent dissipation rate mathematically describes the natural law that turbulent eddies will decrease in intensity and energy as time passes.

As the turbulent kinetic energy contained within a flow is subject to change, the main focus of computational fluid mechanics is on the turbulent kinetic energy budget. This budget describes the rate of change of the turbulent kinetic energy over time.

2.3.1.1 The Standard $k - \varepsilon$ Model

(Launder et al. 1972) recognised this when they derived the true numerical transport equations for computational analysis of turbulent flows. These equations have become the basis of modern day two-equation turbulence modelling due to their economical delivery of accurate results when applied correctly. According to the ANSYS Help file, the mathematical derivation of the following equations assumes that the analysed flow is fully turbulent and that the molecular viscosity is negligible. As such, all $k - \varepsilon$ models are only valid for turbulent flows. The equations that describe the standard form are shown below.

$$\frac{\delta}{\delta t}(\rho k) + \frac{\delta}{\delta x_i}(\rho k u_i) = \frac{\delta}{\delta x_j} \left[\left(\mu + \frac{\mu_t}{\sigma_k} \right) \frac{\delta k}{\delta x_j} \right] + G_k + G_b - \rho \varepsilon - Y_M + S_k \quad (2.19)$$

$$\frac{\delta}{\delta t}(\rho \varepsilon) + \frac{\delta}{\delta x_i}(\rho \varepsilon u_i) = \frac{\delta}{\delta x_j} \left[\left(\mu + \frac{\mu_t}{\sigma_\varepsilon} \right) \frac{\delta \varepsilon}{\delta x_j} \right] + C_{1\varepsilon} \frac{\varepsilon}{k} (G_k + C_{3\varepsilon} G_b) - C_{2\varepsilon} \rho \frac{\varepsilon^2}{k} + S_\varepsilon \quad (2.20)$$

where

$$G_k = \text{TKE from mean velocity gradients}$$

$$G_b = \text{TKE from buoyancy}$$

$$Y_M = \text{dissipation due to compressibility}$$

$$C_{n\varepsilon} = \text{constant}$$

$$S_n = \text{User Defined Source Term}$$

$$\sigma_k = \text{Prandtl Number (Turbulent Kinetic Energy)}$$

$$\sigma_\varepsilon = \text{Prandtl Number (Turbulent Dissipation)}$$

For the analysis of subsonic flow, the compressibility term can be ignored as the fluid used within this analysis is incompressible under the scenario conditions. These equations are used by the software in order to calculate the turbulent viscosity of the fluid body. The equation for this calculation is as follows.

$$\mu_t = \rho C_\mu \frac{k^2}{\varepsilon} \quad (2.21)$$

where

$$\mu_t = \text{Turbulent Viscosity}$$

$$C_\mu = \text{Constant}$$

(Damjanovic et al. 2010) used this standard form of the $k - \varepsilon$ model with the following default values in their 2D analysis of airflow about a conceptual vehicle.

$$C_{1\varepsilon} = 1.44$$

$$C_{2\varepsilon} = 1.92$$

$$C_\mu = 0.09$$

$$\sigma_k = 1.00$$

$$\sigma_\varepsilon = 1.30$$

This allowed the group to model the effects of turbulence to a sufficient degree of accuracy without exploring the effects of changing the model to a more suitable, near wall specific model. However, if this group had researched further, they would have been able to recognise that this standard $k - \varepsilon$ model was specific to high Reynolds number flow. As their flow was at relatively low speeds in the subsonic range, a more specific model would have increased the accuracy of the results.

2.3.1.2 The Renormalisation Group $k - \varepsilon$ Model

Since their inception in 1972, the $k - \varepsilon$ have been modified into a number of different forms that optimise the numerical equations for uses in specific applications. One of the newer $k - \varepsilon$ models is called the renormalisation group model which was formulated in Yakhut and Orzsag (1986). This model improves on the low Reynolds number computation of the standard $k - \varepsilon$ model. It introduces a new term into both of the base transport equations in order to allow the software to more accurately model rapidly strained flow. These types of flows include turbulent swirls and vortices that often occur in the near wall region when geometries change rapidly. Provided that the near wall treatment values are set up correctly, this solution is significantly more adept at modelling near wall flow. Interestingly, the change in Reynolds number focus only reduced the C_μ to 0.0845, still close to the standard.

(Roumeas, Gillieron & Kourta 2008) utilized this enhanced accuracy in their three dimensional reconstruction of a previously 2D flow analysis. Their investigation was based about the effect that an applied suction has on the flow separation over the rear of a Renault hatchback. As their analysis was specifically focussed on the near wall effects of separation vortices on the drag produced behind the car, this model was the ideal choice.

Their results showed that by controlling the suction effect over the rear window of a hatchback, the pressure drop at the rear of the car could be reduced and pushed further behind the rear of the vehicle. This reduced the drag forces on the whole car by approximately 17%. They were able to present their results with confidence, knowing that their treatment of the low Reynolds number flow was suitably defined.

2.3.1.3 The Realizable $k - \varepsilon$ Model

The last commonly applied $k - \varepsilon$ model is called the realizable model. This model improves on the previous two equations by allowing the C_μ term to be varied based upon the properties of the fluid within the turbulent boundary layer development. This turbulent boundary layer is where the velocity gradient of the flow develops the most rapidly. As such, accurate modelling of the fluid properties in this region is vital to the accuracy of the solution.

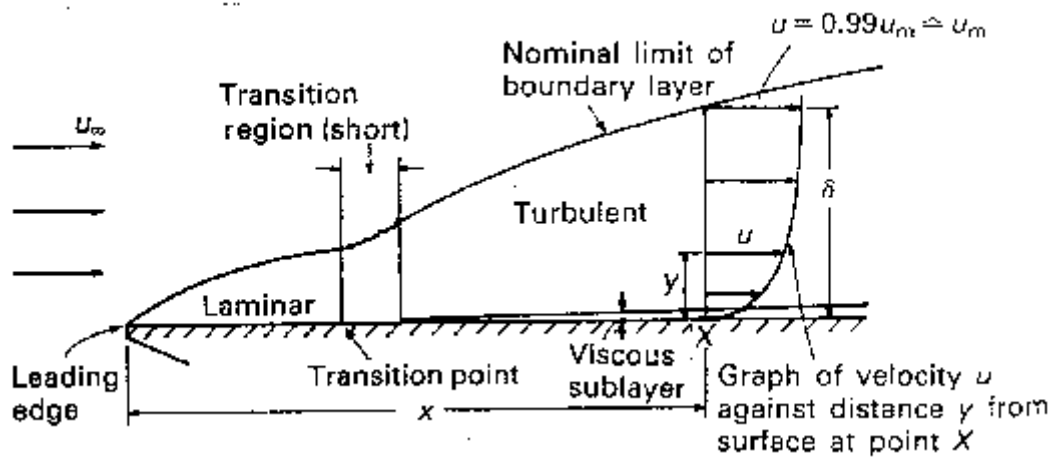


Figure 2.11 – Boundary Layer Development on a Flat Plate

The realizable model sets the C_μ term to approximately 0.09 within a logarithmic development layer of the fluid boundary layer, in keeping with values of the first two models discussed. However, when flow is deemed to be flowing with a strong homogenous shear the value for C_μ can drop as low as 0.05, far below that of the previous models.

The realizable model gains its name from (Shih et al. 1995) because it has added mathematical features that ensure the physics of the flow conform to the theory of turbulent flows in regards to Reynolds stresses. Shih also modified the turbulent dissipation transport model away from the approximate value used to the first to models. Shih's realizable model uses a mathematically exact formula instead, which was derived from an existing vorticity fluctuation formula. For this reason, the realizable model is considered mathematically advanced. According to the ANSYS

Help file, one of the only negative aspects of the realizable transport model is its inability to accurately model multiple reference frames due to the changes to the transport equations.

(Mafi 2007) shows how adept the realisable $k - \varepsilon$ model is at simulating low Reynolds number turbulent flow in his investigation into turbulence reduction at the rear of a Formula 1 vehicle. Mafi uses a very fine mesh within a 2D domain in order to determine the negative lift performance of a rear wing that diverts a significant portion of the airstream upwards when deployed at large angles. After the general case is solved he again uses the realizable model, this time in 3D form, to analyse the vortices present in the upward flow.

2.3.2 The $k - \omega$ Turbulence Model

The other form of two equation fluid modelling within ANSYS is called the $k - \omega$ turbulence model. This model still uses an equation for the turbulent kinetic energy within the flow, but it replaces the turbulent diffusivity equation with a term called the specific dissipation rate. Its base equations are shown below.

$$\frac{\delta}{\delta t}(\rho k) + \frac{\delta}{\delta x_i}(\rho k u_i) = \frac{\delta}{\delta x_j} \left[\Gamma_k \frac{\delta k}{\delta x_j} \right] + G_k - Y_M + S_k \quad (2.22)$$

$$\frac{\delta}{\delta t}(\rho \omega) + \frac{\delta}{\delta x_i}(\rho \omega u_i) = \frac{\delta}{\delta x_j} \left[\Gamma_\omega \frac{\delta \omega}{\delta x_j} \right] + G_\omega - Y_\omega + S_\omega \quad (2.23)$$

This model was specifically designed to model low Reynolds number, compressible flow. It has the ability to accurately model this type of flow within the turbulent shear layer of the near wall; however it can produce unreliable results when the values for k and ω lie outside this layer, in the free stream flow. As this is specifically created for compressible flow, it was determined that this model was not suitable within this analysis.

3 Methodology – 3D Modelling

This section of the document details steps taken in the modelling process, ranging from the wing geometry to the mesh and surface modelling of the vehicle body.

3.1 Preliminary Work

Before any work could begin on setting up the problem, the parameters required in order to construct, model and evaluate the analysis needed to be discovered and compiled. This section acts as a reference guide for all the following steps.

Table 3.1 – JZA80 Toyota Supra Specifications

Toyota Supra Specifications	
Length	4514 mm
Width	1810 mm
Height	1245 mm*
Track (front/rear)	1520 mm / 1525 mm
Wheelbase	2550 mm
Ground Clearance	100 mm*
Mass	1550 kg (53%F/47%R)
Drag Co-efficient	0.33 (with wing)
Top Speed	250 km/h (restricted)
* Modified height in compliance with minimum legal Ground Clearance	

Table 3.2 – TRD 3000GT Wing Dimensions

TRD 3000GT Wing Dimensions	
Width	1080 mm
Chord Length	230 mm

The leading edge at the centre of the wing is 20 mm closer to the rear of the vehicle and raised 10 mm above the corresponding point on each side.

3.2 Developing the Wing Geometry

The process of developing a computer based model of the TRD 3000GT wing began with the dismantling and measurement of an existing carbon fibre wing blade. Using some thin cardboard sheet, scissors and a thin tipped permanent marker, the upper and lower contours were traced. This was achieved by requesting that a partner align the cardboard sheet perpendicular to each contour at the centreline of the wing. The thin tipped marker was then guided across the wing surface, tracing the contour onto the cardboard sheet. The sheet was then removed and scissors were used to cut along the traced line. This process was repeated several times, bringing the shape of the remaining card closer to the actual wing shape each time.

Once the upper and lower contours had been successfully reproduced, they were both fixed in place over a sheet of A4 paper. This allowed both contours to be traced onto a single sheet. The resulting sketch was then scanned to JPEG format, resulting in the image shown below.

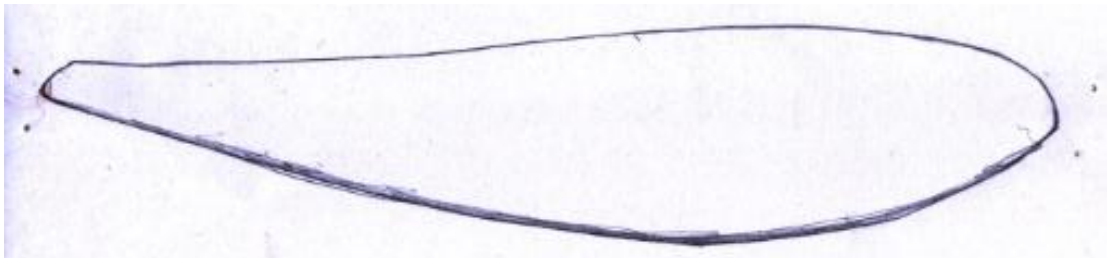


Figure 3.1 – The Sketched Wing Profile

This image could then be imported into AutoCAD 2012 as a raster image reference. After this, the closed loop spline curved tool was used in order to draft over the sketched lines. The resulting curve was then measured electronically to ensure that its scale and overall dimensions accurately reflected the true dimensions of the existing wing.

The AutoCAD sketch satisfied the dimensional checks and was then imported into SolidWorks to act as the basis for the 3D model. Further measurement of the wing showed that the overall length was 1080mm from face to face, with these faces

parallel to the centreline. The cross section differed minimally across the span of the aerofoil and as a result it was concluded that a constant cross section model was suitable. The leading edge at the centreline of the wing was 20mm closer to the rear of the vehicle and raised 10mm above the corresponding point on each face.

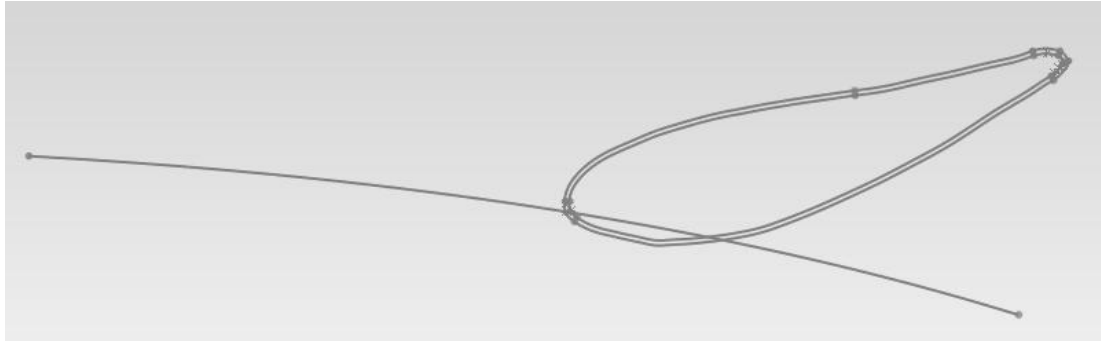


Figure 3.2 – The SolidWorks Sketches

From this data, another spline curve was drawn in SolidWorks that represented the location of the leading edge at all distances across the span of the wing. This curve intersected the leading edge of the imported aerofoil profile, allowing a spline extrusion of that profile across the span. A further addition to the extrusion process was the second, smaller aerofoil profile that was created using an offset distance of 2mm.

Once these profile sketches were finalised, both were extruded along the guide curve in order to form a 2mm thick solid body, where the larger profile was the outer shell and the smaller profile described the inner. The 2mm thickness was selected from Vernier calliper measurements of the carbon fibre weave of the existing wing. The end faces of the extrusion were then trimmed back to square as per the existing wing, with 2mm thick end caps added to form the final product, shown below.

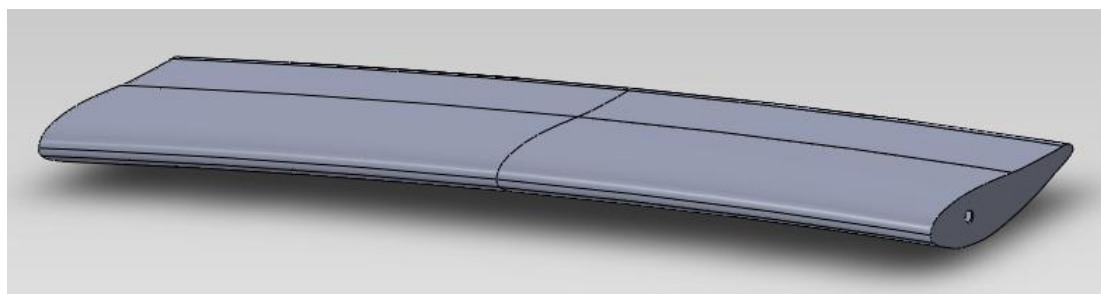


Figure 3.3 – The Final Wing Model

3.3 Developing the Vehicle Geometry

The vehicle geometry is considerably more complex than the wing and it was clear that a comprehensive tutorial or dimensional guide would be needed in order to prepare an accurate model. However, a lengthy search of solid modelling tutorial sites proved fruitless. As such, it was decided that pre-existing scale models could be used in place of creating a new file. A suitably well-constructed model was obtained free of charge from a computer model sharing site. This model had been constructed in Autodesk's computer modelling package, "3DS Max".

This program allows software companies to create 3D graphic animation models for video games and cartoon films. Unlike engineering based modelling suites, this application focusses more on the graphic appeal than rigid relationships between neighbouring features. This allows the user to freely use push and pull functions to quickly construct complex shapes from base objects.



Figure 3.4 – The Initial JZA80 Supra Model

Despite this relative lack of accuracy when compared to equivalent engineering programs, the overall dimensions of the vehicle, shown above, were in exact proportion to the actual vehicle. A trial version of the 3DS Max program was downloaded and the model was stripped of all non-essential features in order to decrease the size of the file and minimise the processing power required to manipulate the shell. These features included the interior, wheels, brakes, standard rear wing, antenna, door handles, windscreen wipers etc.

The next step in the process was to save the cleaned up geometry as a file type that could be supported by SolidWorks 2012, as the native 3ds format was not. The first and most ideal file type was the Alias Wavefront format, OBJ. This format was deemed ideal as it significantly decreases the number of elements in the file, while also ensuring that the mesh remains symmetrical about the centreline of the vehicle. This axis of symmetry would enable the sectioning the fluid dynamics model about the centreline in order to only model flow over half the vehicle, greatly decreasing the processing time for each solution.

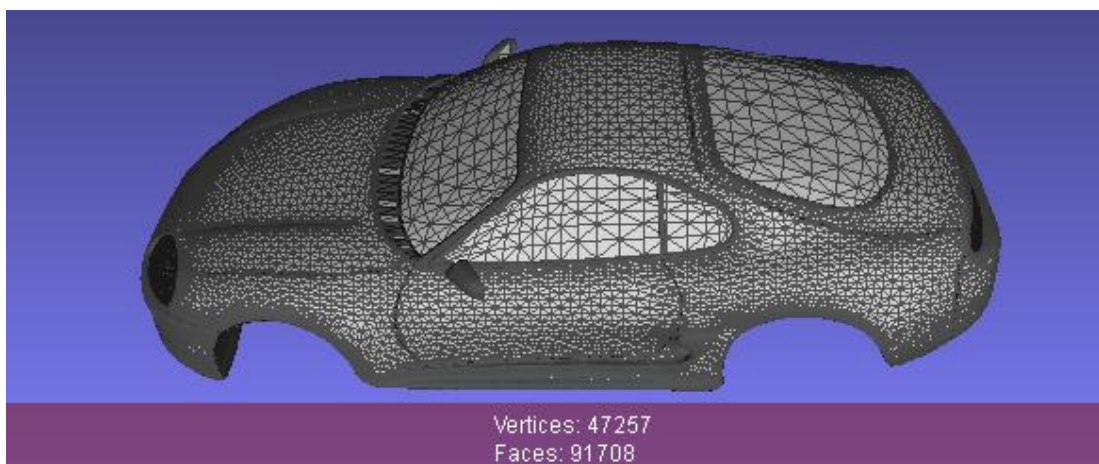


Figure 3.5 – The Alias Wavefront OBJ Format

Unfortunately, the information required to recreate a mesh model of such a complex sheet resulted in these ideally rectangular faces becoming sectioned across the diagonal, forming double the ideal number of faces. This led to an increase of file size from 5.5 MB to 6.4 MB, a substantial increase in an already large file. The file size was also well beyond the limit of the free OBJ import add-on for SolidWorks 2012, indicating that a different approach had to be taken.

Upon viewing several SolidWorks webinars, it was found that many other users have experienced similar issues with the conversion of complex geometries. The recommendation from the presenter was to move on to using the Standard Tessellation Language (STL) file format. This format is most commonly used in the stereo-lithography field of rapid prototyping and is a widely supported 3D file format in both the engineering and graphic design software suites.

The base file from figure 3.5 was once again exported from 3DS Max, this time into the STL format. This reduced the file size from 5.5 MB to 4.1 MB whilst also reducing the number of faces required to describe the geometry from the original 91708 faces to 84245 faces.

The subsequent attempt to import this STL export into SolidWorks 2012 failed, due to the inbuilt 20,000 facet limit of the software. As a result, an intermediary meshing program called MeshLab was downloaded in order to allow for the mathematical manipulation of the mesh.

The first action, upon opening the STL file in MeshLab, was to unify any duplicated vertices automatically. This process allowed for the deletion of any construction lines that were used in the modelling process that were no longer the largest element along their length. The next action was to repeat the unification of close vertices, this time within a tolerance of 1% of the element length. This accounted for coincident lines on neighbouring features to become knitted together to form a single continuous feature. For example, the left hand edge of the bonnet that runs, for the most part, directly next to the upper edge of the left hand guard, would be removed and its nodes would be integrated along the line of the guard.

Once the majority of the body had been combined into a single continuous meshed surface, the 'Close Holes' function was used to create surfaces in sections of the shell that are holes in real life. These holes include the gaps in the front bumper bar that allow air to flow through to the wheel arches and engine bay etc. While these gaps exist in reality, as mentioned before, the fluid dynamic software is only capable of modelling flow over sealed bodies.

Now that the shell has been combined into an acceptable final form, the mesh needed to be manipulated to allow a significant decrease in the number of elements without becoming detrimental to the useability of the output mesh. All of the tools in the Filters > Remeshing, Simplification and Reconstruction menu were used in succession in order to separate the filters that worked successfully from those that crashed the program or significantly deformed the mesh.

From this experimentation, it was found that the most suitable tool for use in this application was the ‘Quadratic Edge Collapse Decimation’ filter that allowed for the mesh to be reduced as close as possible to a definable number of faces, whilst preserving the mesh boundary and topology. Given that this mesh was to be used as a flow model, this filter was a perfect choice. Figure 3.6 shows the method used to define the target faces and weighting assigned to boundary preservation.

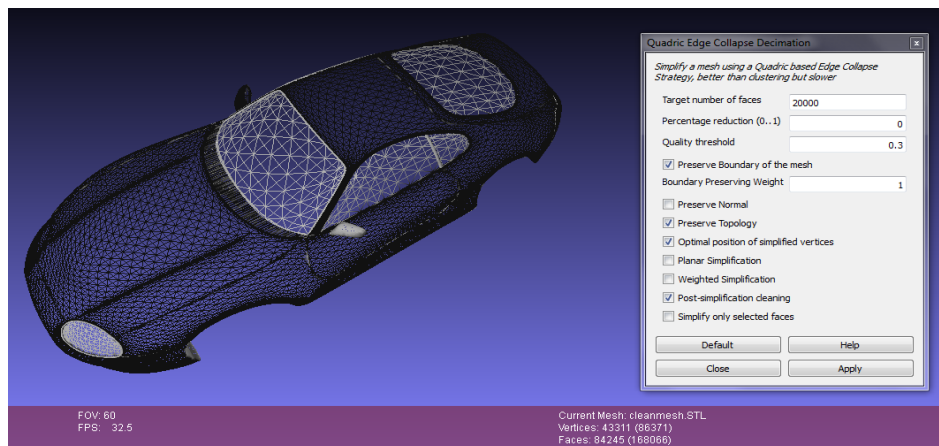


Figure 3.6 – Quadratic Edge Collapse Decimation

This filter was used a number of times in order to toggle between selecting the entire mesh, or simply sections at a time. Major gains were experienced when selecting planar faces, such as the floor of the vehicle or the interior of the wheel arches. These sections could be collapsed into a small number of large planar faces without causing detriment to curves. Several meshes were created below the 20,000 face limit in order to determine a suitable file size that combined accurate geometry with minimal elements. Figure 3.7 below shows the result of reducing the mesh to just under 20,000 faces within MeshLab.

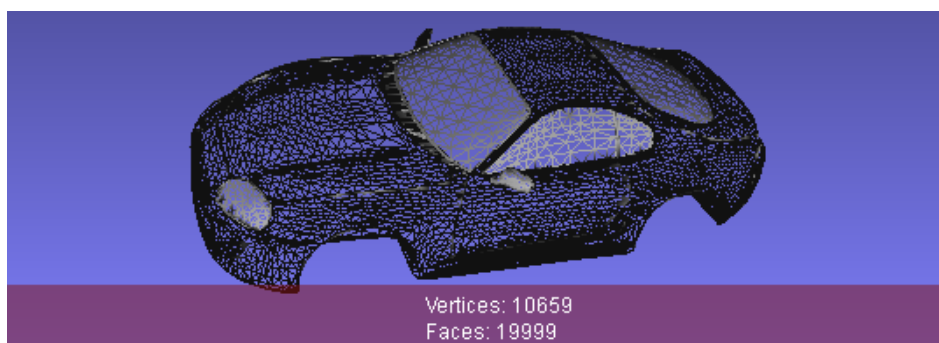


Figure 3.7 – 19,999 Face Mesh in MeshLab

It is clear through comparison between Figure 3.6 and Figure 3.7 that the structure of the mesh is significantly decreased through the action of making it compatible with SolidWorks 2012. This became more apparent when the 20,000 face mesh was saved as an STL file and imported into SolidWorks. The action of opening the file in SolidWorks using its inbuilt import manager and error healing tool took approximately 6 hours, providing the faulty edges were healed separately before attempting to heal faulty faces.

The resulting import, shown below, could be saved as a SolidWorks part file, consisting of a combination of surface and solid model features. The blue lines littered throughout the image indicate faulty geometry that couldn't be healed automatically in the import process.

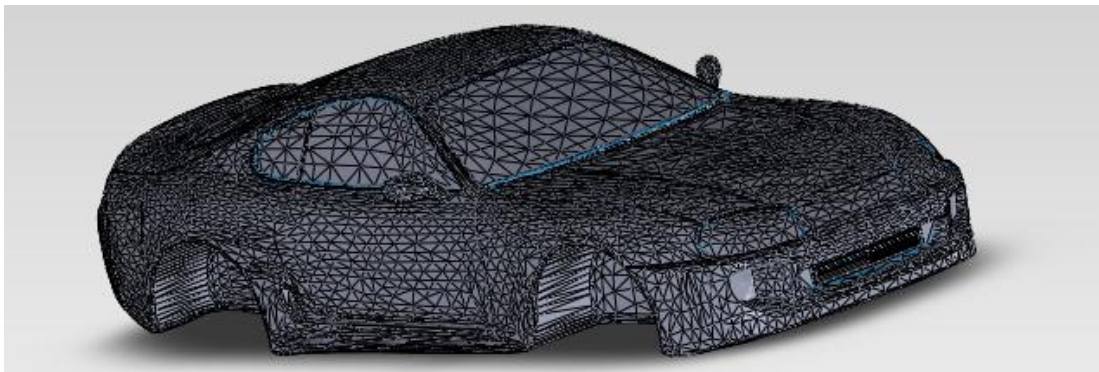


Figure 3.8 – 19,999 Face Part in SolidWorks

The manual healing process for the faulty geometry errors was lengthy, but successful for the most part. Faces with at least one faulty edge were deleted and replaced with new planar faces. These faces were then knitted into the mesh using the merge tool. However, the size of the file grew significantly with each feature addition, resulting in a 10.3 MB file at halfway through the healing process.

As a result of this rapidly growing complication, a new direction was pursued. Another Autodesk program called 'Rhinoceros' was downloaded, along with the newly released version of an add-on called 'T-Splines. This add-on had been specifically created in order to aid professionals in the rapid prototyping field by allowing the conversion between the polygonal STL files and the NURBS based engineering programs.

It allows the operator to import an STL file into rhinoceros and simply select faces that they wish to convert from a mesh of nodes into a singular curved surface. The ‘Convert to T-Spline’ feature interprets the mesh data, seen above in Figure 3.6, as a point cloud of nodes connected by curved elements, rather than the linear elements that were created within the SolidWorks import in Figure 3.8. The result of importing the Figure 3.6 mesh file into Rhinoceros is shown below.

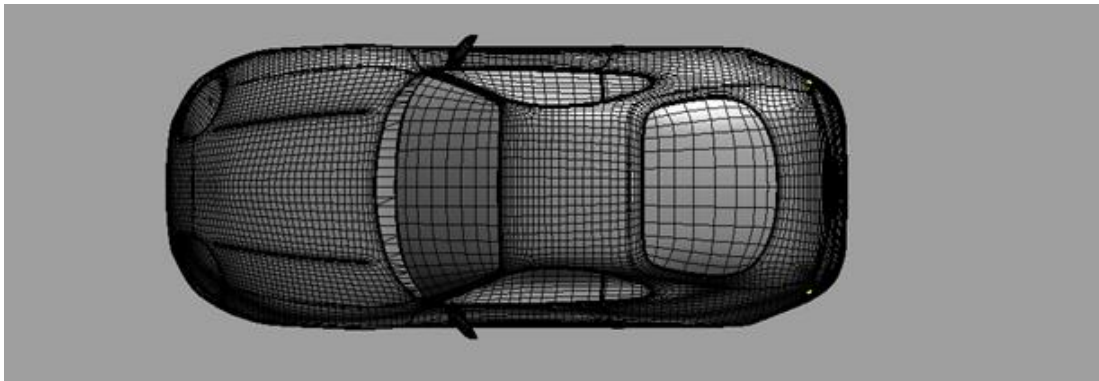


Figure 3.9 – The Rhinoceros T-Splines Model

The OBJ mesh style is more distinguishable in Rhinoceros than it was in MeshLab, with a clear network of predominantly quadrangle faces. Despite the appearance of being curved, these faces are still planar and will remain so until the T-Spline software can be applied to the geometry. The act of using the base OBJ mesh that came with the download means that the model is composed of several independent meshes that needed to be selected independently and converted to a T-Spline surface.

An example of the T-Spline effect is shown below. This is the smooth toggle function that converts the linear node connections to curved connection based on the location of the surrounding nodes.

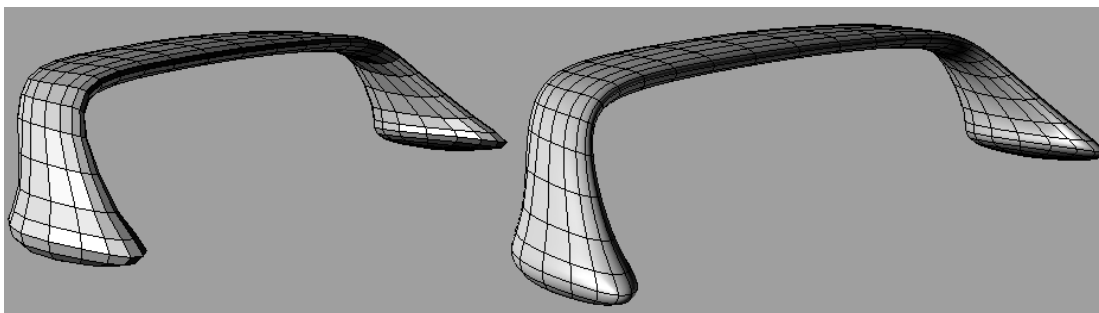


Figure 3.10 – The T-Splines Function

The smooth toggle function worked for several minor meshes within the base model including the standard wing, wheels, bonnet and windows. However the rear section of the car failed to be converted in this manner due to an issue called ‘Non-manifold geometry’. This is when there are three or more faces that connect run coincident along a single element. The T-Splines function cannot determine which of the faces is faulty and bypass that in the curve fitting process. A visual example of non-manifold geometry is shown below. The yellow highlighted elements in the left hand image detail the problematic geometry in the model.

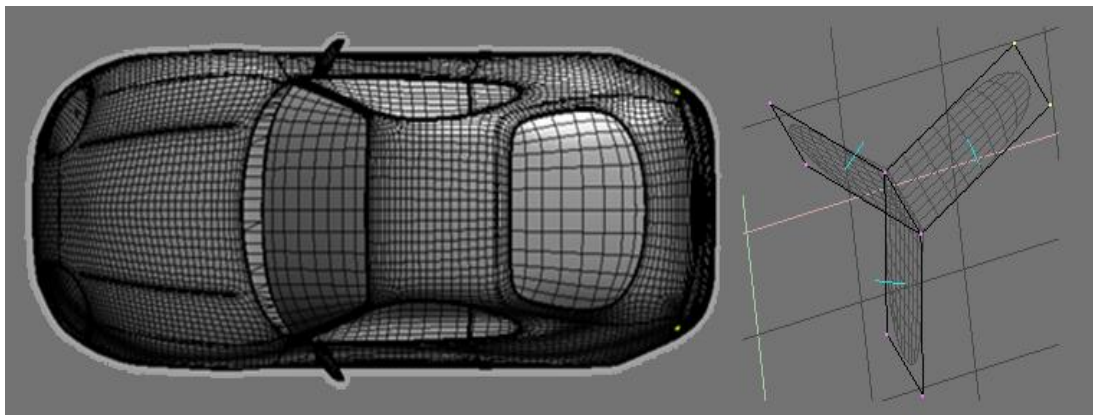


Figure 3.11 – Non-Manifold Edges

Both MeshLab and Rhinoceros have functions with the ability to heal non-manifold edges; however the act of running each case created more non-manifold sections in the process of healing the initial fault. Even after help was sought from other users of T-Splines, through the applications online forums, this problem was still present. The most common comment was that the mesh shown above was too complex to the program to heal without major, time-consuming reconstruction.

This led to the decision to abandon the 3DS model completely in favour of a newly released NURBS based surface model, available for purchase on the CAD sharing site ‘TurboSquid.com’. This model had been created ‘Rhinoceros’ and was significantly more detailed than the original model shown in Figure 3.4. Despite the added detail, the base mesh was less complex than the 3DS model and required significantly less elements to detail the shape of essential features.

The new model was provided in both IGES and 3dm formats, where IGES is a universal NURBS format for conversion between software packages and 3dm format is the primary modelling format used in Rhinoceros. This new file is shown below in Figure 3.12.

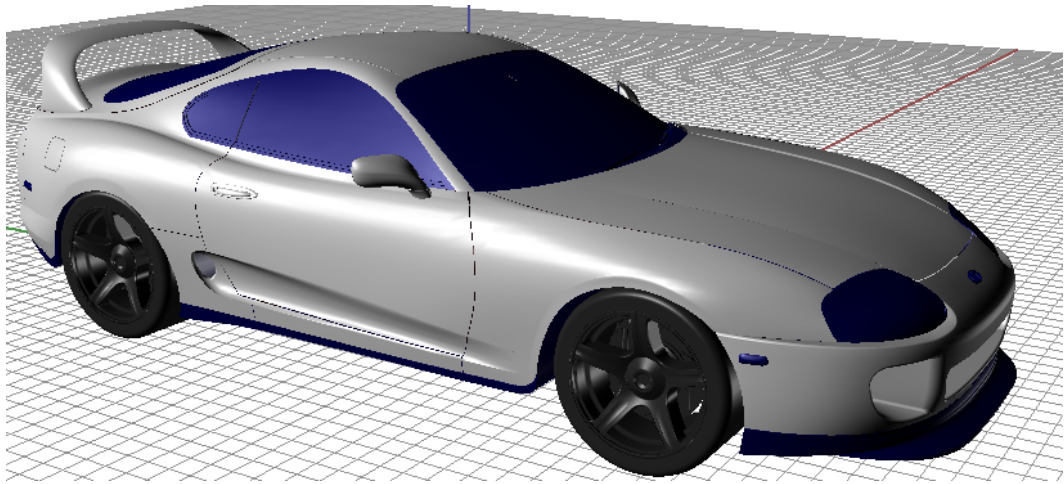


Figure 3.12 – The Rhinoceros ‘NURBS’ Model

The file was originally opened in Rhinoceros using the 3dm format model in order to allow for the deletion of unnecessary elements. It was clear that this model was immensely superior to the initial 3ds model, as each body element had been modelled separately and assembled accurately to form the final model.

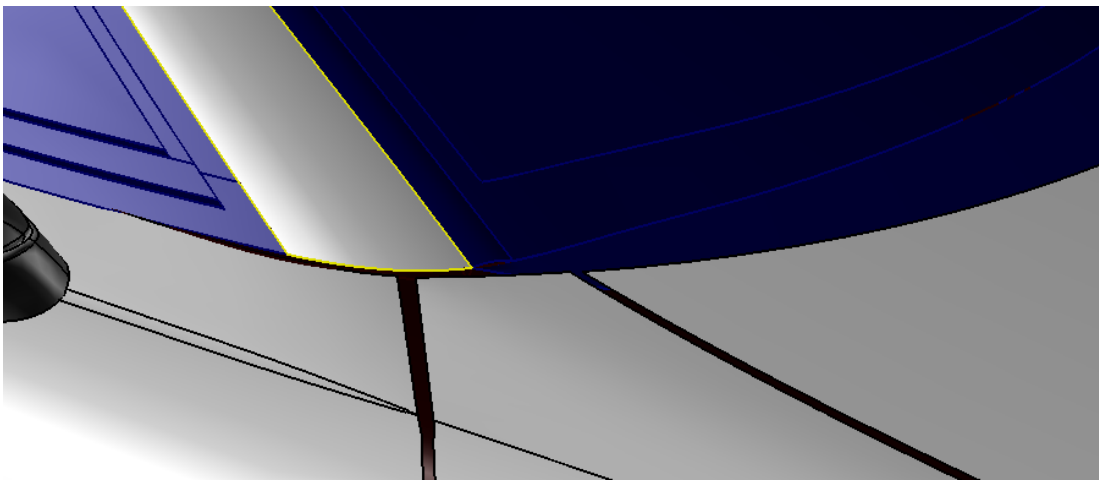


Figure 3.13 – Gaps Between Faces

As with the 3ds model, features such as the interior, wheels, exhaust, wing and door handles could be removed to further reduce the overall size of the file and hence the number of mesh elements required to define the geometry. Once satisfied that the geometry was sufficiently clean, the gap closing process could begin.

This model was assembled from independently created features, the inbuilt 'Heal Gaps' function could not be used, as Rhinoceros could have no way of correctly deciding which features should be joined. As an alternative, lines were inserted between corner nodes of adjacent features to define the edges that needed to be joined together. For example, the top right corner of the door feature in Figure 3.13 was connected with a simple line to the top left corner of the front guard feature. From here, a two line sweep could be inserted from the surface modelling menu. The sketched line defined the surface cross section and the adjacent feature edges acted at the sweep guide. This allowed a large number of faces to be joined, creating an essentially airtight geometry.

3.4 Prohibiting Factors

Unfortunately, this manual healing process was very slow and the modelling process had already exceeded all of its allocated project time. This realisation, compounded with the discovery of a Birmingham University paper, Chandra et al (2011), led to the abortion of the 3D flow modelling process.

Chandra et al (2011) describes the method a team of engineering students used to analyse the flow over a PACE Formula 1 vehicle. After using a similarly healed solid model with an equivalent number of polygonal faces, the group found that to solve 1000 iterations within their fluid dynamics software took approximately 22 hours. This figure was given for a regular dual core computer, identical to the laboratory computers available at the University of Southern Queensland.

As this project proposes to analyse flow over a large number of vehicle speeds and wing angles, the continuation of the model healing process was deemed to be in vain. With more than 180 simulations needed to comprehensively determine resultant forces, it was clear that a 3D solution required far more time than was available.

4 Methodology – 2D Fluid Dynamics Model

4.1 Developing the Model Geometry

The first step in the creation of the two dimensional model was to find a dimensionally accurate two dimensional image of the Toyota Supra. A search of the site 'CarBluePrints.info' resulted in the discovery of the following side view. This view is of a JZA80 Series 2 Toyota Supra and includes an accurate dynamic front spoiler, appended to a standard front bar. These features were desirable as this is the most aerodynamically advanced package available from the factory.

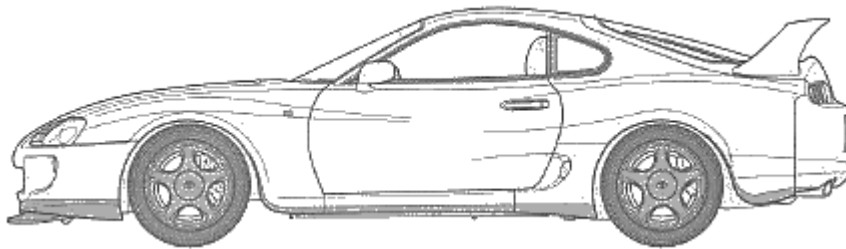


Figure 4.1 – Blueprints of the 1996-2002 Toyota Supra

This side view was then imported as a raster image reference into AutoCAD to allow for the sketching of the external contour. Damjanović (et al 2010) showed that for two dimensional flow modelling, the cross section at the centreline of the vehicle must be sketched in order to show the maximum cross section. Also, the wheels must be excluded from the modelling process in order to allow the flow modelling software to recognise that air can flow beneath the vehicle. If the wheels were included, the software would assume that the front wheels were that same width as the vehicle, preventing air that flows underneath the front bumper from continuing past the contact patch of the front tyre and the road.

Once the external contour of the vehicle was sketched using a mixture of spline curves and linear elements, the drawing was saved and imported into SolidWorks as a drawing. Within SolidWorks, the drawing was then saved as a SolidWorks part, allowing for the use of the 'Filled Surface' tool. This patched the boundary defined by the centreline contour with a surface body. This was also used on the base

sketches for the TRD wing, shown in Figure 3.2, in order to create a 2D surface body that represented the cross section of the wing.

Both of these newly created surface bodies were then imported into a SolidWorks assembly file, as shown below. A real Supra with the same TRD 3000GT wing was used in order to determine the location of the wing with respect to the body. It was found that the leading edge of the wing was located 200mm vertically above the surface of the rear hatch and 300mm in front of the rearmost portion of the rear bumper.

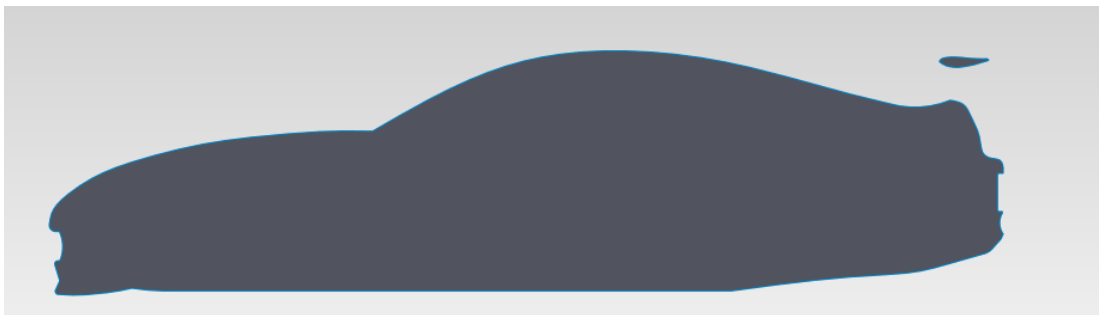


Figure 4.2 – The 2D SolidWorks Assembly Model

Once the wing was moved to this location, it was rotated anticlockwise about the leading edge so that the aerofoils angle of attack was -3° , as per the standard setting. From here, a point needed to be selected that would represent the active aerofoils axis of rotation.

The first option considered was to rotate the wing about the aerofoils theoretical centre of pressure. However, as the aerofoil used is a cambered non-symmetrical example, the centre of pressure moves along the chord length according to the angle of attack. At steep angles of attack, the aerodynamics centre lies at slightly greater than $\frac{1}{4}$ the total chord length and this point will move toward the trailing edge as the angle of attack is decreased and the lift co-efficient increases.

The quarter chord length value was calculated to be at 57.5mm along the 230mm chord length of the TRD 3000GT aerofoil. This value was then rounded to 60mm in order to account for the dynamic nature of the centre of pressure. Using SolidWorks, this point on the chord line was sketched into place. The point was then moved vertically downward onto the camber line in order to have the rotation point spaced

equidistant from both the upper and lower surface of the aerofoil. This was done to allow the aerofoil material to disperse the stress concentrations evenly and efficiently about the rotation point.

The aerofoil part of the assembly model, shown in Figure 4.2, was then rotated clockwise 3° about the newly defined rotation point in order to show the location of the wing at 0° angle of attack. This assembly file was then exported from SolidWorks as a STEP file so that it may be imported into ANSYS as a geometry file. Several similar files were created after this, with angles of attack decreasing in 5° increments from 0° to -50° , then in 10° increments from -50° to -90° . Another two STEP files were created for positive angles of attack at 5° and 10° in order to evaluate the performance of the aerofoil at all probable attack angles.

The first of these STEP files was then imported into a standalone geometry section in ANSYS Workbench. The geometry properties were set to 2D in Workbench to indicate that only the x and y planes could have model features. Each of the STEP files was then encased in a 2D enclosure according to specifications shown in Damjanović (et al 2010). These specifications are shown below.

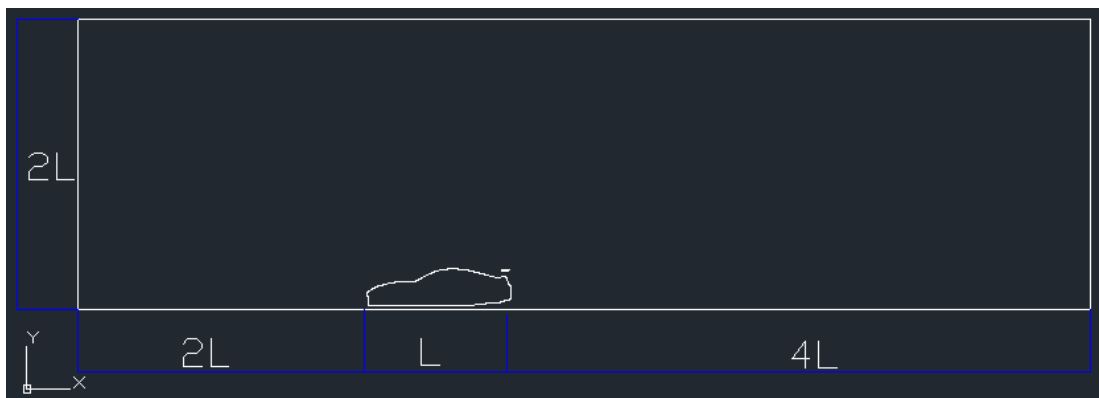


Figure 4.3 – The 2D Flow Model Domain ($L = 4514\text{mm}$)

Once the domain had been sketched on the same plane as the 2D Supra model, an attempt was made to use the “Surface from Sketches” tool to create a surface between the external contour of the vehicle and the domain walls. For a currently unknown reason, ANSYS would recognise the lines used to create the vehicle contour but would not allow them to be selected for further modelling purposes. This

ultimately led to the re-tracing of the vehicle contour within ANSYS' geometry section in order to allow a surface to be created.

Once traced, the imported STEP file could be suppressed leaving the sketch of the domain and the sketch of the vehicle contour free to interact with each other without error. Before a surface could be inserted between the sketches, the wing needed to be traced in the same manner. It was clear that from this point on, the only geometry change within the model was the angle of the wing. As such, the geometry file was duplicated a number of times within ANSYS workbench to create geometry sections for each wing angle.

Each geometry section was named according to the proposed angle of attack that it would model. The corresponding STEP file for that angle was then imported into each separate model, overlapping the suppressed import that was used to trace the vehicle contour. Both imports were then unsuppressed to ensure that the ANSYS import manager had used the correct global co-ordinates. This is shown below.

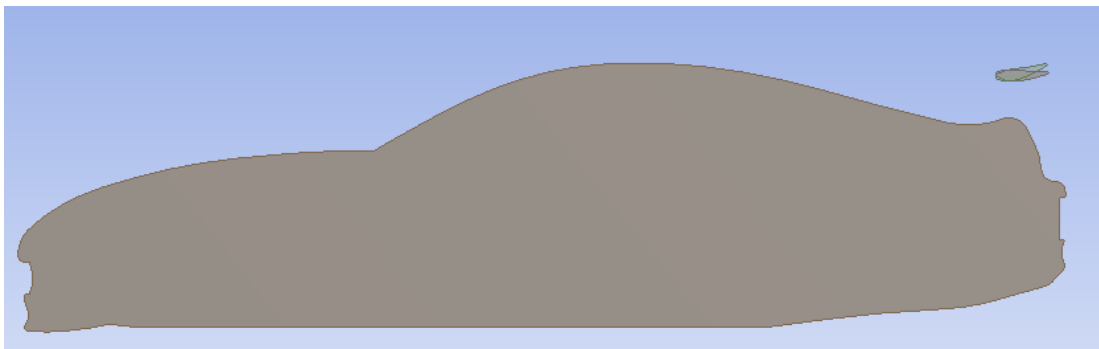


Figure 4.4 – The Overlapping STEP Imports

This shows that the second import (green) has identically defined vehicle co-ordinates, with the only differentiation between it and the initial import (grey) being the different wing angle of attack. For each model, this green element was traced within the same sketch as the original vehicle contour sketch. This allowed the surface from sketches tool to correctly fill the void between the domain walls, the vehicle contour and the wing contour.

The resulting surface body was a 2D representation of the fluid domain. As such, the properties of the solid were changed from solid to fluid in the 'Details of Surface

Body' tab. This ensured that all further steps in the analysis process recognised that the body in question had the physical properties of air.

4.2 Meshing the Domain

At the end of the geometry creation process, a surface model of the 2D fluid body was created, each of which appeared similar to the domain shown below.

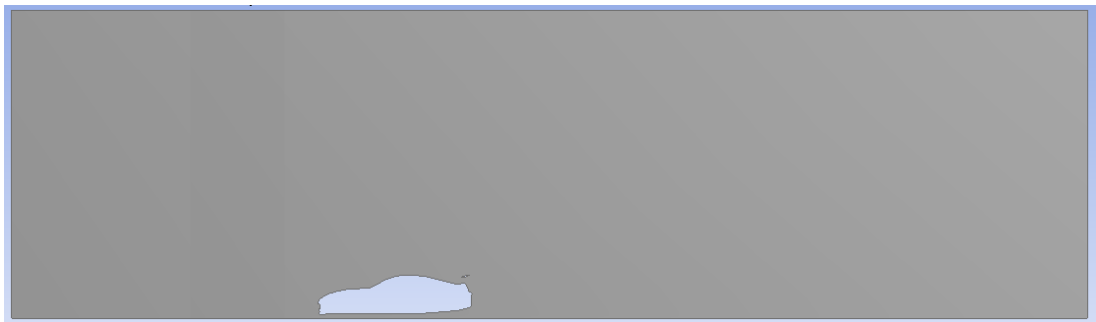


Figure 4.5 – The Final Domain

Mesh component systems were then added to the ANSYS Workbench model for each of the geometry components. The first act involved in setting up the mesh model was to set the mesh style to Computational Fluid Dynamics in the 'Physics Preference' section of the defaults tab. This tells the mesh generation software that the interaction between nodes will be based on a fluid body in motion, rather than a solid body mesh used for structural analysis.

The second action in the application defaults for the mesh was to indicate that the FLUENT would be used. This was done by setting the 'Solver Preference' to FLUENT, with an unchecked relevance setting of 0. This relevance setting can be used to describe whether the mesh should be optimised for solver speed or accuracy and spans between -100 and +100. This setting was not used, as the next steps in the setting up of the mesh allow more specific settings to be defined.

The next, most vital step in the preparation of the mesh is to define the sizing of the mesh. This was done in the 'Sizing' tab of the 'Details of Mesh' menu. The mesh sizing described the size, number and location of the elements used to create the mesh. In general, more elements equates to more accurate results, at the expense of increased processing time.

The first setting that required user input was the ‘Use Advanced Sizing’ drop down menu. This section allows the user to define which sections of the mesh are to be analysed in the most detail and therefore require the smallest element sizes.

It was clear from the review of automotive literature that the curves of the vehicle shell would play a significant role in the development of the flow. As such, the advanced sizing would be required to act on the vehicle curvature at a minimum. It was also known that sharp edges and rapid geometry changes play a significant role in the disruption of streamlines. The front and rear of the vehicle have several zones where gaps between geometric entities could play a significant role in the development of the turbulent flow. This led to the final selection of ‘On Proximity and Curvature’ in the advanced sizing tab.

Once the most important features within the mesh had been accounted for, the relevance centre needed to be defined for the mesh as a whole. This required user input as the relevance section of the default tab was not set earlier in the process. A fine mesh was initially considered, though the advanced sizing on proximity and curvature meant that the base element size could be reduced to a medium relevance centre without affecting the accuracy of the key zones. This would allow the solving time of the free stream flow to be reduced significantly as the free stream accounts for a very large zone within the domain.

The initial size seed was kept at the default value of ‘Active Assembly’ which allowed the STEP vehicle files that had been permanently suppressed in the geometry selection phase to be neglected in the meshing process. The other option of meshing the full assembly model would incorporate these suppressed parts in order to prevent the need for mesh regeneration if parts were unsuppressed.

The next value that required user input was the smoothing section that improves the element quality by performing smoothing iterations where node groups are relocated in bulk to allow for the smooth generation of a mesh. This smoothing value was set to its maximum value, ‘High’, in order to improve the quality of the curvature mesh.

After this, the span angle centre of the mesh needed to be described. According to the ‘ANSYS Help’ menu, this defines the goal angular range for mesh refinement about curvature. The ranges for each range are shown below. Due to the curved nature of the Supra body, the most obvious and desirable choice for this setting was ‘Fine’.

Table 4.1 – Span Angle Centre

Span Angle Centre	Angular Range
Coarse	91° - 60°
Medium	75° - 24°
Fine	36° - 12°

Once the meshing aids had been defined, parameters could be enforced within the mesh to describe the upper and low limits for element sizing. After significant experimentation it was found that the minimum allowable element size that did not significantly impact upon the performance of the FLUENT solver was 2mm.

The maximum allowable size between the nodes was most applicable to the free stream air; however the interaction between the free stream and the displaced air needed to be considered in some detail. As such, both the maximum allowable element size and the maximum face size were set to 85mm, allowing a medium mesh for the free stream that was not so coarse that it failed to detail the described interactions.

The last action used to define the mesh was to apply a fixed sizing parameter to the external contours of the wing and vehicle shell. This allowed the mesh to describe all of these surfaces with the same 2.5mm element size. This enhanced sizing allowed for the introduction of a significant number of nodes to the zones immediately next to the surfaces. These nodes are critical in the adequate modelling of the turbulent boundary layer as they allow the parabolic development of the velocity profile to be modelled correctly. The methods used in checking the adequacy of the nodes within the boundary layer will be described in greater detail within the modelling the flow section of this chapter.

A compilation of all the values changed in order to create a suitable CFD mesh is shown below in Table 3.4. These settings, in co-operation with the ‘Edge Sizing’ tool allow the program to generate the final mesh used for the flow analysis.

Table 4.2 – The Mesh Settings

Menu	Parameter	Setting
Defaults	Physics Preference	CFD
	Solver Preference	FLUENT
Sizing	Use Advanced Sizing	On : Proximity and Curvature
	Relevance Centre	Medium
	Initial Seed Size	Active Assembly
	Smoothing	High
	Span Angle Centre	Fine
	Min Size	0.002m
	Max Face Size	0.085m
	Max Size	0.085m

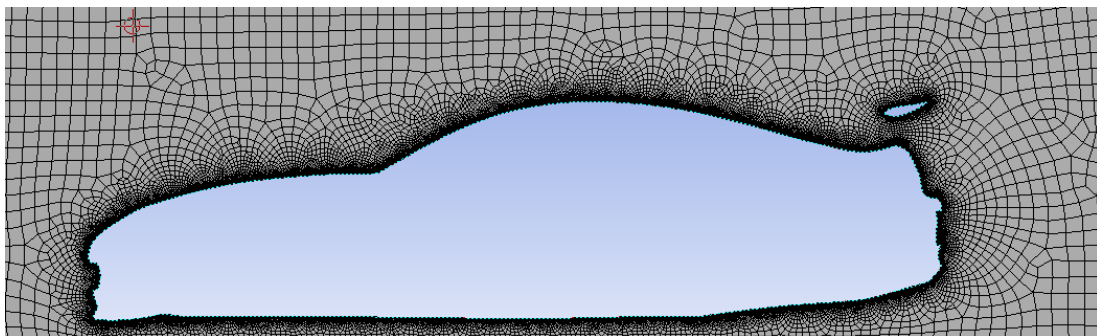


Figure 4.6 – The Vehicle Mesh

The final step in the Meshing process is to identify edges at which properties will need to be specified. These edges are then used to create ‘Named Selections’.

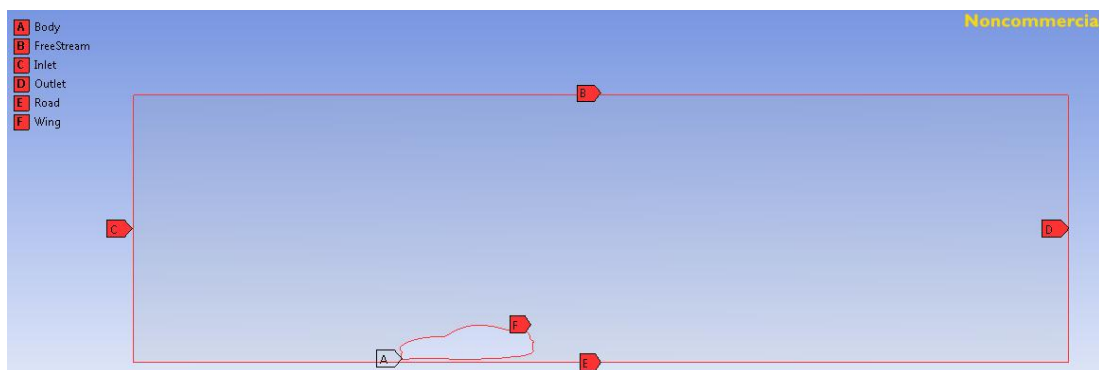


Figure 4.7 – The Named Selections

4.3 Modelling the Flow

The final step in ANSYS workbench is to create FLUENT component systems that reference geometry and mesh component pairs. This allows FLUENT to use the mesh files and named selections, indicated within these toolboxes, as base elements in the solving process. After this, the FLUENT was launched.

4.3.1 The FLUENT Launcher

The first step in modelling the flow is to alter the settings of the FLUENT launcher. The launcher had already determined that the flow was to be 2D, given that this was specified in the geometry toolbox. The next step was to identify the number of parallel processors that FLUENT has available in order to maximise the solving potential. Initial models were set up to take advantage of the dual processors available in the laboratory computers at USQ; however this led to memory issues for the models with high angles of attack. This fact, coupled with the fact that each processor required its own FLUENT license, meant that the solver was limited to using a single processor in serial mode.

4.3.2 Problem Setup - General

Once the FLUENT solver was opened, the model could be set up according to the findings of the literature review. The first tab in the 'Problem Setup' menu allowed for the selection of the general, solver specific, parameters.

The solver type was set to pressure-based as the fluid in question was a gas and the aerodynamic capabilities in question were direct effects of the change in gas pressure. Velocity formulation was left at its default setting of absolute. The time parameter was kept to steady, as the aim of the process was to get a steady state force out of the solver that accurately represents the forces applied to the wing geometry while the car is in steady state motion. The 2D space setting was kept at its default

value of planar, as the geometry was not axis-symmetric and needed to be modelled in its complete form to allow for a solution.

4.3.3 Problem Setup - Models

The second tab of the ‘Problem Setup’ menu allow for the identification of the flow model to be used. It was clear from the literature review that the viscous model was the correct model to choose. As such, the rest of the model selections were turned off and the viscous model option was opened for editing.

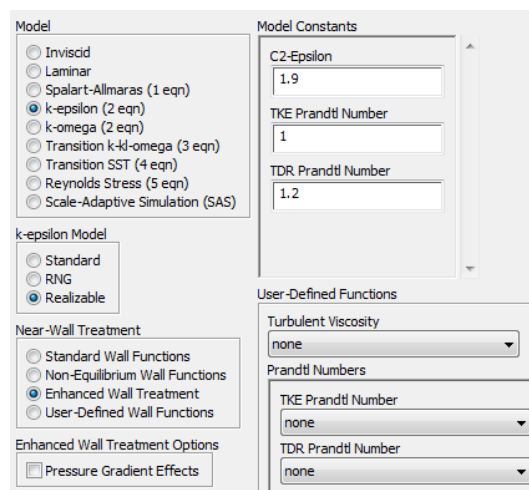


Figure 4.8 – The Model Menu

Based upon the findings of the literature review, the two equation k-epsilon model was selected. The model specific setting was changed from the standard model to the realizable model because of its ability to allow for positive shear stress in the turbulent flow through the variation of the C_{μ} term in the calculation of the turbulent viscosity.

This means that the solver can vary the properties based upon the location of the turbulent eddies, allowing accurate calculation of turbulence in both near-wall and free stream flow in the same solving process. The standard model sets the C_{μ} term to a constant value that is widely accepted for high Reynolds number flow. As such, the near wall calculation in the standard model lacks the accuracy of the renormalization

group (RNG) and realizable models. The renormalization model was not considered to be ideal for this scenario as it also sets the C_μ term to a constant value, closer to the accepted value for low Reynolds number flows.

The near wall treatment setting required a large amount of experimentation in order to settle upon a final value. Initially the standard wall functions were used, as the mesh was considered to be refined enough to allow for the accurate calculation of near wall velocity change without applying specific conditions. Upon inspection of the results, it was pointed out that the residual Y^+ term was several orders of magnitude too large, well outside the accepted range for the term.

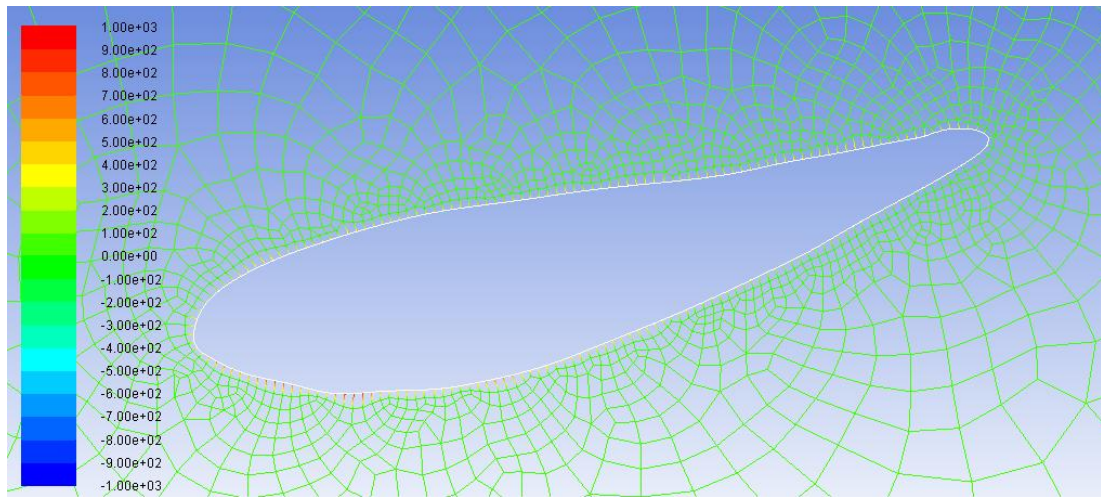


Figure 4.9 – Contours of Y^+ in the Standard Wall Function Model

Y^+ is a non-dimensional term, described by the following equation. It details the distance of the flow from the wall according to turbulent boundary layer theory.

$$y^+ \equiv \frac{u_* y}{\nu} \quad (3.1)$$

where $u_* =$ friction velocity (ms^{-1})

$y =$ distance to nearest wall (m)

$\nu =$ kinematic viscosity (m^2s^{-1})

The mesh was already very fine and further mesh refinement would have greatly increased the processing time required for each wing angle and speed combination. The properties of the flow also exceeded the limitations of the standard wall function model, as described in Section 4.13.3.2 of the ANSYS Help guide. The model was expected to experience boundary layer separation resulting from severe pressure gradients and low Reynolds number flow through a gap.

For these reasons, the non-equilibrium wall function model needed to be considered, at a minimum. The application of the non-equilibrium model saw the value of Y^+ fall well below the accepted upper range of 300 and it remained the main model used in the solution process. All other settings in the viscous model menu remained at their default values, as per the accepted practice described in the ANSYS Help file.

4.3.4 Problem Setup – Materials & Cell Zone Conditions

The next step in the ‘Problem Setup’ menu was to define the materials within the flow. The correct settings had already been imported through the reference to the mesh file, with the fluid body having properties of atmospheric air and the solid edges of the vehicle retaining surface properties of aluminium. This was deemed adequate as painted aluminium makes up a large portion of the vehicle body.

After this, the cell zone conditions tab was checked to ensure that the only mesh zone considered to be flowing was the fluid body that filled the void between the domain walls and the vehicle contour. This meant that the FLUENT solver recognised that it was to analyse a moving body of air passing over a stationary vehicle.

4.3.5 Problem Setup – Boundary Conditions

Next, the boundary conditions were defined. Each of the named selection elements, described in Figure 4.7, can be assigned properties based upon their expected interaction with the flow. The road, wing and vehicle contour edges were specified as no-slip stationary walls. This meant that the velocity at the wall would be 0 m/s and

the turbulent boundary layer would develop in the manner described in the literature review. The wall roughness for each was kept at the standard value of 0.5 with a roughness height of 0.

The free stream wall was set to be a stationary wall of specified shear, with the x and y components of this shear set to 0 Pascals. This tells the solver that the free stream is a dummy wall that has no effect on the local turbulence.

The inlet and outlet were automatically identified by the FLUENT solver. The outlet conditions did not need to be configured beyond their default settings as the model was not required to consider the effect of turbulent backflow at the outlet.

The inlet is possibly the most important section to define for the creation of an accurate model. It defines the manner in which momentum enters the model, while also providing a scale by which the turbulence can be formulated.

The image shows a screenshot of the FLUENT software interface for defining inlet conditions. The 'Zone Name' field is set to 'inlet'. The 'Momentum' tab is selected, and the 'Velocity Specification Method' is set to 'Magnitude, Normal to Boundary'. The 'Reference Frame' is set to 'Absolute'. The 'Velocity Magnitude (m/s)' is set to 70, and the 'Supersonic/Initial Gauge Pressure (pascal)' is set to 0. The 'Turbulence' section is expanded, showing the 'Specification Method' set to 'Intensity and Length Scale', with 'Turbulent Intensity (%)' set to 5 and 'Turbulent Length Scale (m)' set to 0.625.

Figure 4.10 – Defining the Inlet Conditions

The velocity was specified as a magnitude with its vector normal to the boundary wall. This was the best way to set up a model that reflected the motion of a fast moving vehicle along the road surface. The velocity was stepped up in increments of 5 m/s within the ranges of 20 m/s and 70 m/s for all the wing angles considered. This allowed the model to determine whether optimum wing angles changed with respect

to the velocity with which the car was travelling. The reference frame was kept to absolute, in keeping with previous selections, while the gauge pressure was known to be zero.

Several settings were considered for the calculation of the turbulence within the specification method tab. Originally, the default values of k and epsilon were used to get a feel for what the flow would do under default settings. After some investigation into these values, it was decided that a pre-set turbulent intensity value should be used to ensure that the air entering the model would have turbulent intensity as per the following equation.

$$I \equiv \frac{u'}{u_{avg}} = 0.16 (Re_{D_H})^{-\frac{1}{8}} \quad (3.2)$$

where $I = \text{Turbulent Intensity} \quad (\%)$

$u' = \text{RMS Velocity Fluctuations} \quad (\text{m/s})$

$u_{avg} = \text{Average Velocity} \quad (\text{m/s})$

$Re_{D_H} = \text{Reynolds Number of Hydraulic Diam.}$

ANSYS Help states that in some modern wind tunnel facilities can have turbulent intensities as low as 0.5%, however this is significantly lower than naturally occurring turbulent intensity values. The Help guide goes on to state that values generally range between 1% and 10% for typical flows. With the aid of Dr Andrew Wandel, the selection of a common practise value of 5% for the turbulent intensity was used.

The length scale to be with this value is defined by the following equation.

$$l = 0.07 L \quad (3.3)$$

where $l = \text{Turbulent Length Scale} \quad (\text{m})$

$L = \text{Hydraulic Diameter} \quad (\text{m})$

$$= \frac{4A}{P} \quad (3.4)$$

The area considered was the square of the inlet height, 9.028^2 m^2 . The perimeter of that square was calculated as the wetted perimeter ($4 \times 9.028\text{m}$).

$$\begin{aligned}
 \textit{Therefore} \quad l &= 0.07 \frac{4(9.028)^2}{4 \times 9.028} \\
 &= 0.07 \times 9.028 \\
 &= 0.632 \text{ m}
 \end{aligned}$$

This value was then approximated to 0.625m for use in the specification of the turbulent length scale.

4.3.6 Problem Setup – Reference Values

The following reference values were used to allow the FLUENT Solver to calculate drag and lift coefficients for iterations in the solution process. These calculations are made according to the equations described in the literature review.

Table 4.3 – Reference Values

Reference Values	Values	Units
Area	1	m^2
Density	1.225	kg/m^3
Pressure	101000	Pa
Temperature	300	k
Velocity	Varied	m/s

The area could not be set to a specific value in this process, as the calculation of the drag co-efficient required the frontal area of the vehicle and the lift co-efficient required the area of the plan view. The value was kept at its default of 1.0 in order to act as a guide for quick comparison to other calculations.

The density, pressure and temperature were kept at fairly common values for local atmospheric conditions to allow for comparison between field testing data, in the event of their measurement in the future. The final value, velocity, was updated for each calculation to reflect the velocity defined in the inlet boundary conditions.

4.3.7 Solution Setup

The solution methods used for each spatial parameter are shown below in Table 4.4. These values are the default setting for the 2D, pressure based model. The Simple pressure velocity coupling uses a number of flux equations to compute the pressure field from the relationship between velocity and pressure corrections.

The gradient was kept at its ‘Least Squares Cell Based’ setting as this is the most resource economical gradient calculation method that uses linear connections between the centroids of adjacent cells to determine the gradient. For unstructured meshes, such as within this project, the accuracy is comparable to the more resource expensive node based solvers.

Pressure was kept at its default value due to a lack of available information on the other pressure settings within the ANSYS Help guide. The other continuity equations were kept at their default value of first order upwind for the same reason.

Table 4.4 – Solution Methods

Pressure-Velocity Coupling	
Scheme	Simple
Spatial Discretization	
Gradient	Least Squares Cell Based
Pressure	Standard
Momentum	First Order Upwind
Turbulent Kinetic Energy	First Order Upwind
Turbulent Dissipation Rate	First Order Upwind

Under relaxation parameters were kept at their default values for all solutions as the model would reach convergence quite quickly in all cases. In the event that convergence could not be reached, the pressure and momentum under relaxation factors can be freely adjusted provided their sum remains equal to zero. The density, body forces and turbulent kinetic energy factors were not used for this project.

The next step in setting up the solution parameters was to tell the solver which properties should be shown graphically during the iteration process of the solution. The first monitor to be defined was the residuals monitor. The residuals monitor

describes the variance of each of the following variables between iterations of the solution. If the variance between successive iterations is smaller than the absolute criteria for that value, the calculation is considered to be converged. The default setting for residual convergence is to drop three orders of magnitude, or 1×10^{-3} . In order to calculate a more accurate solution, the convergence tolerance was dropped another order of magnitude to 1×10^{-4} .

Table 4.5 – Residual Monitors

Residual	Absolute Criteria
Continuity	0.0001
X-Velocity	0.0001
Y - Velocity	0.0001

Drag and lift monitors were also modified within this section to allow the solver to create a graph of the drag and lift coefficients throughout the solution process. This was used to give an early indication of potential errors within the setup as these values should remain fairly constant over the range of speeds tested.

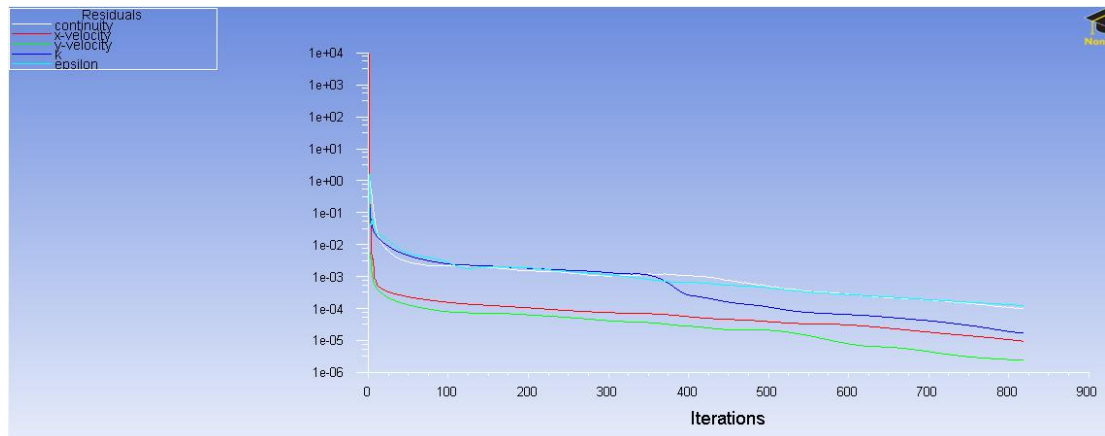


Figure 4.11 – Convergence of Scaled Residuals (818 iterations)

The next step in the process is to initialize the solution. This tells the FLUENT solver to discard all previous input parameters and replace them with everything that has been altered. After this, the maximum number of iterations can be defined. For the low-medium angles of attack the maximum iterations needed were 1000, with most

converging well inside this range. However, for the very steep wing angles the maximum allowable iterations was extended to 1500 to allow the FLUENT solver more time to calculate a steady solution.

After this, the solution was initiated and the calculation began. Once completed or converged, graphics of the velocity and pressure fields can be obtained and analysed in order to understand the nature of the steady state flow scenario. Y^+ values were checked for each case, with all lying well below the upper limit of 300. After passing the checking process, the reports tab was used to print resultant force vectors in the [1 0 0]' and [0 1 0]' directions for both the wing and the vehicle body geometries. These forces were used as the resulting drag and lift forces respectively and will be presented in the results section.

This process was run in parallel on multiple computers over a period of 1 week in order to calculate drag and lift forces for a complete range of attack angle and speed combinations that are feasible for the application of an active aerodynamic aid. Speeds ranged from 20 m/s to 70 m/s at increments of 5 m/s, allowing for the modelling of the range of speeds at which the vehicle can travel in standard form. Attack angles ranged from $+10^\circ$ to -80° to allow comparison of plausible angles.

		Forces (n)		
Zone		Pressure	Viscous	Total
body		174.66896	19.981234	194.65019
wing		1.0334549	1.3463099	2.3797648

Net		175.70242	21.327543	197.02996
Forces				
		Forces (n)		
Zone		Pressure		
body		(174.66896 -1181.6659 0)		
wing		(1.0334549 -70.724197 0)		

Net		(175.70242 -1252.3901 0)		
Forces - Direction Vector (0 1 0)				
		Forces (n)		
Zone		Pressure	Viscous	Total
body		-1181.6659	1.4218105	-1180.2441
wing		-70.724197	-0.13851991	-70.862717

Net		-1252.3901	1.2832906	-1251.1068

Figure 4.12 – Resultant Forces on Relevant Zones

5 Methodology - Stress Analysis of Wing Blade

This section describes the process of determining the ideal material to use in the manufacturing of the wing, based upon the critical criteria of adequate strength and minimal mass.

5.1 Material Selection

The wing needs to be capable of withstanding the rigorous dynamic and static loading cases involved with applying lift forces and rotating in the free stream flow at high speeds. The standard material for the TRD3000GT wing is fibreglass, which is an out-dated car body material of very low strength. The results, shown in Chapter 4, show the reasons that fibreglass has remained suitable for application at the standard -3° angle of attack, with resultant forces of approximately 600 N/m. This is less than half the maximum force applied to the wing at larger angles of attack.

In recent years, the reproduction process of the standard TRD3000GT wing blade has been updated. New wing blades are available that are constructed out of carbon fibre, an increasingly prominent woven material that has exceptional tensile strength along the length of its fibres. As one of these reproduction blades is available for testing this material will be considered for the base material of the active wing. The selection of carbon fibre as a base material was reinforced by its use in the 'Active Aero' dynamic rear wing that was developed at the Massachusetts Institute of Technology.

Another tried and tested material for use in car bodies is aluminium. Should the carbon fibre material fail the material testing process, testing process would be extended to include this material as a possible replacement.

5.2 Near Field Strain Mapping of Existing Wing Blade

Near field strain mapping is the act of physically determining the amount of strain a surface experiences under specific load conditions. Near field analysis details that the strain measured reflects the localised strain at the surface, rather than a full indication of strain throughout the body. This analysis was used in an attempt to verify the accuracy of the computer based, finite element model.

The first step in this analysis process is to select a suitable gauge for the application. The gauges were to be applied to a privately owned TRD wing blade, which meant that destructive analysis was completely ruled out. It also meant that the gauges should be as small as feasibly possible, in order to reduce the amount of damage done to the carbon fibres. As a result of these conditions, the following strain gauges were selected.

Table 5.1 – Selected Strain Gauges

Strain Gauge Properties	Strain Gauge		
	SR-4	FLA-2-11-3I	PR-5-11
Manufacturer	Vishay	TML	TML
Type	Uni-Axial	Uni-Axial	Tri-Axial
Gauge Length	4mm	2mm	5mm
Grid Resistance	120	120.4	120
Gauge Factor	2.095	2.11	2.06

These strain gauges are a suitable tool for measuring the amount of surface strain, given that the University of Southern Queensland had granted access to their Vishay strain computer that allows for the instantaneous calculation of strain from the information the sensors provide. Each of these sensors has an inbuilt grid resistance, shown above. As a force is applied to the gauge along its measurement axis, the copper wire that makes up the foil stretches and its cross section shrinks as a result. This increases the amount of resistance the gauge has on electricity passing through.

The next step was to determine the sections on the body where these gauges should be applied to give the best indication of maximum strain values. Due to the theory that the centre of pressure was expected to be located at approximately 25% of the chord length behind the leading edge, this was chosen as a location for the majority of the gauges.

The first of the gauges were applied to the upper surface of the aerofoil. The location for the first gauge was chosen to be at a distance of 90mm from the left hand face in the x-direction, while remaining along the centre of pressure line at a distance of 55mm in the y-direction. The second gauge was also kept 55mm behind the leading edge and offset 50mm left of the centreline in the x-direction. This would allow weights to be hung along the centreline without damaging this gauge.

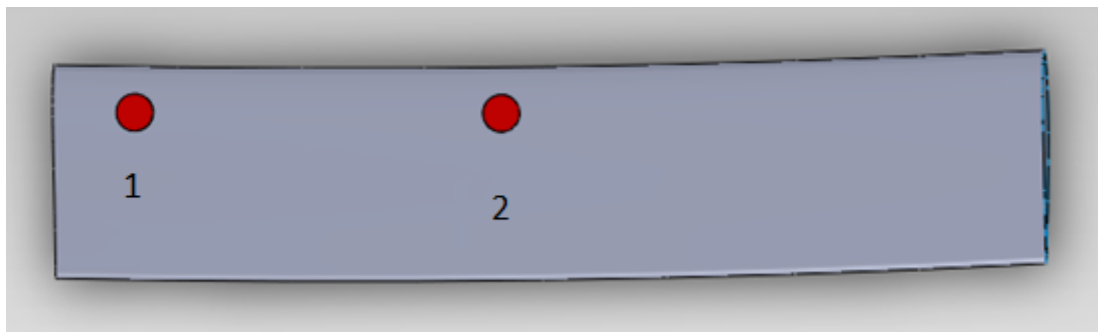


Figure 5.1 – Strain Gauge Locations – Upper Wing Surface

The wing surface needed to be prepared before the strain gauges could be applied. This meant that the protective clear-coat paint covering the carbon fibres needed to be sanded back in the locations shown above. This would allow the gauges to read the strain within the fibres rather than the strain suffered by the paint. A fine grade wet and dry paper was used for this, as the protective coating was quite thin.

Once the fibres had been revealed, the surface was cleaned thoroughly using isopropyl alcohol and medical wipes in order to remove paint and dirt that had been separated from the wing surface. After this, more alcohol was used to clean a glass bench surface and the first strain gauge was placed gauge side down upon the glass. A length of clear sticky tape was then applied over the gauge, attaching itself to the gauge so that the gauge may be picked up and transported using the tape.

The first gauge was then taped into place over the cleared zone, shown as [1] in Figure 5.1. Indicators on the gauge surface allowed it to be aligned correctly along the x axis of the carbon fibres of the wing surface. The tape was then carefully peeled back to expose the rear of the gauge. A small amount of superglue was applied to the cavity in the cleared zone and the gauge was lowered back over the glue. Pressure was applied to ensure that the glue could set without the gauge twisting out of alignment. This process was repeated for the second gauge at [2].

A similar process was carried out for the lower wing blade surface. However it was anticipated that this tension side of the wing, would require more gauges in order to map the stain more accurately. As such, the following locations were selected.

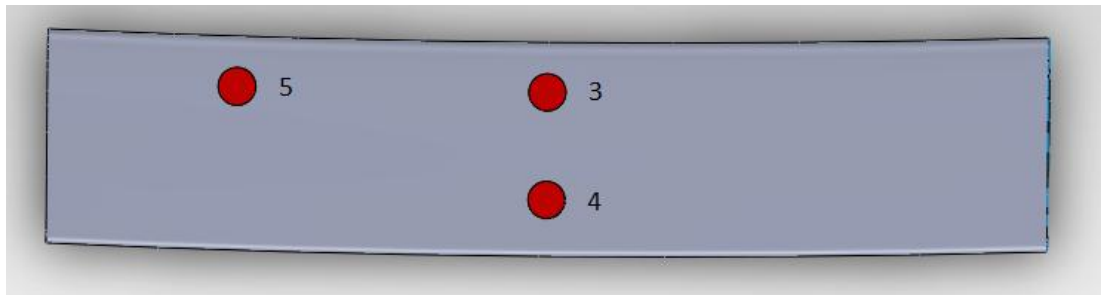


Figure 5.2 – Strain Gauge Locations – Lower Wing Surface

Gauge 3 was located at the very centre of the wing in the x-direction and along the 55mm centre of pressure line. Gauge 4 was also at the very centre of the wing, but spaced 60mm forward of the trailing edge. Finally, gauge 5 was placed 200mm from the left hand edge, also along the centre of pressure line.



Figure 5.3 – Wire Structure for Gauge 3

Once all of the gauges had been fixed, gauges 1 and 3 needed to have wires soldered onto their measurement terminals. Great care had to be taken to ensure that the wires of gauge 3 were not capable of touching, as they lacked the insulation coating of the other gauges.

Now that the wing was ready for testing, a suspension jig needed to be made to elevate the wing above the ground far enough that weights could be hung from the blade without striking the ground. Two stands were constructed that stood 800mm tall and each utilised a bracing support to prevent excessive bending during the loading process. Once created, the wing was attached and the test was run. The final assembly of the wing, weights and stands is shown below.



Figure 5.4 – The Strain Testing Assembly

A rope was strung over the centre of the wing, 540mm from each face. A small metal chain was hooked together, through the dangling rope and then looped about a metal support at the base. Metal weights were then placed onto the metal support in increments of 5 lb. and the associated strain was measured.

These measurements were taken calculated by the Vishay P3 strain indicator that has the ability to convert a change in measured resistance into an equivalent change in the length of the copper strain gauge. A number of steps needed to be taken to ensure that this strain indicator was calibrated correctly.

The first step was to ensure that the grid resistance of the strain gauges and their respective gauge factors were input correctly. After this, a single gauge could be connected to the indicator using two wires, a positive and a negative. For this application, the half bridge technique was used.

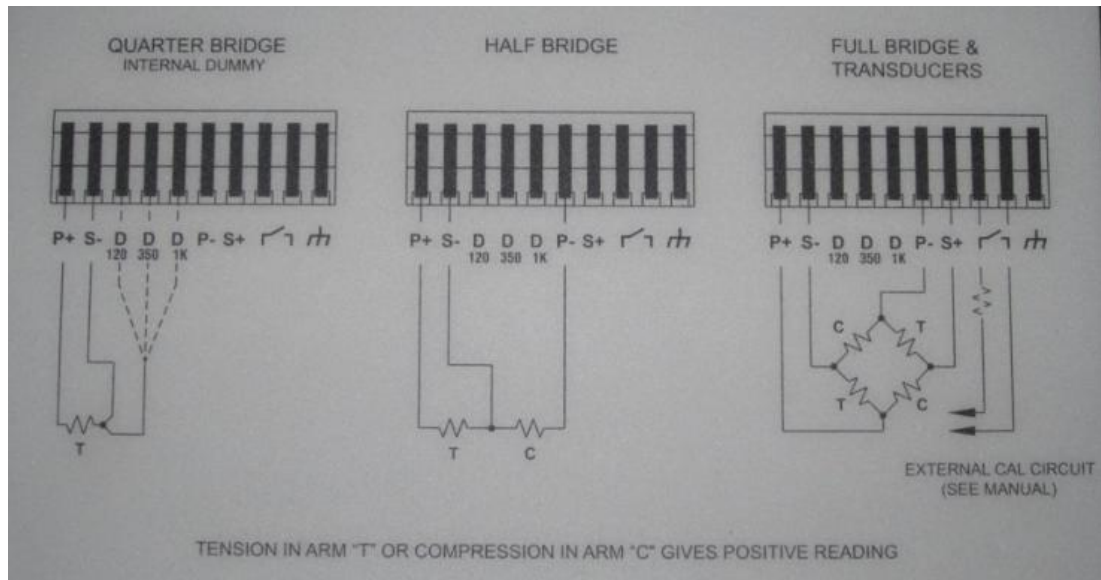


Figure 5.5 – The Half Bridge Connection

This half bridge technique uses a dummy wire to connect terminals S- and P-. The two wires connected to the strain gauge could then be inserted into P+ and S- in order to set the machine up to read positive values of strain as tension and negative values as compression. After this, the units of micro strain ($\mu\epsilon$) were selected. This meant that a reading of 1 unit on the device would correlate to a strain of $1\mu\text{mm/mm}$.

After this was defined, the indicator would give a base reading for the strain, based upon the amount of extra resistance detected within the bridged circuit that could not be attributed to the strain gauge. This extra resistance can be attributed to the length of the wires and the quality of the soldering. Before any weight was added to the wing, the system was balanced by using a tare function. This resets the zero position of the strain to account for the resistance.

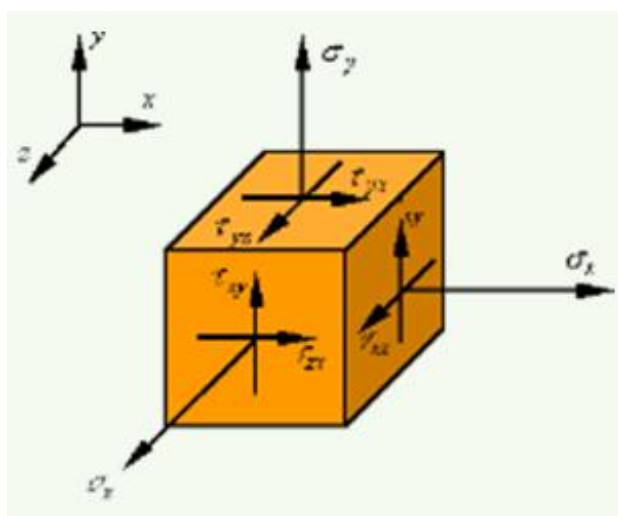
Once tared, the weights were added in 5 lb. increments up to 55 lbs. with the strain for each increment recorded. The test was performed individually for each strain

gauge. Gauge 3 was the first to be tested as it was anticipated, based on beams deflection, that this zone would experience the most tensile strain. Once it was established that the maximum weight available did not exceed the 1000 $\mu\epsilon$ limit advised by Dr Jayantha Epaarachchi, the other gauges were used.

5.3 Finite Element Analysis of Wing Blade

Finite Element Analysis (FEA) is the process of applying mathematical, structural principles to mesh geometries in a similar manner to the method used for Computational Fluid Dynamics. The first step taken in this process was to import the 3D TRD wing file, shown in Figure 3.3, into a computational analysis package called Strand7.

This package was chosen over ANSYS due to its improved ability to model composite and fibre based features where material properties are isotropic. An isotropic material has different strength properties when loaded in different directions, unlike the orthotropic materials like metals that have consistent material properties in all directions. A comparison of each material type is shown below in Figure 5.6.



For Orthotropic:

$$\sigma_x = \sigma_y = \sigma_z$$

$$G_x = G_y = G_z$$

For Isotropic:

$$\sigma_x \neq \sigma_y \neq \sigma_z$$

$$G_x \neq G_y \neq G_z$$

Figure 5.6 – Isotropic versus Orthotropic

The ANSYS solver excels at analysing orthotropic materials, however the use of the ANSYS solver to analyse isotropic materials requires significant experience that was not achievable within the project time span. After the wing was imported, unnecessary features were deleted away until only the internal layer of the wing blade existed as a cluster of surfaces. This allowed for a surface mesh to be created using the ‘Automesh’ command in the ‘Tools’ menu. This surface mesh is shown below in Figure 5.7.

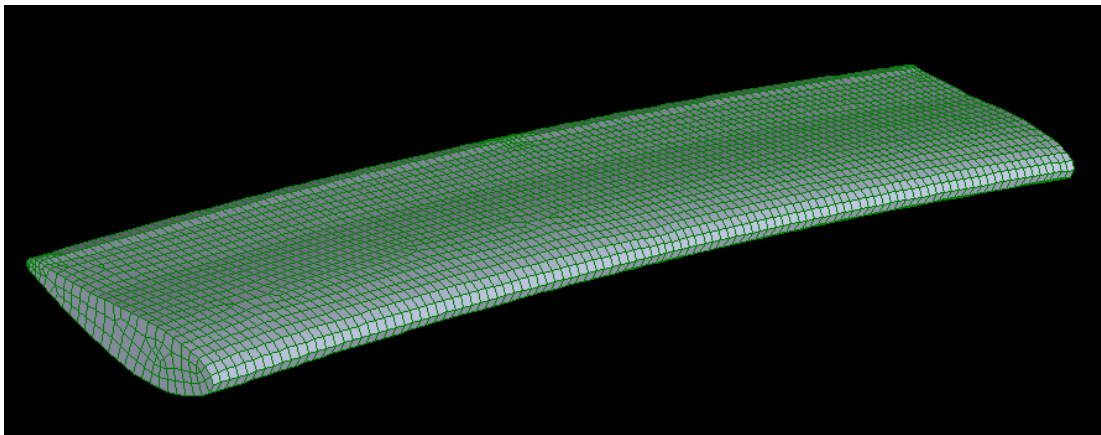


Figure 5.7 – The Wing Mesh

The original features of the wing import could then be deleted completely, leaving only the mesh elements in the Strand7 file. The properties of the surface mesh could then be defined within the ‘Ply’ section of the ‘Property’ menu. The input material properties are shown below.

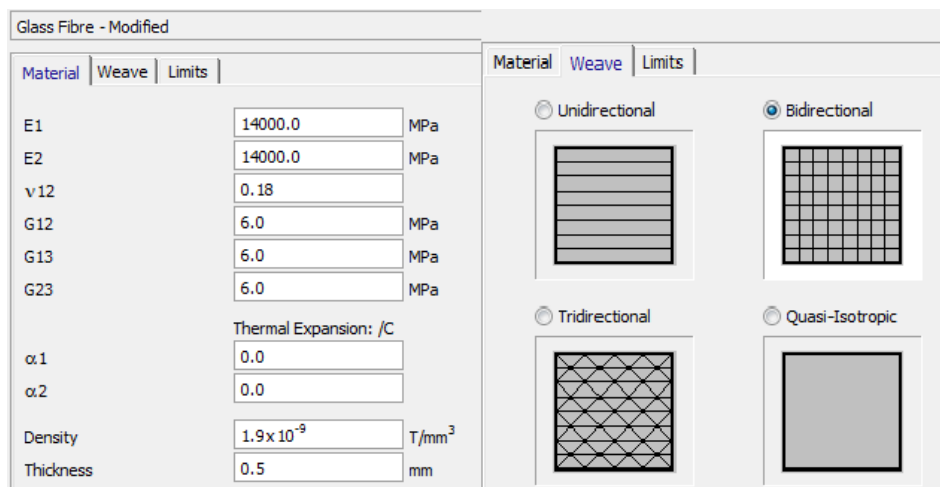


Figure 5.8 – The Ply Properties

These values were suggested by Dr Epaarachchi as the base properties of the carbon fibres present in the TRD 3000GT wing. It is clear from close up comparison that the fibres within the top layer of the wing run at 0° and 90°, as per the bidirectional ply style.

Vernier calliper measurements of some carbon fibre trim that came with the wing identified that the total thickness of the fibre layer was 2.0 mm, which led to the assumption that it consisted of 4 layers of carbon fibre wrap, where each layer was 0.5 mm thick. This is the assumption that was adjusted in the modelling process to allow the electronic model to conform to the values of the experimental data. The number of layers within the surface mesh is defined in the ‘Laminate’ section of the ‘Property’ menu.

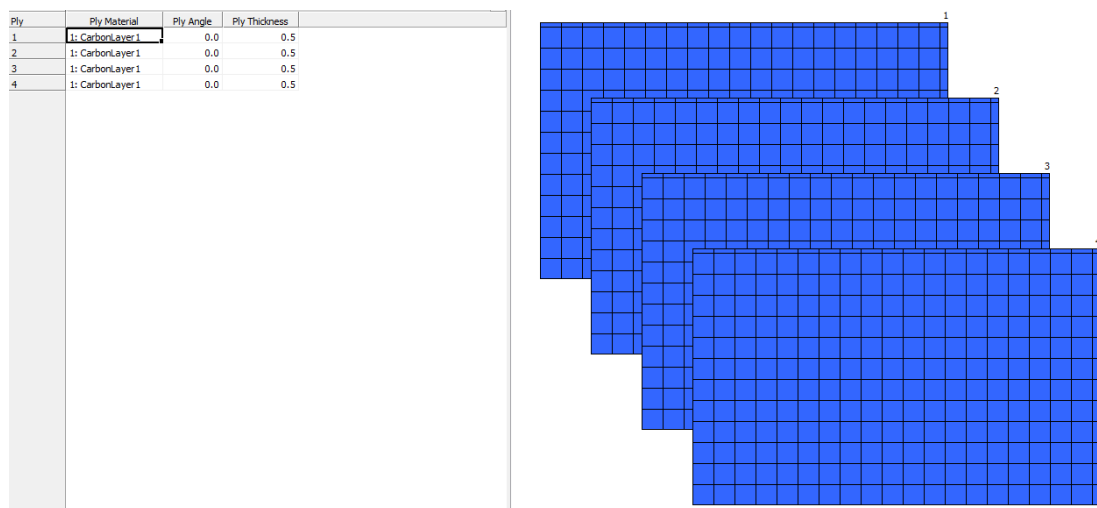


Figure 5.9 – The Laminate Properties

Once the mesh properties had been defined, the model constraints were detailed within the load and freedom cases menu of the Strand7 solver. The first mesh elements to be constrained were the side faces of the wing geometry. Each of these faces was assumed to be completely restricted from movement in any direction. This assumption was made to simplify the possible bending configurations of the wing blade and limit the deflection and strain to the upper and lower surface of the wing blade. These constraints are shown in pink within Figure 5.10 on the following page.

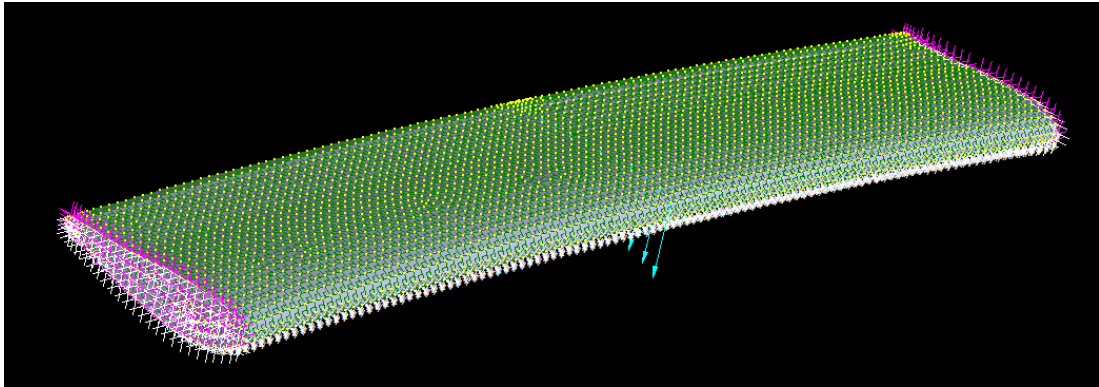


Figure 5.10 – The Load Case

After this, 13 nodes were selected along the centreline of the upper wing surface. Any force used within the near field analysis can be evenly distributed across these nodes, according to the equation below, in order to simulate the effects that this load has on the deflection and strain of the wing.

$$F_{node} = \frac{F_{applied}}{13} \quad (5.1)$$

Once the values of the strain at any three of the five strain gauge locations, defined in Figures 5.1 and 5.2, were calculated to be within 10% of the experimentally obtained data, the wing mesh was considered to be verified for all load cases. This meant that the maximum resultant force from the FLUENT analysis could be applied to the wing in order to determine if the wing blade would break.

This was done by selecting all of the nodes on the top surface and distributing the maximum force condition from Appendix B. Should the simulation show that the strain and deflection of the wing blade were within the material limits, the wing blade would be considered strong enough for use in the application.

6 Results and Discussion

This chapter describes the results of the computational fluid dynamics analysis and relates the results to the implications that they should have on the vehicle dynamics. After this, the results of the material testing are presented and linked to the finite element analysis of the wing blade.

6.1 Computational Fluid Dynamics Results

This section discusses the results obtained from the comprehensive FLUENT analysis detailed in Chapter 4. The raw data obtained from these experiments too details to be included within this section, but is available in Appendix B. Only the key flow scenarios are discussed in this chapter in order to focus on the important deliverables of the project.

6.1.1 Maximum Downforce Angle

The maximum downforce angle describes the position at which the wing blade transfers the most force downward, through its supports and onto the rear of the vehicle. This increases the normal force that reacts upward through the rear wheels, increasing vehicle traction according to Equation 2.5, which subsequently increases the speed at which the vehicle can navigate a corner according to Equation 2.6.

For all the wind speeds tested, maximum downforce has been shown to occur when the blade is declined at have a -15° angle of attack. This is shown below for the 70 m/s wind speed as an indication of the characteristic nature of the data for all wind speeds. The comprehensive raw data list is shown in tabular form within Appendix B, details the magnitude of the forces at all the wind speeds tested. Furthermore, the graphs within Appendix C describe the effect that the angle of attack has on the magnitude of the forces imposed on the wing.

Table 6.1 – Wing Angle Data at 70 m/s

Velocity = 70m/s			
Wing Angle	Downforce (N)	Drag (N)	Downforce/Drag
-10.00	-111.69	76.33	-1.46
-5.00	154.54	47.89	3.23
0.00	596.10	13.17	45.26
5.00	894.44	27.16	32.93
10.00	954.14	83.45	11.43
15.00	1238.80	130.64	9.48
20.00	1134.09	226.04	5.02
25.00	925.04	351.58	2.63
30.00	916.18	455.44	2.01
35.00	792.31	521.18	1.52
40.00	604.86	483.89	1.25
45.00	600.76	571.31	1.05
50.00	732.84	813.22	0.90
60.00	656.99	1004.93	0.65
70.00	378.79	880.22	0.43
80.00	243.53	948.91	0.26

Key values have been highlighted for each variable. These points are reflected as maximums in the following graph of forces versus wing angle in Figure 6.1.

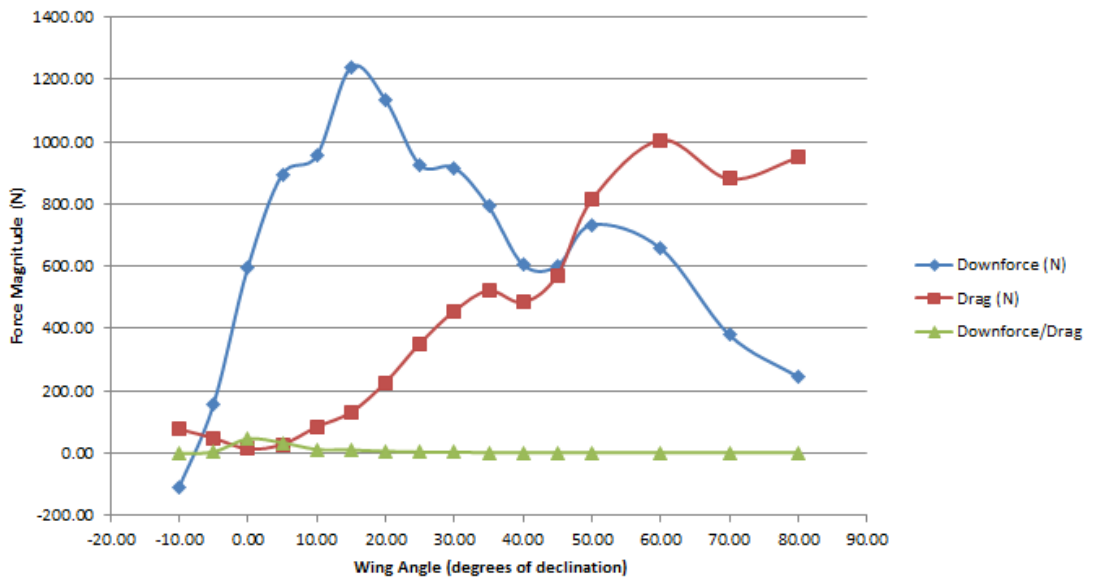


Figure 6.1 – Force versus Wing Angle (70 m/s)

Figure 6.1 shows that lift (blue) starts to decrease rapidly once the wing is rotated past the optimum -15° angle of attack. This is attributed to wing stall and is the result of the separation of flow off the aerofoil surface, greatly reducing its ability to produce lift forces. Figure 6.2, shown below, describes the pressure field about the vehicle and shows why the -15° angle of attack is so effective at producing negative lift forces.

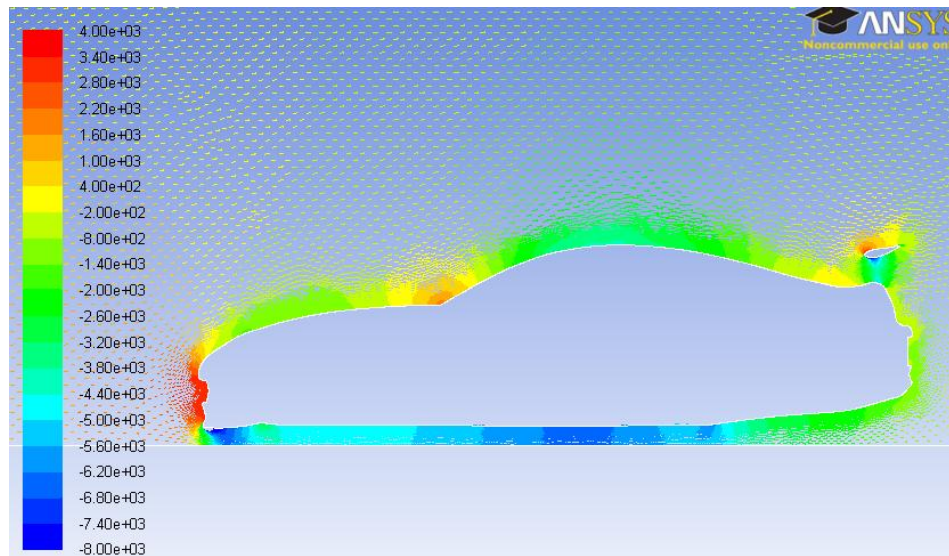


Figure 6.2 – Velocity Vectors Coloured By Static Pressure (Pascal)

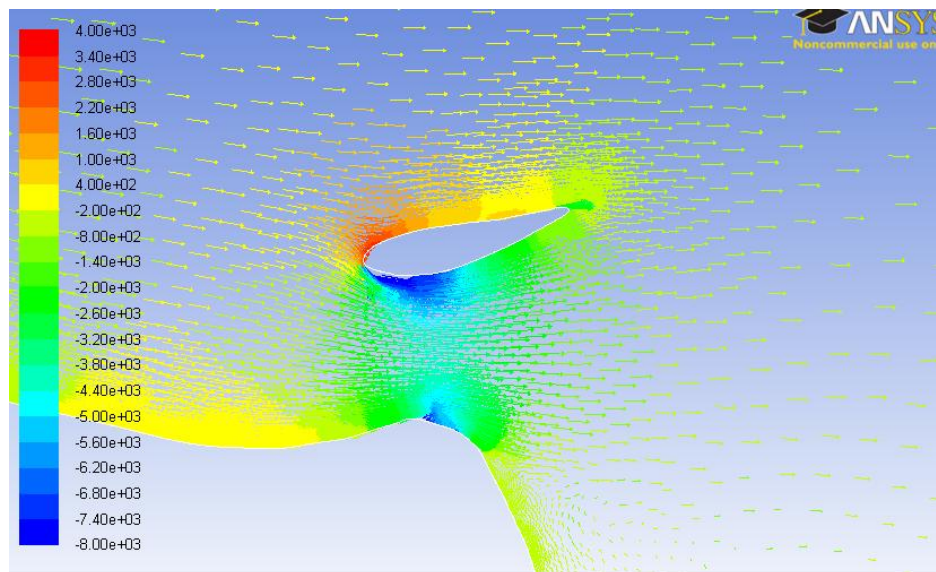


Figure 6.3 – Velocity Vectors Coloured By Static Pressure (Pascal)

Figure 6.2 shows that the 2D model has incorrectly modelled the pressure of the air flowing beneath the vehicle. Hucho (1987) shows that this is a common occurrence in two dimensional flow simulations that require complex under-body geometries such as tyres and wheels to be ignored in order to allow flow to pass beneath the vehicle. Figure 6.4 describes these increases.

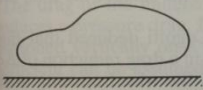
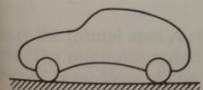
	c_D	c_L	$A \text{ (m}^2\text{)}$ $M \text{ 1:2}$
	0.073	-0.044	0.407
	0.157	-0.009	0.462

Figure 6.4 – Addition of Wheels to a car-like body (Hucho 1987 p165)

The geometry over the top of the vehicle has not been simplified to the same extent and as a result, the figures produced by the FLUENT solver can be presented with a modest degree of accuracy. The low static pressure on the bottom face of the wing in Figure 6.3 can be attributed to the high velocity experienced within that zone in Figure 6.5. This is a visual representation of Bernoulli's principle in Equation 2.3. The high pressure on the upper side of the wing pushes the wing downward and provides the large downforce detailed in Table 6.1.

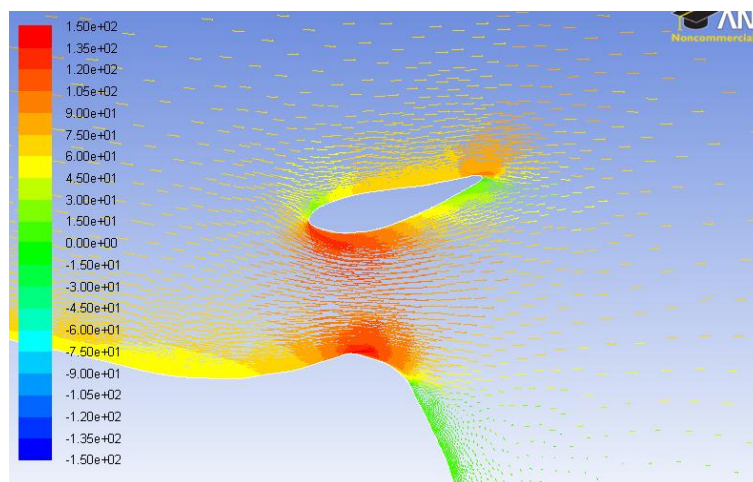


Figure 6.5 – Velocity Vectors Coloured By Velocity (m/s)

The range of the velocity scale has been adjusted so that green zones represent points on the vehicle at which stagnation is occurring. As expected the front and rear of the vehicle are large zones at which air is trapped. The leading and trailing edges of the aerofoil are also stagnation points. The fact that the plots shown in this section are consistent with the aerodynamic theory allows further confidence in the output forces.

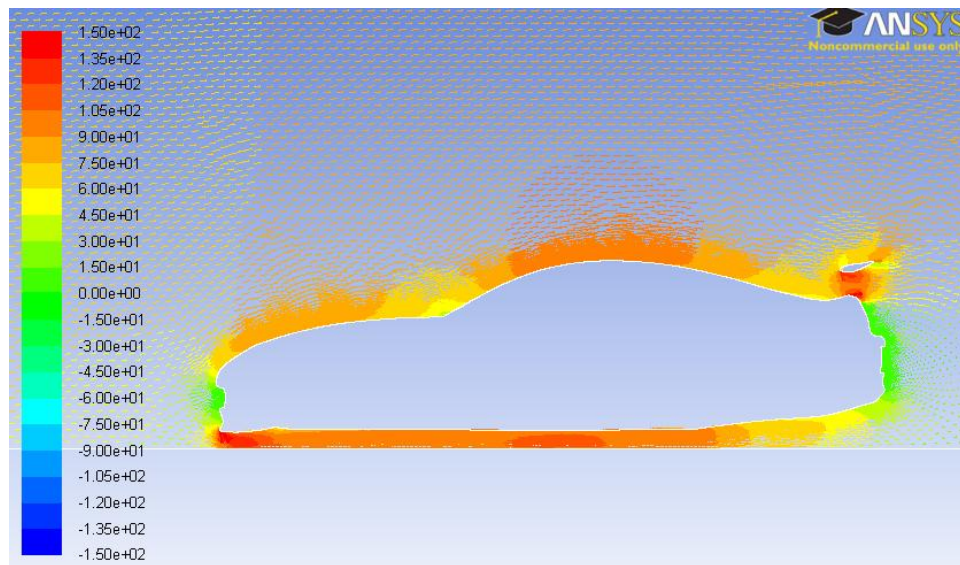


Figure 6.6 – Velocity Vectors Coloured By Velocity (m/s)

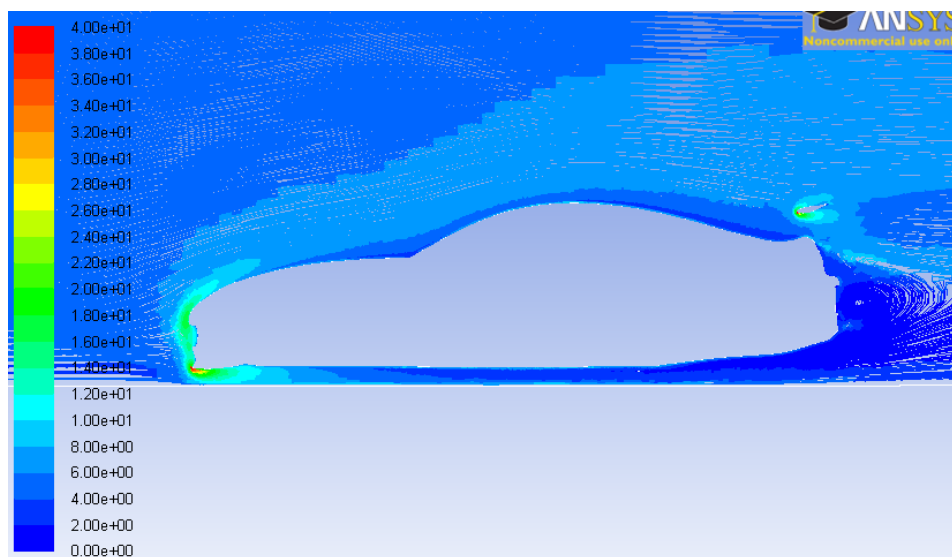


Figure 6.7 – Pathlines of Turbulent Intensity (%)

Figure 6.7 details where the turbulence is at its most intense. As expected, the most severe turbulence occurs as a result of the initial interruption of the free stream flow at the nose of the vehicle and the leading edge of the wing blade. Within these zones, it is the points where the geometry is sharpest that creates the most intense turbulent flow (shown in red). The thick blue zone at the rear of the car in Figure 6.7 shows where the very slow moving air from Figure 6.6 is mixing with a relatively small amount of energy.

As the FLUENT solver has calculated values for a blade depth of 1m in the z direction, the output values need to be adjusted by a factor of 1.08 in order to modify the results to reflect the true blade dimensions. It has been assumed that the end effects of air passing from upper side to lower side can be neglected due to the end turrets of the wing. Figure 6.8 shows a plot of how these modified -15° forces develop as the speed of the vehicle increases.

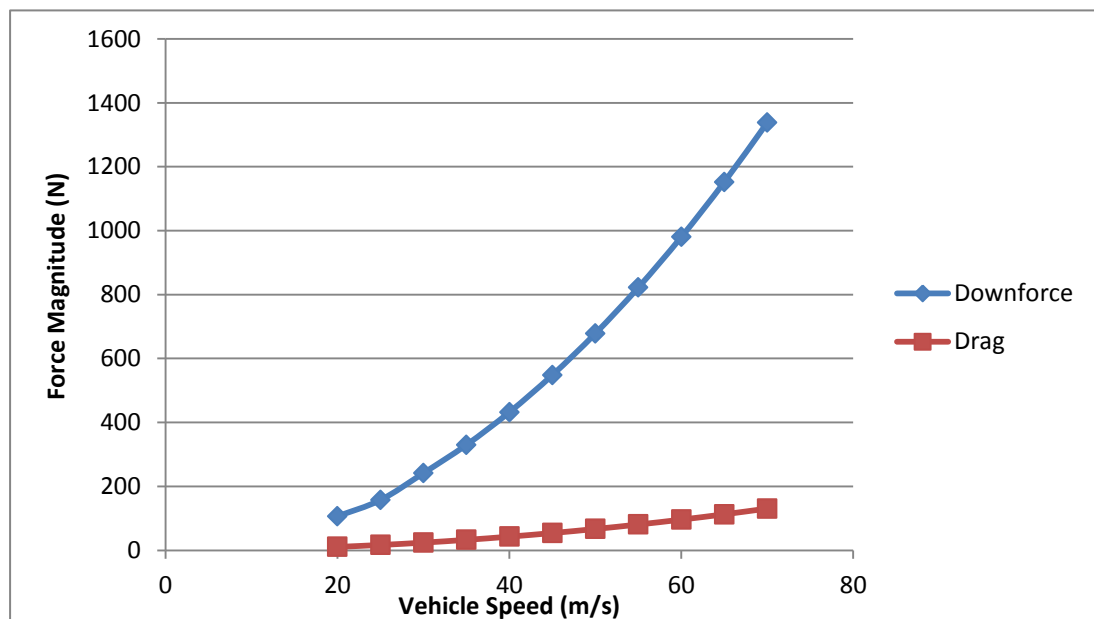


Figure 6.8 – The Maximum Downforce Wing Angle Forces (-15°)

This shows that at the optimum wing angle for generating maximum downward force, the lift force increases exponentially as the speed increases. This is expected due to the V^2 term within Equation 2.2. The drag force develops much more slowly and fails to reach a significant magnitude when compared to the lift force. As a result

of this slow development, the lift to drag ratio increases as the vehicle speed increases.

At 70 m/s the wing develops 1337 Newtons of negative lift force which equates to a mass of 136.4 kg being distributed evenly between the vehicles rear wheels. Interestingly, at a speed of 145 km/h (40 m/s) the negative lift generated by the rear wing is 432.1 Newtons which is 138 Newtons more than the standard rear wing produces at a similar speed. This 46.97% increase can be attributed to the more aggressive aerofoil design as well as the much steeper angle of attack.

6.1.2 Maximum Drag Angle

The maximum drag angle describes the position at which the wing blade transfers the most force in the opposite direction to motion. This increases the total drag forces incurred on the vehicle, allowing the car decelerate more quickly than usual. The magnitude of this drag force can be added to the vehicular drag described in Equation 2.1. The typical wing angle for maximum drag across the span of the speeds tested is the -60° angle of attack, as shown in Figure 6.1.

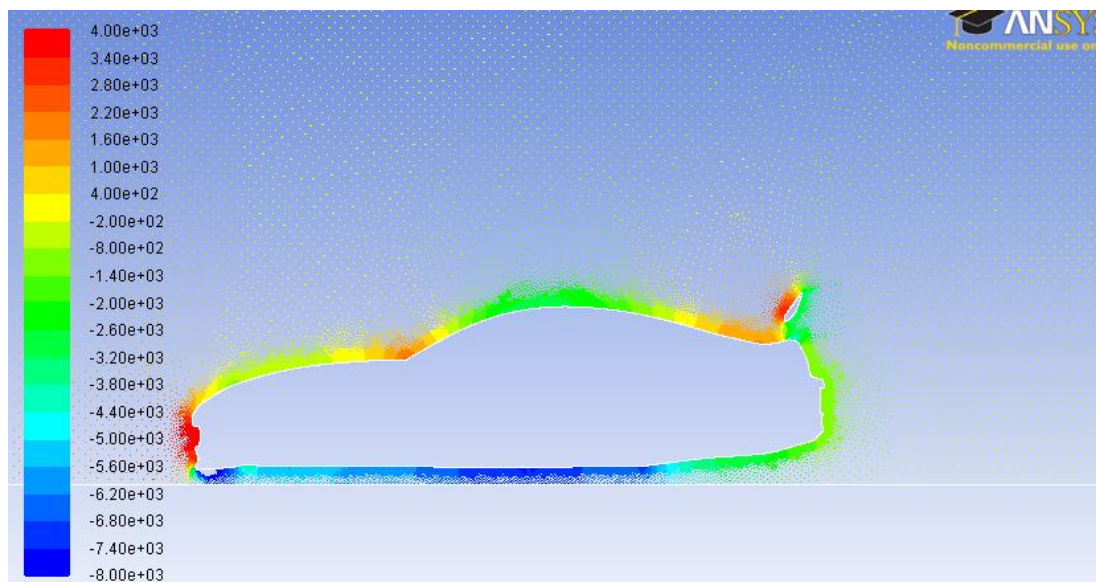


Figure 6.9 – Velocity Vectors Coloured By Static Pressure (Pascal)

Comparison of Figures 6.2 and 6.9 is possible, as both images utilize a consistent scale. It is clear from this comparison that the pressure on the upper surface of the wing is significantly greater in the -60° wing than on the -15° degree wing. Similarly, the pressure on the lower side of the wing has increased drastically as well however the pressure over the rest of the vehicle is essentially identical. This huge pressure increase at the wing is shown in more detail in Figure 6.10.

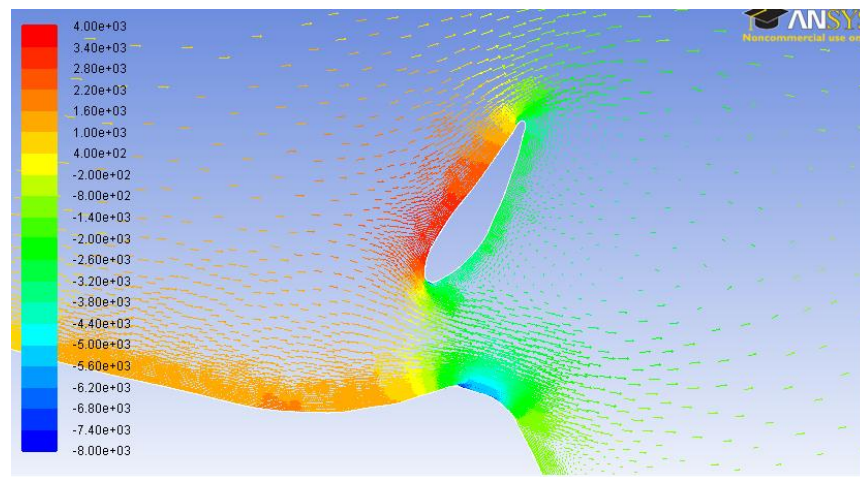


Figure 6.10 – Velocity Vectors Coloured By Static Pressure (Pascal)

The effect that this static pressure increase has on the velocity passing over this wing is shown below in Figure 6.11. Large stagnation zones are present on both sides of the wing and a stagnation zone has developed on the rear hatch of the vehicle as a result, greatly increasing the overall drag on the vehicle.

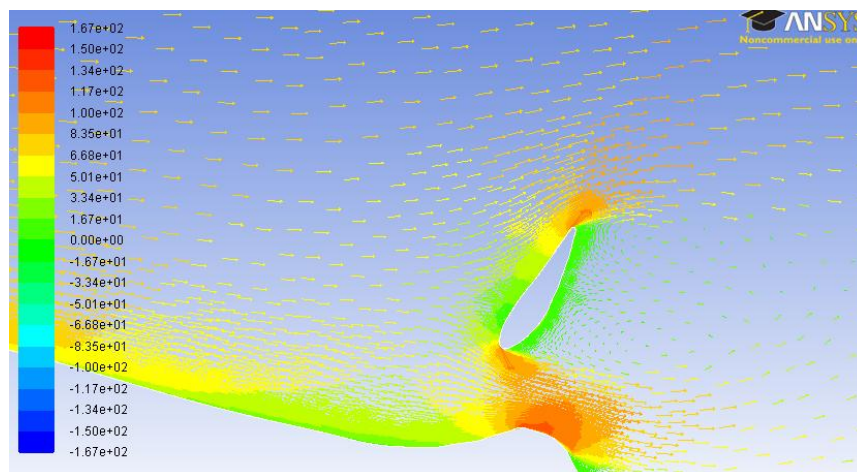


Figure 6.11 – Velocity Vectors Coloured By Velocity (m/s)

The turbulent intensity field at the rear of the vehicle is also changed significantly since the elevation of the rear wing. The small pockets of high turbulent intensity from Figure 6.7 have been replaced with a much larger zone with significantly more intense turbulence.

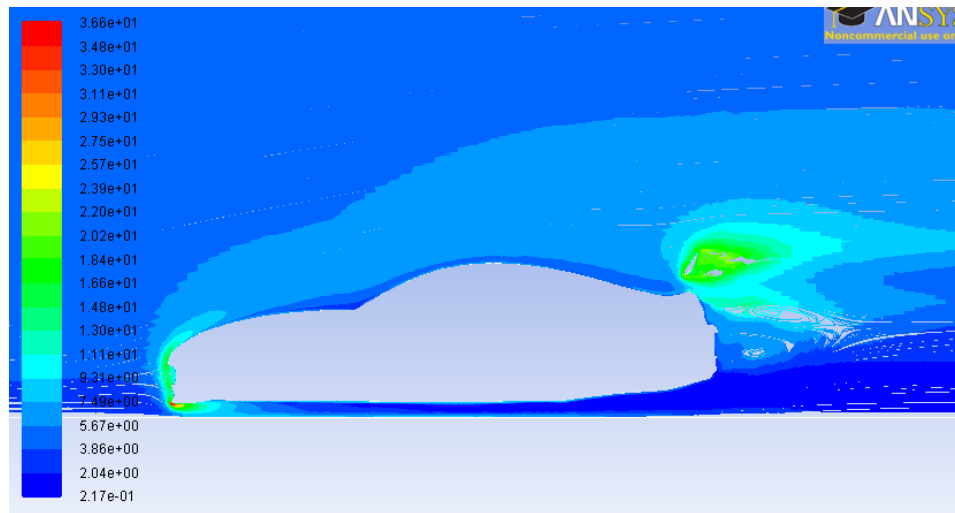


Figure 6.12 – Pathlines of Turbulent Intensity (%)

This larger pocket of turbulence carries on for several metres behind the vehicle before eventually dispersing once it meets the road surface. The effect that this has on the drag at the measured speeds is shown below in Figure 6.13.

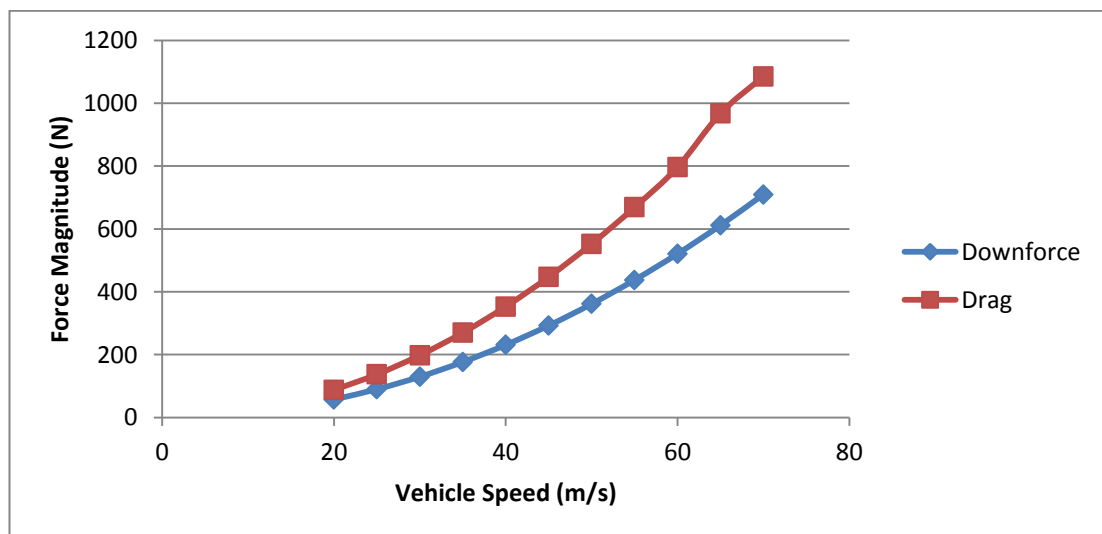


Figure 6.13 – The Maximum Drag Wing Angle Forces (-60°)

The maximum drag at 70 m/s has a magnitude of 1085 Newtons which equates to an extra 110.6 kilograms acting against the motion of the vehicle. This force will act instantaneously to slow a vehicle provided that it does not expend any more engine power to overcome the drag effect. The magnitude of the drag force decreases along the red curve shown in Figure 6.13 meaning that the braking potential of the wing is at its maximum at high speeds and loses effectiveness as the vehicle slows.

Unlike in Figure 6.8, the drag force for the -60° angle is far greater than the downforce generated. At 70 m/s the ratio of drag to lift is 1.53 compared to the maximum downforce wing that has a ratio of 0.105. Despite this, the magnitude of the downforce generated is still a respectable 710 Newtons, meaning that the rear of the vehicle is not likely to become unstable due to the effects of rear wing lift whilst the airbrake is in actuation.

6.1.3 Minimum Drag Angle

The minimum drag angle described the angle at which the drag forces acting on the wing are at a minimum value. The data in Appendix B shows that the drag of the wing is at its smallest when the wing is deployed at a 0° angle of attack in most cases. This means that for consideration of the wing forces alone, the 0° angle of attack incurs the least drag resistance of all the angles tested. The velocity profile of the airflow over the vehicle is shown below in Figure 6.14.

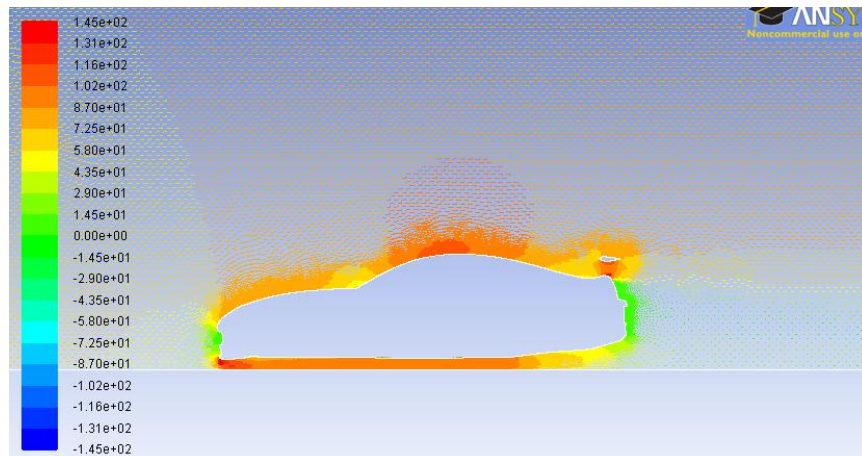


Figure 6.14 – Velocity Vectors Coloured By Velocity (m/s)

Due to the asymmetric nature of the TRD 3000GT aerofoil, the wing still produces a significant amount of lift when deployed at an angle of 0° . This is because the air on the underside of the wing is still required to travel faster than the wing flowing over the upper surface. The magnitudes of the forces associated with the wing at this angle are described below in Figure 6.15.

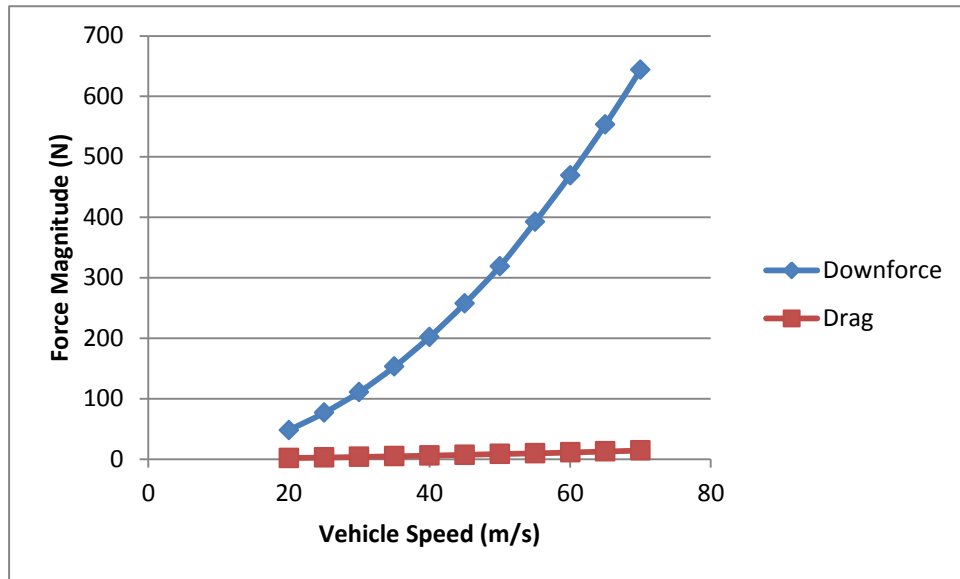


Figure 6.15 – The Maximum Drag Wing Angle Forces (0°)

The shows that the drag forces incurred on the wing are essentially negligible, reaching a maximum magnitude of 14.2 Newtons at 70 m/s. The turbulent intensity present within the flow at this speed is shown below in Figure 6.16.

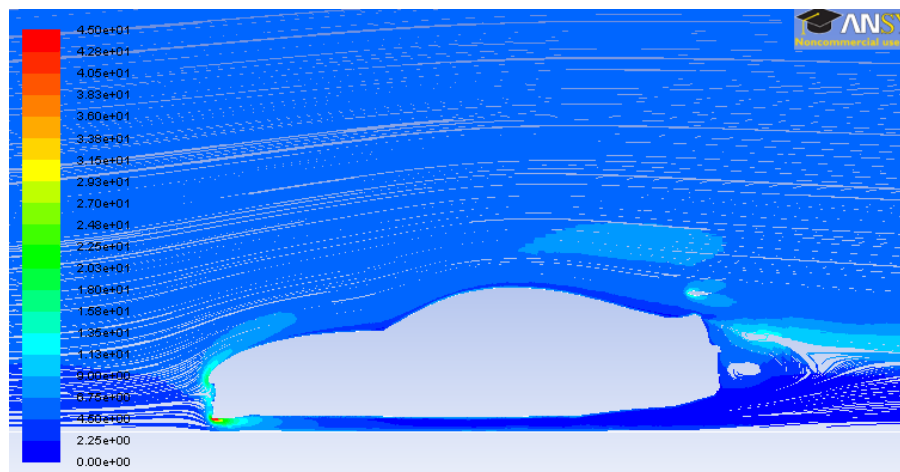


Figure 6.16 – Pathlines of Turbulent Intensity (%)

Figure 6.16 possesses a similar scale to the previous plots of turbulent intensity. Comparison between these plots shows that by decreasing the effect that the rear wing has on the turbulence of the flow over the rear of the vehicle, the total turbulent intensity over the vehicle is reduced as well.

Provided that the raw data results for the resultant forces on the vehicle body only require linear scaling in keeping with the values in Figure 6.4, the total drag of the vehicle can be reduced below its value for a wing at 0° . The raw data in Appendix B suggests that by rotating the wing to an inclined angle of 10° , the magnitude of the drag force acting on the car can be decreased by a factor of 0.91 (approximately 10% of the base drag). In this case, the rear wing acts more like a rear spoiler, by locally increasing the drag in order to reduce the overall vehicle drag.

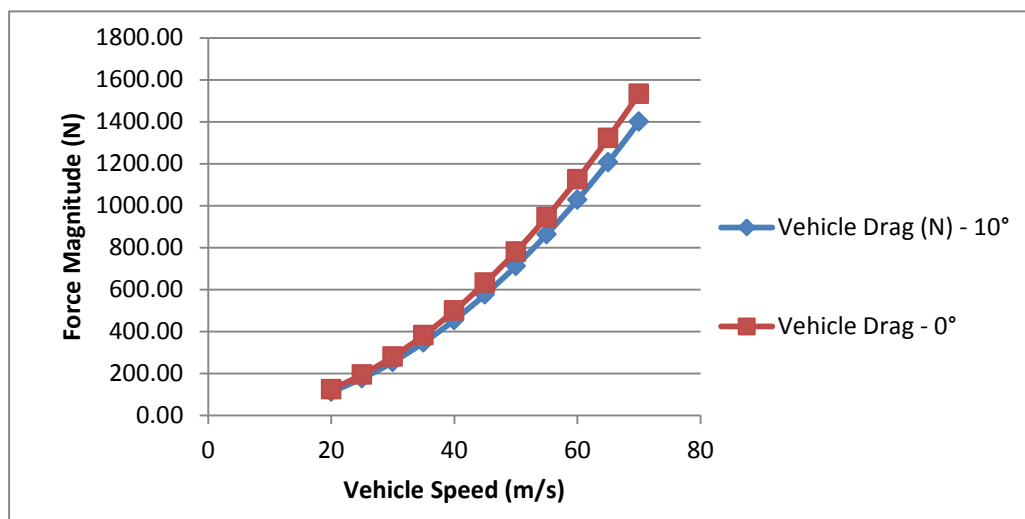


Figure 6.17 – Comparison of Vehicle Drag Forces

Unfortunately, a wing angle of 10° acts to decrease drag on the vehicle quite significantly, a side effect of this is a local production of positive lift forces at the rear of the vehicle. This makes the implementation of the 10° angle potentially dangerous, as the final result of decreasing the drag is to provide an upward force, decreasing the normal force at the rear wheel and decreasing tractive ability. For this reason the optimum wing angle for decreasing the overall drag of the vehicle without detriment to vehicle stability is 0° .

6.2 Dynamic Effect of Changes

In order to gauge the performance increase attained when replacing the standard supra wing with this active TRD 3000GT style wing, steady state cornering analysis was performed. This analysis uses the equations from Section 2.2 in order to determine the effect that increased normal forces can have on the vehicles maximum speed through a radial corner. When the vehicle is travelling on a highway or track, it is assumed that the road is either banked toward the inside of the corner or completely flat. The banked corner increases the natural cornering ability of a vehicle based on mechanical grip. As such, the flat road case was analysed in order to gauge the worst case scenario.

In order to calculate this for a range of speeds, the following assumptions have been made:

- Constant vehicle speed
- Constant radius corner
- Lift forces on vehicle are negligible (see Figure 6.4)
- Drag increase is negligible (see Appendix B)

The following data has been collected throughout this report for the standard Supra:

Given

- Vehicle mass (m) = 1550 kg
- Vehicle speed (V) = 90 mph
= 145 km/h
= 40.3 m/s
- Downforce (F_{aero}) = 294 N

These can then be substituted into Equation 2.7 to determine the normal force.

$$\begin{aligned} N &= mg + F_{aero} \\ &= 1550 \times 9.81 + 294 \\ &= 15499 \text{ Newtons} \end{aligned}$$

Müller et al. (2003) showed that for normal tyres in dry braking conditions, the value of the friction co-efficient can be approximated to:

$$\text{- Friction Coefficient } (\mu) \approx 1$$

This value can then be substituted into Equation 2.6 in order to determine the minimum radius corner that the Supra can travel at through at this speed.

$$\begin{aligned} \mu N &= \frac{mV^2}{R} \\ 1 \times 15499 &= \frac{1550 \times 40.3^2}{R} \\ R &= 162.42 \text{ m} \end{aligned}$$

That data calculated within this project shows that for the same speed, the aerodynamic downforce increases to:

$$\text{- Downforce } (F_{\text{aero}}) = 432 \text{ N}$$

This can then be substituted into Equation 2.7 to determine the normal force.

$$\begin{aligned} N &= mg + F_{\text{aero}} \\ &= 1550 \times 9.81 + 432 \\ &= 15637.5 \text{ Newtons} \end{aligned}$$

This value can then be substituted into Equation 2.6 in order to determine the minimum radius corner that the Supra can travel at through at this speed.

$$\begin{aligned} \mu N &= \frac{mV^2}{R} \\ 1 \times 15637.5 &= \frac{1550 \times 40.3^2}{R} \\ R &= 160.98 \text{ m} \end{aligned}$$

Similarly, a Supra without a wing will have a normal reaction force equivalent directly calculated from mechanical grip only.

$$\begin{aligned}
 N &= mg + F_{aero} \\
 &= 1550 \times 9.81 \\
 &= 15205.5 \text{ Newtons}
 \end{aligned}$$

This value can then be substituted into Equation 2.6 in order to determine the minimum radius corner that the Supra can travel at through at this speed.

$$\begin{aligned}
 \mu N &= \frac{mV^2}{R} \\
 1 \times 15205.5 &= \frac{1550 \times 40.3^2}{R} \\
 R &= 165.55 \text{ m}
 \end{aligned}$$

These results are summarised below in Table 6.2.

Table 6.2 – Minimum Corner Radius Decrease (40.3 m/s)

	Units	No Wing	Stock Wing	TRD Wing
Cornering Speed	(m/s)	40.3	40.3	40.3
Aerodynamic Force	(N)	0	294	432
Minimum Corner Radius	(m)	165.55	162.42	160.98
Radius Decrease	(%)	N/A	1.9	2.8

Similarly calculated results for a vehicle cornering at a much higher speed where aerodynamic effects are more significant is shown below. This analysis can only be performed for two cases, as data is not available for the stock wing at other speeds.

Table 6.3 – Minimum Corner Radius Decrease (70 m/s)

	Units	No Wing	TRD Wing
Cornering Speed	(m/s)	70	70
Aerodynamic Force	(N)	0	1338
Minimum Corner Radius	(m)	499.5	459.1
Radius Decrease	(%)	N/A	8.1

6.3 Material Performance

This section discusses the results of the material testing for both the near field strain analysis and the finite element analysis. It discusses the validity of the results obtained and shows the effect that the full aerodynamic load condition has upon the structural integrity of the wing blade.

6.3.1 Near Field Strain Analysis

The results from loading the wing blade in the P2 laboratory have been tabulated in Appendix D. Each strain gauge worked without error in the final testing phase. A sample test is included below for the most severe loading case tested.

Table 6.4 – Strain Measured Within Wing Blade (55 lb.)

Mass = 55 lb.			
Sensors	dx	dy	dx/dy
1	-42		
2	-480		
3	363	12	232
4	170		
5	170		

The Vishay strain indicator was set up according to the half bridge technique described in Figure 5.5. As the wires for the strain gauges were inserted into ports P+ and S-, the micro strain is shown to be positive when the member is in tension. Sensors 1 and 2 were located on the upper surface of the wing, as described in Figure 5.1. As expected, the gauge has shown that the carbon fibres are being compressed along the x-axis of the wing (from face to face). The value of the micro strain is significantly smaller than the 1000 $\mu\epsilon$ limit advised by Dr Epaarachchi.

Sensors 3, 4 and 5 were located on the underside of the wing, as shown in Figure 5.2. These gauges also demonstrated the expected results, showing the wing fibres were in tension in both the x-axis and the y-axis (leading to trailing edges) of the wing.

6.3.2 Finite Element Analysis

The comparison between the near field strain analysis results and the results from the Strand7 model showed that the actual wing blade was significantly stronger than the computer blade model. When the computer model was loaded with the 55 lb. force along 13 nodes in the centreline, the properties detailed in Figure 5.8 allowed the wing blade model to deform approximately 22 mm downward across the line load axis. This is significantly more deflection than was noticed on the test day.

As such, the material properties of the ply were updated. The glass fibre properties in Figure 5.8 were replaced with properties for carbon fibre, as detailed in the 4th column of Appendix E. Re-modelling of the 55 lb. force distributed across 13 nodes on the top surface of the wing resulted in the following strain plot for the underside of the wing.

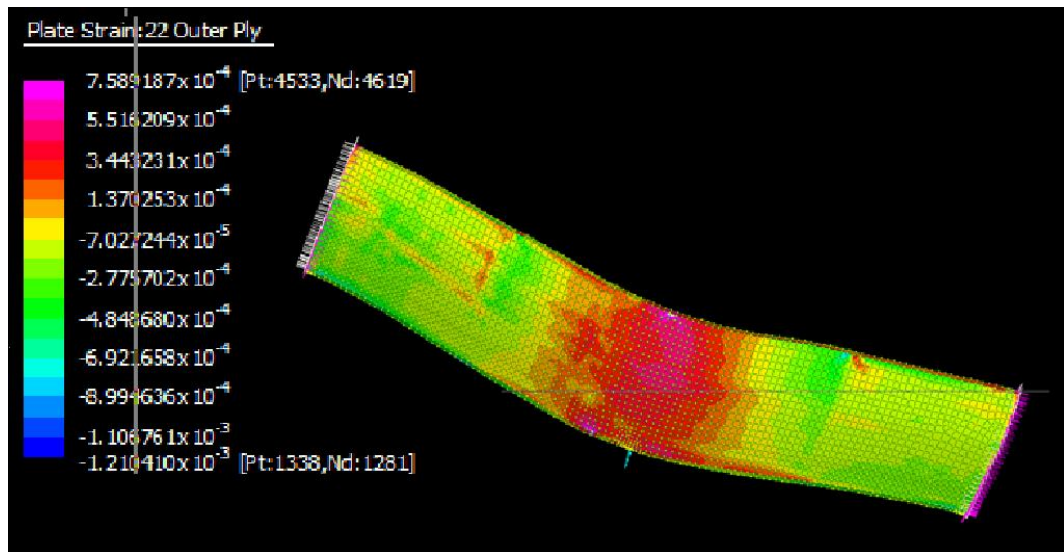


Figure 6.18 – Strand7 Strain Plot (55 lb. Load)

This shows that the results for the underside of the wing are approximately equal to the measured strain from the gauges when the correct, carbon fibre data is used. The leading edge faces up in this plot, which means Gauge 3 is located in the pink-red zone just inside the leading edge. Gauge 4 is located in the yellow-orange zone closer

to the trailing edge. Gauge 5 is located to the left of Gauge 3, within the red-orange-yellow zone. The values of these zones are tabulated below.

Table 6.5 – Strain Comparison of Wing Blades (55 lb.)

Mass = 55 lb.			
Analysis Type	Gauge 3	Gauge 4	Gauge 5
Near Field	363 $\mu\epsilon$	170 $\mu\epsilon$	170 $\mu\epsilon$
Finite Element	380 $\mu\epsilon$	220 $\mu\epsilon$	172 $\mu\epsilon$
Variance (%)	4.7	29.4	1.8

The top side of the wing reflected these values, indicating that the Strand7 solver had analysed the wing as two separate sheets, rather than a rigid beam element. The compression values of strain that were anticipated were not shown, with large amounts of tension strain present. Despite this, the values of strain were close enough on the lower surface in order to justify moving on to the maximum load condition.

A new load case was made to distribute the maximum 1337 N evenly across the 2900 nodes that are used to define the upper wing surface. This brought the individual load force down from 19 Newtons (for the 55 lb. case with 13 nodes) to 0.46 Newtons per node. This resulted in a more equal strain distribution within the wing, with increases in the magnitude of the strain. The new strain profile is shown below in Figure 6.19. It shows that the maximum strain on the underside of the wing is approximately 1000 $\mu\epsilon$, with most sections closer to 200 $\mu\epsilon$.

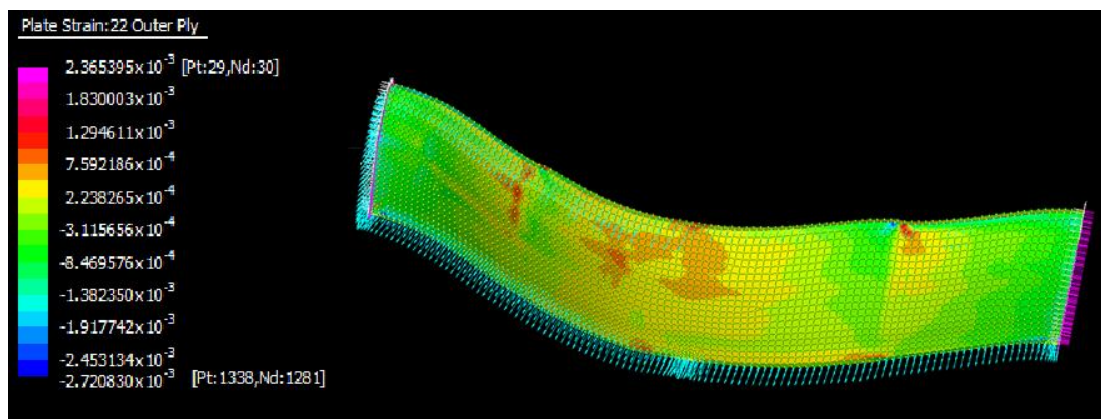


Figure 6.19 – Strand7 Strain Plot (1337 N Load)

The pink areas on certain sections of Figure 6.19 have been attributed to the unrealistic supports in place and as such, they are quite possibly anomalies. Further, more accurate finite element analysis will be needed to confirm this. For the majority of the wing blade, the strains are well within the limits of the carbon fibre material. The only real concern that requires more investigation is the moderate deflection calculated within the Strand7 model. This is shown below in Figure 6.20.

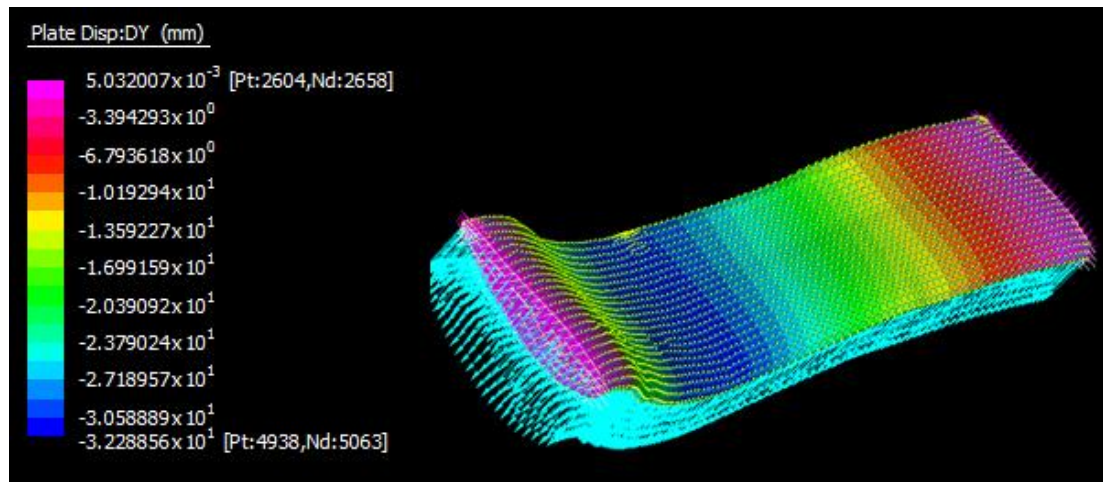


Figure 6.20 – Strand7 Displacement Plot (1337 N Load)

The maximum displacement in the pressure load model occurs at the centreline of the wing blade. According to Strand7, the upper surface would be depressed approximately 30 mm toward the lower surface during the maximum downforce scenario. This deflection is much more severe than any of the deflections observed during the near field strain analysis.

It can be seen that the carbon fibre TRD 3000GT wing blade is well equipped to deal with the added pressures incurred during the steady state loading that occurs at 70 m/s. The strain is well within the experimental limits that were imposed as a measure of ensuring the real blade did not fail. As a result, testing of an alternate material is not warranted at this stage.

7 Conclusion

This project set out to investigate and justify the use of a dynamic rear wing on a Toyota Supra JZA80. The modelling process was conducted in an accurate manner in accordance with objectives A2 and A3 of the Project Specification (Appendix A). Chapter 3 details the limitations which inhibited the use of a 3D model, leading to the adoption of an accurate 2D profile being used.

The detailed literature review clearly indicates why the computational fluid dynamics analysis utilized the realizable $k - \varepsilon$ turbulence model. This model was then implemented on seventeen different wing angle settings at 11 different speeds. The resulting 177 simulations have provided what appear to be accurately calculated component forces for each scenario. These simulations more than satisfy objective A4 of the Project Specification.

Post processing of the simulation data has resulted in the identification of the following critical angles:

Table 7.1 – Summary of Critical Angles

Desired Effect	Critical Angle
Maximum Downforce	-15°
Maximum Drag Force	-60°
Minimum Drag Force	0°

The TRD 3000GT wing produces the most downforce at -15°. At this angle it produces 432 Newtons of downforce at 40 m/s, which is 46.97% more than the standard Toyota Supra wing. At the vehicles maximum speed of 70 m/s, the wing adds 1337 Newtons of downforce. Steady state cornering calculations show that this increase directly results in an increase in vehicle grip, allowing the Supra to perform at a higher standard than a stock vehicle. The evaluation of the effects that increased downforce has on the vehicle satisfies objective B2 of the Project Specification.

At -60° the TRD wing produces the most drag force. The 1085 Newton force at 70 m/s is an increase of 669% over the drag induced by the wing if kept at a static angle of -15° . This massive increase in the drag force correlates to a significant increase in the braking ability of the Supra when travelling at high speeds. This result in itself justifies the use of a dynamic TRD wing on any Toyota Supra that is used in this speed range.

Conversely, when the wing is set at 0° the drag force is at its minimum. When travelling at 70 m/s in a straight line, the wing at this angle will produce 14 Newtons of drag. This is a 90% reduction in the drag induced by a static wing at -15° .

The near field strain analysis results were semi-successfully verified with some locations along the finite element model producing similar results. However further work is needed in this area to be certain that the computer modelling is accurate. This testing, along with the research required in order to perform it, satisfies objectives A5 and A6 of the Project Specification. Despite the doubt around the computer model, all indications suggest that the standard TRD 3000GT carbon fibre wing is capable of withstanding the steady state forces imposed at speeds of up to 70 m/s.

In conclusion, these results conclusively show that static vehicle wings are a compromise between ideal performance levels and that a dynamic wing can allow the vehicle to achieve significant gains by optimising forces for each scenario. The addition of a dynamic rear wing to the Toyota Supra will result in meaningful gains and is therefore recommended for use.

7.2 Further Work

The design stage of this wing is still in its infancy. Now that the computational fluid dynamics confirm that the 2D case produces agreeable results, more work can be done on the 3D case to scope in on the critical wing angles and develop a more rounded understanding of the nature of the vehicle flow field. This would require more sophisticated computers and a completely healed 3D version of the model shown in Figure 3.12.

Once the model is properly refined in a 3D case, the resultant forces should be applied to finite element analysis of the wing blade. Further refining of the FEA model is also required, as not all sections of the blade conform to the experimental data obtained in the near field strain analysis. Dynamic CFD analysis should also be performed on the 3D model to gauge how significant the rise in force magnitude will be when the wing is moving at speed.

Beyond this, the actuation method should be analysed further to allow a prototype to be developed that can adequately function whilst the wing is loaded with a pressure. This will require extensive fibre composite modelling, as the standard wing turrets will need to be modified in order to house the hydraulic pistons.

After this is completed, a software engineer or computer programmer will be required to create control software for the wing. The control device will be required to calculate the vehicle speed from either the odometer cable or the existing front lip control computer.

At the completion of all of these stages, a prototype could be constructed and tested in a closed environment in order to verify the results of the 3D CFD and FEA data.

8 References

- Hucho, W-H 1987, *Aerodynamics of Road Vehicles*, English edn, Butterworths, London.
- Launder, BE & Spalding, DB 1972, *Lectures in Mathematical Models of Turbulence'* Academic Press, London.
- Orszag, SA, Yakhot, V, Flannery, S, Boysan, F, Choudhury, D, Maruzewski, J & Patel, B 1993, *Renormalization Group Modelling and Turbulence Simulations*, Tempe.
- Bakker, A 2006, *Applied Computational Fluid Dynamics*, Dartmouth College, Hanover.
- Shih, TH, Liou, WW, Shabbir, A, Yang, Z & Zhu, J 1995, *A New $k-\epsilon$ Eddy-Viscosity Model for High Reynolds Number Turbulent Flows – Model Development and Validation*.
- Abbott, IH & Von Doenhoff, AE 1959, *Theory of Wing Sections*, Dover, New York.
- Allan, BG, Jones, GS & Lin, JC 2010, '*Reynolds Averaged Navier Stokes Simulation of a 2D Circulation Control Wind Tunnel Experiment*', Langley Research Centre, NASA, Hampton.
- Chandra, S, Lee, A, Gorrell, S & Jensen, G 2011, '*CFD Analysis of PACE Formula-1 Car*', Brigham Young University, Provo.
- Damjanovic, D, Kozak, D, Ivandic, Z & Kokanovic, M 2010, '*Car Design as a new Conceptual Solution and CFD Analysis in Purpose of Improving Aerodynamics*', Mechanical Engineering, University of Osijek, Slavonski.
- Flower, HM 1995, *High Performance Materials in Aerospace*, Chapman & Hall, London.
- Gillespie 1992, *Fundamentals of Vehicle Dynamics*, Society of Automotive Engineers, Warrendale.
- Hibbeler 2010, *Engineering Mechanics Dynamics*, Pearson, Singapore.
- Katz, J 2006, '*Aerodynamics of Race Cars*', Department of Aerospace Engineering, San Diego State University, San Diego.

Mafi, M 2007, '*Investigation of Turbulence Created by Formula One Cars with the Aid of Numerical Fluid Dynamics and Optimisation of Overtaking Potential*', ANSYS, CADFEM User Meeting, Germany.

Powell, KL, Parker, K & Soria, J 2004, '*Flow visualisation of forced flow control over inclined aerofoils*', Mechanical Engineering, Monash University, 15th Australasian Fluid Mechanics Conference, Sydney.

Roumeas, M, Gillieron, P & Kourta, A 2008, '*Drag Reduction By Flow Separation Control on a Car After Body*', Direction de la recherche Renault, Institut de Mecanique de Fluides de Toulouse, Guyancourt.

Savli, M 2012, '*Turbulence Kinetic Energy - TKE*', Faculty of Mathematics and Physics, University of Ljubljana.

Scott-Pomerantz, CD 2004, '*The K-Epsilon Model in the Theory of Turbulence*', Faculty of Arts and Sciences, University of Pittsburgh, Pittsburgh.

Sorensen, B & Damborg, S 1999, '*Mosley's Equations*', *Atlas Formula One Journal*, p. 5.

Wang, Y, Zheng, Z, Sun, M & Zhu, S 2010, '*Finite Element Modelling of Carbon Fiber Reinforced Polymer Vessel*', School of Science, Wuhan Institute of Technology, ICENT, Wuhan.

Wordley, S & Saunders, J 2006, '*Aerodynamics for Formula SAE: Initial Design and Performance Prediction*', Mechanical Engineering, Monash University, Sydney.

Muller, S, Uchanski, M & Hedrick, K 2003, '*Estimation of the Maximum Tire-Road Friction Coefficient*', California

Bugatti.com, 2012, *Technology – Deceleration*, [viewed 18 Oct 2012]
<http://www.bugatti.com/en/veyron-16.4/technology/deceleration.html>

Daimler.com, 2012, *Leaders & Personalities – Alfred Neubauer*, [viewed 18 Oct 2012]
<http://www.daimler.com/dccom/0-5-1333265-1-1279809-1-0-0-1279537-0-0-135-0-0-0-0-0-0-0.html>

Formula1.com, 2012, *Aerodynamics*, [viewed 15 Oct 2012]
http://www.formula1.com/inside_f1/understanding_the_sport/5281.html

Appendix A – Project Specification

PROJECT SPECIFICATION (02/08/12)

For: Douglas Jesshope

Topic: Electronically Controlled Thruster

Supervisor: Dr Jayantha Epaarachchi & Dr Andrew Wandel

Project Objective:

To design a TRD styled dynamic rear wing for a Toyota Supra that optimises down-force and also functions as an airbrake.

A) Methods and Resources:

1. Research general automotive aerodynamics including current active rear wing designs.
2. Obtain or create a dimensionally accurate CAD profile for the Supra
3. Create the TRD-spec rear wing and append to the supra body.
4. Perform aerodynamic simulations on the model to obtain proof of concept (at a minimum)
5. Research the use of lightweight metals and fibre composites in the proposed application and select possible materials.
6. Perform FEA on the wing to in order to justify final material selection.

B) If time permits:

1. Refine the aerodynamic model using real world data
2. Graphically demonstrate the effect of the wing at different speeds and compare to standard model
3. Design a mechanical control system that enables angular transitions

Douglas Jesshope
(Student)

Dr Jayantha Epaarachchi
(Supervisor)

Appendix B – Raw FLUENT Data

Table B-1 – Forces for Speeds 20 m/s to 30 m/s

Wing Angle	Geometry	Velocity (m/s)					
		20		25		30	
		Lift (N)	Drag (N)	Lift (N)	Drag (N)	Lift (N)	Drag (N)
10	Wing	10.96	6.62	16.50	10.23	23.16	14.60
	Body	-805.94	112.57	-1314.28	176.62	-1941.12	254.80
5	Wing	-8.31	0.91	-9.77	7.24	-20.32	9.82
	Body	-913.56	120.27	-1472.75	188.42	-2162.92	271.30
0	Wing	-44.33	1.65	-70.86	2.38	-102.59	3.34
	Body	-726.47	124.25	-1180.25	194.65	-1739.88	280.48
-5	Wing	-70.78	2.48	-111.23	3.80	-160.96	5.38
	Body	-1009.88	132.14	-1625.77	206.85	-2394.38	298.28
-10	Wing	-77.02	6.93	-120.60	10.80	-173.91	15.51
	Body	-1129.06	140.87	-1810.65	220.53	-2661.43	318.06
-15	Wing	-98.50	10.73	-145.65	16.75	-223.63	24.10
	Body	-1059.76	144.67	-1708.16	226.51	-2512.46	326.57
-20	Wing	-90.97	17.95	-142.40	28.22	-205.48	40.81
	Body	-978.65	142.70	-1588.82	223.47	-2327.52	321.76
-25	Wing	-74.56	27.92	-116.51	43.93	-168.01	63.57
	Body	-1117.94	145.14	-1808.39	227.36	-2651.67	327.56
-30	Wing	-73.11	36.67	-114.45	57.50	-165.29	83.03
	Body	-1014.95	148.41	-1633.08	232.24	-2405.46	334.79
-35	Wing	-65.48	43.02	-99.99	65.86	-147.86	97.24
	Body	-1245.59	158.80	-2164.75	252.47	-2937.65	358.16
-40	Wing	-58.12	46.40	-92.66	73.62	-133.49	106.09
	Body	-1222.18	168.14	-1773.25	249.02	-2590.98	358.80
-45	Wing	-48.88	47.03	-75.06	72.19	-107.79	103.57
	Body	-1410.23	197.89	-2229.27	313.42	-3250.76	452.02
-50	Wing	-59.59	65.90	-93.24	103.19	-134.35	148.78
	Body	-1534.17	174.55	-2468.32	273.76	-3622.99	394.99
-60	Wing	-53.23	81.20	-83.32	127.16	-120.14	183.42
	Body	-1572.28	178.23	-2527.37	279.32	-3710.15	402.91
-70	Wing	-31.04	71.46	-47.74	111.11	-67.90	160.17
	Body	-1707.72	217.78	-2804.44	354.79	-4117.84	509.41
-80	Wing	-20.66	76.74	-32.14	119.97	-46.56	173.37
	Body	-1670.20	222.85	-2686.06	355.90	-3914.87	505.58

Table B-2 – Forces for Speeds 35 m/s to 45 m/s

Wing Angle	Geometry	Velocity (m/s)					
		35		40		45	
		Lift (N)	Drag (N)	Lift (N)	Drag (N)	Lift (N)	Drag (N)
10	Wing	30.62	19.70	39.58	25.61	49.09	32.21
	Body	-2718.54	347.77	-3632.46	455.08	-4692.05	576.90
5	Wing	-32.69	12.83	-44.71	16.50	-60.57	20.42
	Body	-3033.02	370.34	-4030.07	484.30	-5196.76	613.93
0	Wing	-141.50	4.30	-186.85	5.35	-238.20	6.54
	Body	-2417.44	382.14	-3211.61	499.45	-4143.82	632.73
-5	Wing	-219.43	7.32	-287.78	9.41	-365.37	11.78
	Body	-3220.72	404.44	-4287.78	529.01	-5489.48	669.83
-10	Wing	-237.41	21.06	-310.09	27.46	-393.32	34.69
	Body	-3689.88	433.60	-4886.36	566.89	-6257.94	717.92
-15	Wing	-305.43	32.78	-400.08	42.79	-507.63	54.13
	Body	-3484.15	445.02	-4621.70	581.80	-5923.92	736.84
-20	Wing	-280.11	55.79	-366.59	73.06	-464.94	92.69
	Body	-3264.87	438.86	-4346.09	573.74	-5591.27	726.75
-25	Wing	-228.99	86.84	-299.57	113.75	-379.80	144.32
	Body	-3677.92	446.36	-4865.30	583.23	-6270.19	739.33
-30	Wing	-225.72	113.21	-295.63	148.04	-375.26	187.60
	Body	-3324.50	455.97	-4418.03	596.22	-5769.46	757.57
-35	Wing	-196.81	129.64	-257.46	169.59	-326.48	215.01
	Body	-4453.46	497.26	-5922.64	650.66	-7597.67	825.40
-40	Wing	-181.81	144.53	-237.44	188.81	-300.55	239.02
	Body	-3570.53	488.82	-4710.69	638.21	-6013.70	808.57
-45	Wing	-146.79	140.98	-191.85	184.25	-243.04	233.37
	Body	-4484.84	616.70	-5920.14	804.70	-7560.93	1017.26
-50	Wing	-182.99	202.73	-239.06	265.04	-302.68	335.65
	Body	-5033.99	539.31	-6676.56	705.96	-8554.46	895.02
-60	Wing	-163.66	249.94	-213.90	326.76	-270.92	414.06
	Body	-5152.77	548.98	-6766.42	717.64	-8672.08	909.79
-70	Wing	-92.18	218.52	-120.94	286.40	-152.77	362.27
	Body	-5601.95	672.54	-7360.14	873.55	-9439.36	1106.10
-80	Wing	-62.61	235.52	-79.52	305.78	-99.94	387.59
	Body	-5459.69	702.92	-7305.07	928.11	-9361.68	1178.66

Table B-3 – Forces for Speeds 50 m/s to 60 m/s

Wing Angle	Geometry	Velocity (m/s)					
		50		55		60	
		Lift (N)	Drag (N)	Lift (N)	Drag (N)	Lift (N)	Drag (N)
10	Wing	59.59	39.55	70.72	47.59	83.62	56.46
	Body	-5875.29	712.76	-7222.29	863.39	-8693.99	1027.88
5	Wing	-76.19	24.98	-93.34	30.01	-113.43	35.38
	Body	-6508.83	758.62	-7967.47	918.41	-9607.11	1093.92
0	Wing	-295.34	7.83	-363.10	8.83	-434.63	10.16
	Body	-5158.23	780.74	-6364.11	946.04	-7659.33	1125.94
-5	Wing	-452.42	14.38	-548.68	17.23	-654.55	20.30
	Body	-6846.66	827.12	-8369.43	1001.10	-10083.22	1192.23
-10	Wing	-485.28	42.79	-588.23	51.69	-700.25	61.44
	Body	-7802.01	886.63	-9528.43	1073.23	-11467.10	1278.25
-15	Wing	-627.98	66.78	-761.26	80.76	-907.51	96.07
	Body	-7405.06	910.35	-9057.27	1102.14	-10877.59	1312.04
-20	Wing	-575.03	114.64	-697.08	139.00	-830.85	165.67
	Body	-6994.83	897.71	-8588.87	1087.08	-10313.25	1293.57
-25	Wing	-469.79	178.57	-569.35	216.43	-677.96	257.79
	Body	-7852.18	913.61	-9653.82	1107.12	-11619.02	1318.54
-30	Wing	-464.06	231.77	-562.66	280.67	-671.04	334.32
	Body	-7115.82	933.53	-8714.20	1130.44	-10479.60	1345.94
-35	Wing	-403.27	265.54	-488.52	321.59	-580.95	382.36
	Body	-9525.09	1019.51	-11659.9	1234.83	-14104.66	1472.95
-40	Wing	-327.17	260.55	-449.30	357.19	-534.97	425.25
	Body	-5807.80	934.90	-9089.99	1205.73	-10881.76	1434.89
-45	Wing	-300.12	288.07	-365.56	349.56	-437.32	417.95
	Body	9437.36	1260.63	-11523.2	1532.30	-13690.83	1800.28
-50	Wing	-373.96	414.68	-452.52	501.94	-538.50	597.43
	Body	-10765.9	1109.20	-13059.7	1341.22	-15612.71	1596.04
-60	Wing	-334.62	511.52	-405.10	619.36	-482.26	737.46
	Body	-10834.7	1124.92	-13255.5	1363.30	-15909.75	1623.94
-70	Wing	-188.81	447.90	-233.24	545.31	-281.03	650.36
	Body	-11774.2	1367.49	-14097.1	1620.33	-16923.69	1940.48
-80	Wing	-123.74	478.64	-149.43	580.72	-176.48	689.95
	Body	-11654.6	1450.46	-14203.6	1758.61	-16935.34	2065.29

Table B-4 – Forces for Speeds 65 m/s to 70 m/s

Wing Angle	Geometry	Velocity (m/s)			
		65		70	
		Lift (N)	Drag (N)	Lift (N)	Drag (N)
10	Wing	97.19	66.03	111.69	76.33
	Body	-10308.00	1206.67	-12068.78	1399.68
5	Wing	-134.69	41.25	-154.54	47.89
	Body	-11384.12	1284.08	-13243.53	1488.02
0	Wing	-512.17	11.62	-596.10	13.17
	Body	-9113.37	1322.15	-10647.55	1532.84
-5	Wing	-769.64	23.63	-894.44	27.16
	Body	-11927.43	1399.30	-13955.42	1623.36
-10	Wing	-822.31	72.04	-954.14	83.45
	Body	-13557.93	1500.34	-15843.04	1740.56
-15	Wing	-1066.67	112.69	-1238.80	130.64
	Body	-12876.06	1540.13	-15032.78	1786.53
-20	Wing	-976.54	194.70	-1134.09	226.04
	Body	-12199.43	1517.75	-14124.41	1757.54
-25	Wing	-796.72	302.90	-925.04	351.58
	Body	-13732.90	1547.31	-16015.26	1794.08
-30	Wing	-788.59	392.47	-916.18	455.44
	Body	-12451.57	1581.25	-14522.06	1833.52
-35	Wing	-682.46	449.04	-792.31	521.18
	Body	-16702.66	1730.28	-19512.60	2007.81
-40	Wing	-553.89	441.21	-604.86	483.89
	Body	-9982.99	1579.55	-10858.99	1826.61
-45	Wing	-506.94	486.82	-600.76	571.31
	Body	-16343.34	2135.57	-18929.76	2474.82
-50	Wing	-632.02	701.23	-732.84	813.22
	Body	-18513.66	1876.37	-21565.12	2176.16
-60	Wing	-566.18	895.90	-656.99	1004.93
	Body	-18781.54	1906.60	-21977.75	2214.38
-70	Wing	-329.46	760.49	-378.79	880.22
	Body	-20352.72	2361.68	-24019.18	2785.03
-80	Wing	-207.50	813.07	-243.53	948.91
	Body	-19866.70	2375.51	-22961.94	2717.78

Appendix C – Development of Forces per Velocity

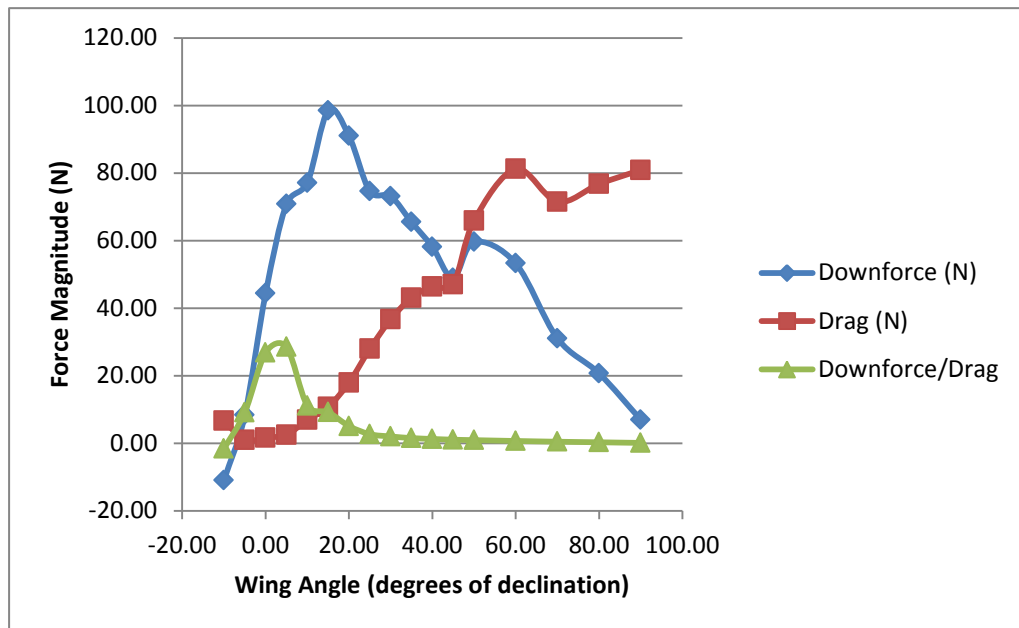


Figure C-1 – Aerodynamic Forces versus Vehicle Speed (20 m/s)

Wing Angle	Downforce (N)	Drag (N)	Downforce/Drag
-10.00	-10.96	6.62	-1.66
-5.00	8.31	0.91	9.13
0.00	44.33	1.65	26.80
5.00	70.78	2.48	28.54
10.00	77.02	6.93	11.11
15.00	98.50	10.73	9.18
20.00	90.97	17.95	5.07
25.00	74.56	27.92	2.67
30.00	73.11	36.67	1.99
35.00	65.48	43.02	1.52
40.00	58.12	46.40	1.25
45.00	48.88	47.03	1.04
50.00	59.59	65.90	0.90
60.00	53.23	81.20	0.66
70.00	31.04	71.46	0.43
80.00	20.66	76.74	0.27
90.00	6.95	80.90	0.09

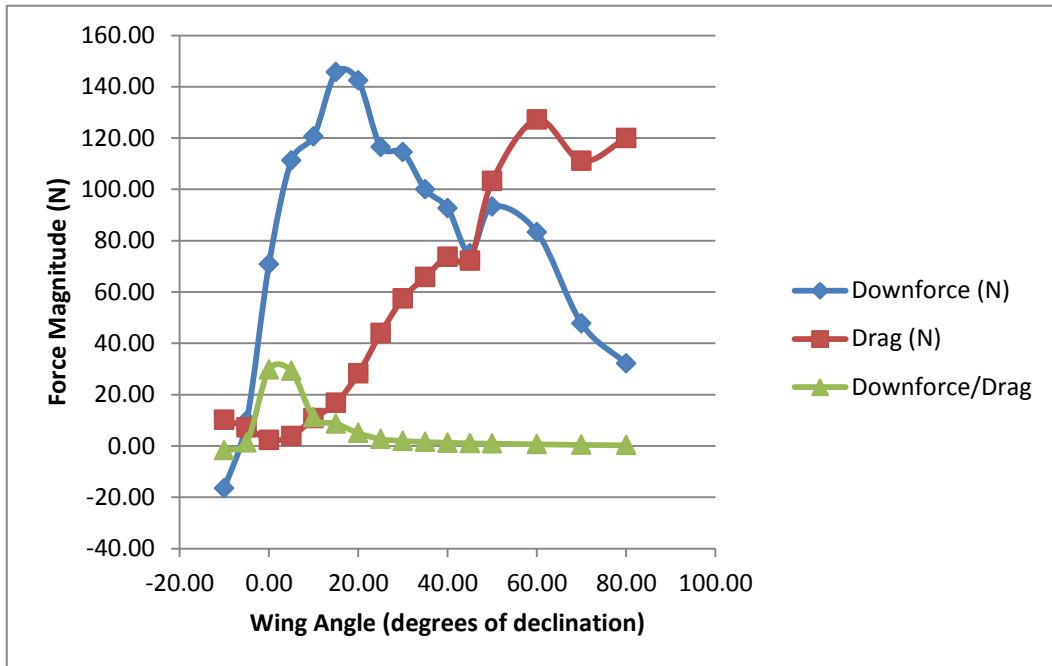


Figure C-2 – Aerodynamic Forces versus Vehicle Speed (25 m/s)

Table C-2 Vehicle Velocity = 25m/s			
Wing Angle	Downforce (N)	Drag (N)	Downforce/Drag
-10.00	-16.50	10.23	-1.61
-5.00	9.77	7.24	1.35
0.00	70.86	2.38	29.77
5.00	111.23	3.80	29.27
10.00	120.60	10.80	11.17
15.00	145.65	16.75	8.70
20.00	142.40	28.22	5.05
25.00	116.51	43.93	2.65
30.00	114.45	57.50	1.99
35.00	99.99	65.86	1.52
40.00	92.66	73.62	1.26
45.00	75.06	72.19	1.04
50.00	93.24	103.19	0.90
60.00	83.32	127.16	0.66
70.00	47.74	111.11	0.43
80.00	32.14	119.97	0.27

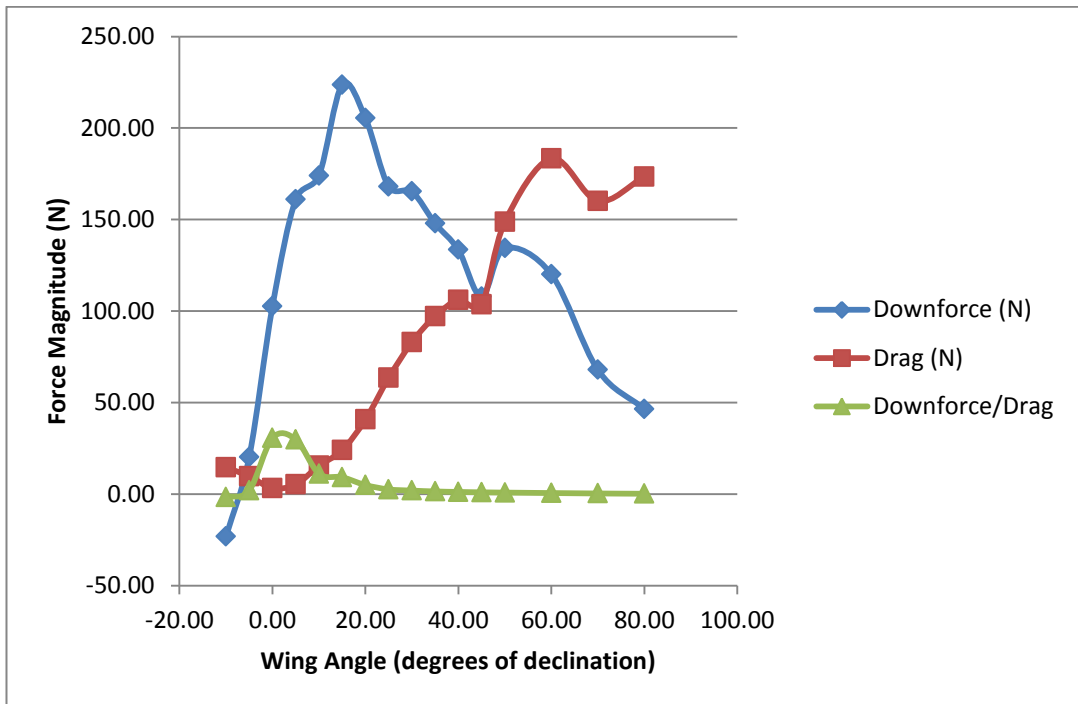


Figure C-3 – Aerodynamic Forces versus Vehicle Speed (30 m/s)

Table C-3 Vehicle Velocity = 30m/s			
Wing Angle	Downforce (N)	Drag (N)	Downforce/Drag
-10.00	-23.16	14.60	-1.59
-5.00	20.32	9.82	2.07
0.00	102.59	3.34	30.72
5.00	160.96	5.38	29.92
10.00	173.91	15.51	11.21
15.00	223.63	24.10	9.28
20.00	205.48	40.81	5.04
25.00	168.01	63.57	2.64
30.00	165.29	83.03	1.99
35.00	147.86	97.24	1.52
40.00	133.49	106.09	1.26
45.00	107.79	103.57	1.04
50.00	134.35	148.78	0.90
60.00	120.14	183.42	0.65
70.00	67.90	160.17	0.42
80.00	46.56	173.37	0.27

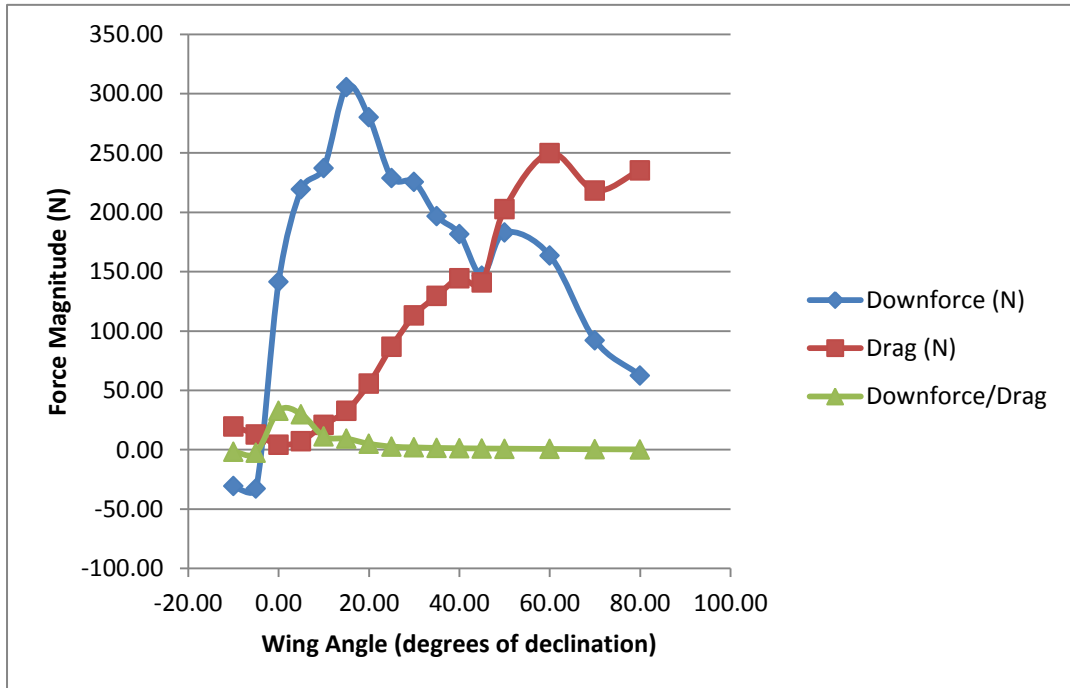


Figure C-4 – Aerodynamic Forces versus Vehicle Speed (35 m/s)

Table C-4 Vehicle Velocity = 35m/s			
Wing Angle	Downforce (N)	Drag (N)	Downforce/Drag
-10.00	-30.62	19.70	-1.55
-5.00	-32.69	12.83	-2.55
0.00	141.50	4.30	32.91
5.00	219.43	7.32	29.98
10.00	237.41	21.06	11.27
15.00	305.43	32.78	9.32
20.00	280.11	55.79	5.02
25.00	228.99	86.84	2.64
30.00	225.72	113.21	1.99
35.00	196.81	129.64	1.52
40.00	181.81	144.53	1.26
45.00	146.79	140.98	1.04
50.00	182.99	202.73	0.90
60.00	163.66	249.94	0.65
70.00	92.18	218.52	0.42
80.00	62.61	235.52	0.27

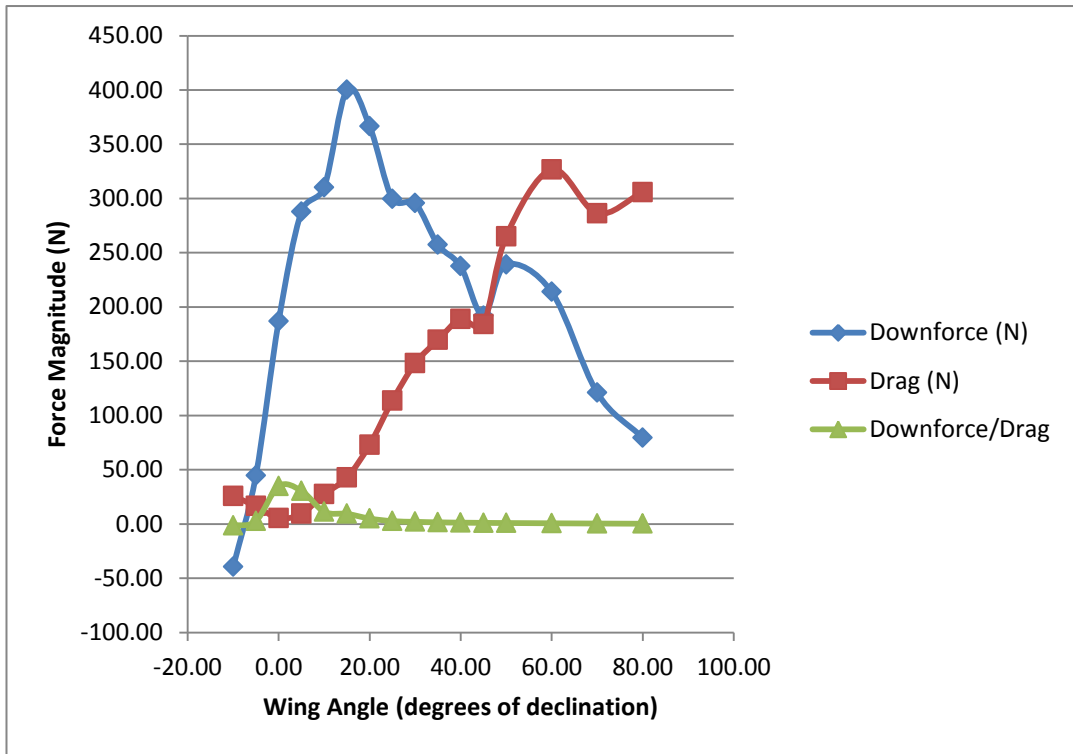


Figure C-5 – Aerodynamic Forces versus Vehicle Speed (40 m/s)

Table C-5 Vehicle Velocity = 40 m/s			
Wing Angle	Downforce (N)	Drag (N)	Downforce/Drag
-10.00	-39.58	25.61	-1.55
-5.00	44.71	16.50	2.71
0.00	186.85	5.35	34.93
5.00	287.78	9.41	30.58
10.00	310.09	27.46	11.29
15.00	400.08	42.79	9.35
20.00	366.59	73.06	5.02
25.00	299.57	113.75	2.63
30.00	295.63	148.04	2.00
35.00	257.46	169.59	1.52
40.00	237.44	188.81	1.26
45.00	191.85	184.25	1.04
50.00	239.06	265.04	0.90
60.00	213.90	326.76	0.65
70.00	120.94	286.40	0.42
80.00	79.52	305.78	0.26

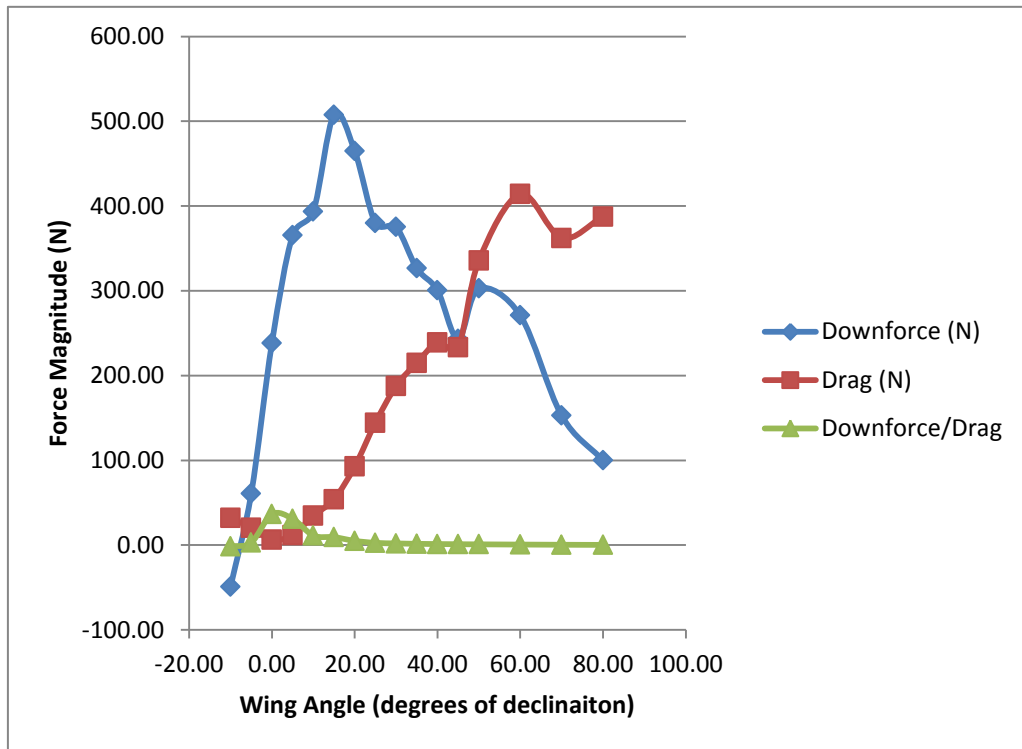


Figure C-6 – Aerodynamic Forces versus Vehicle Speed (45 m/s)

Wing Angle	Downforce (N)	Drag (N)	Downforce/Drag
-10.00	-49.09	32.21	-1.52
-5.00	60.57	20.42	2.97
0.00	238.20	6.54	36.42
5.00	365.37	11.78	31.02
10.00	393.32	34.69	11.34
15.00	507.63	54.13	9.38
20.00	464.94	92.69	5.02
25.00	379.80	144.32	2.63
30.00	375.26	187.60	2.00
35.00	326.48	215.01	1.52
40.00	300.55	239.02	1.26
45.00	243.04	233.37	1.04
50.00	302.68	335.65	0.90
60.00	270.92	414.06	0.65
70.00	152.77	362.27	0.42
80.00	99.94	387.59	0.26

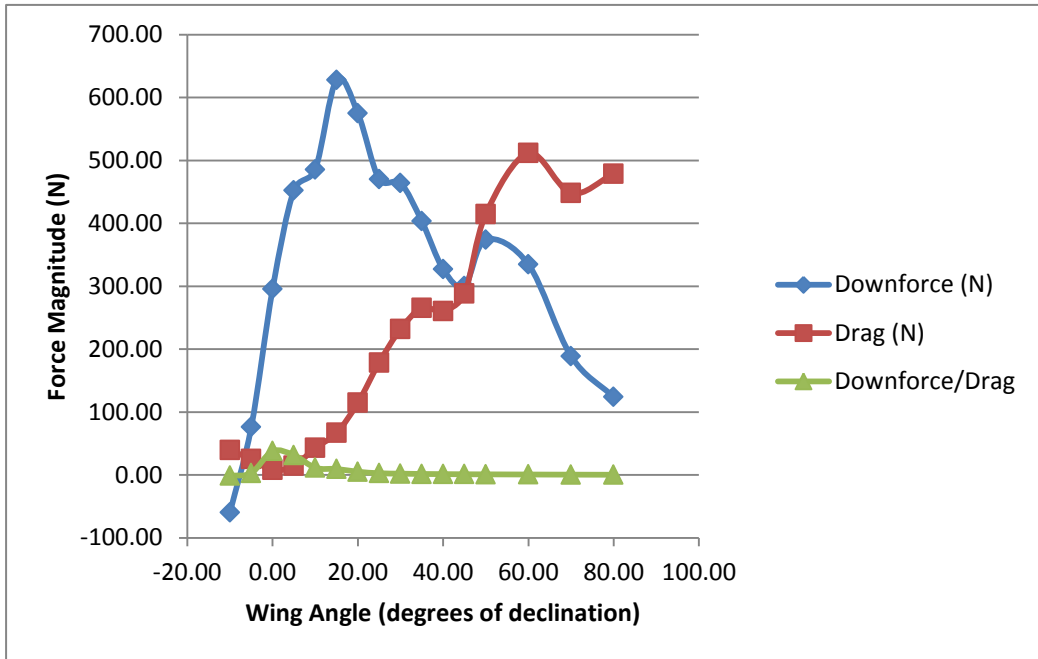


Figure C-7 – Aerodynamic Forces versus Vehicle Speed (50 m/s)

Wing Angle	Downforce (N)	Drag (N)	Downforce/Drag
-10.00	-59.59	39.55	-1.51
-5.00	76.19	24.98	3.05
0.00	295.34	7.83	37.72
5.00	452.42	14.38	31.46
10.00	485.28	42.79	11.34
15.00	627.98	66.78	9.40
20.00	575.03	114.64	5.02
25.00	469.79	178.57	2.63
30.00	464.06	231.77	2.00
35.00	403.27	265.54	1.52
40.00	327.17	260.55	1.26
45.00	300.12	288.07	1.04
50.00	373.96	414.68	0.90
60.00	334.62	511.52	0.65
70.00	188.81	447.90	0.42
80.00	123.74	478.64	0.26

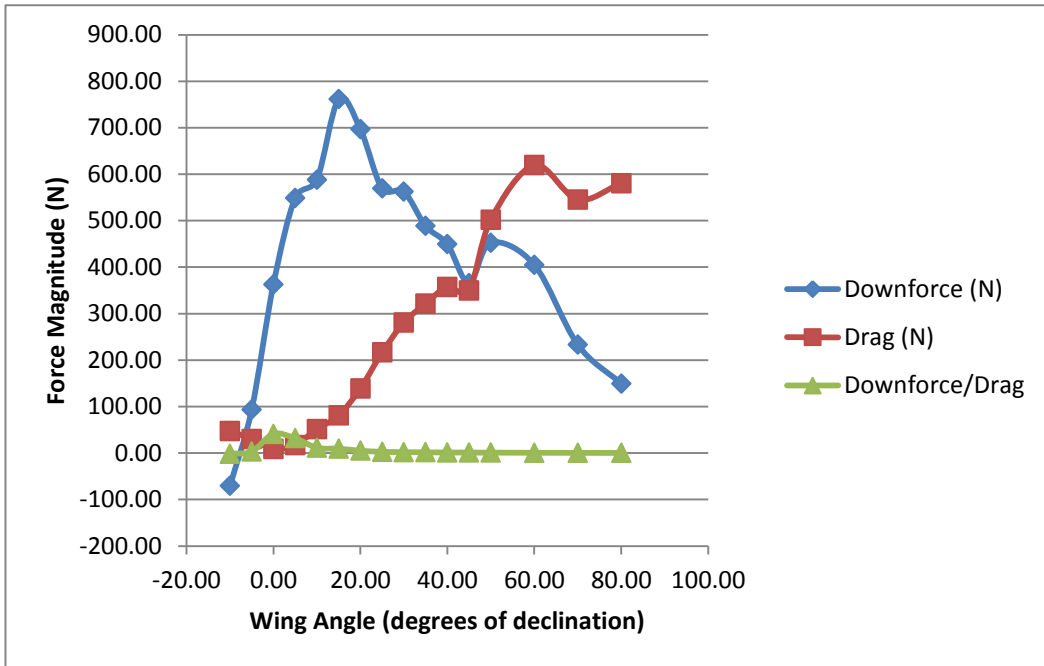


Figure C-8 – Aerodynamic Forces versus Vehicle Speed (55 m/s)

Wing Angle	Downforce (N)	Drag (N)	Downforce/Drag
-10.00	-70.72	47.59	-1.49
-5.00	93.34	30.01	3.11
0.00	363.10	8.83	41.12
5.00	548.68	17.23	31.84
10.00	588.23	51.69	11.38
15.00	761.26	80.76	9.43
20.00	697.08	139.00	5.01
25.00	569.35	216.43	2.63
30.00	562.66	280.67	2.00
35.00	488.52	321.59	1.52
40.00	449.30	357.19	1.26
45.00	365.56	349.56	1.05
50.00	452.52	501.94	0.90
60.00	405.10	619.36	0.65
70.00	233.24	545.31	0.43
80.00	149.43	580.72	0.26

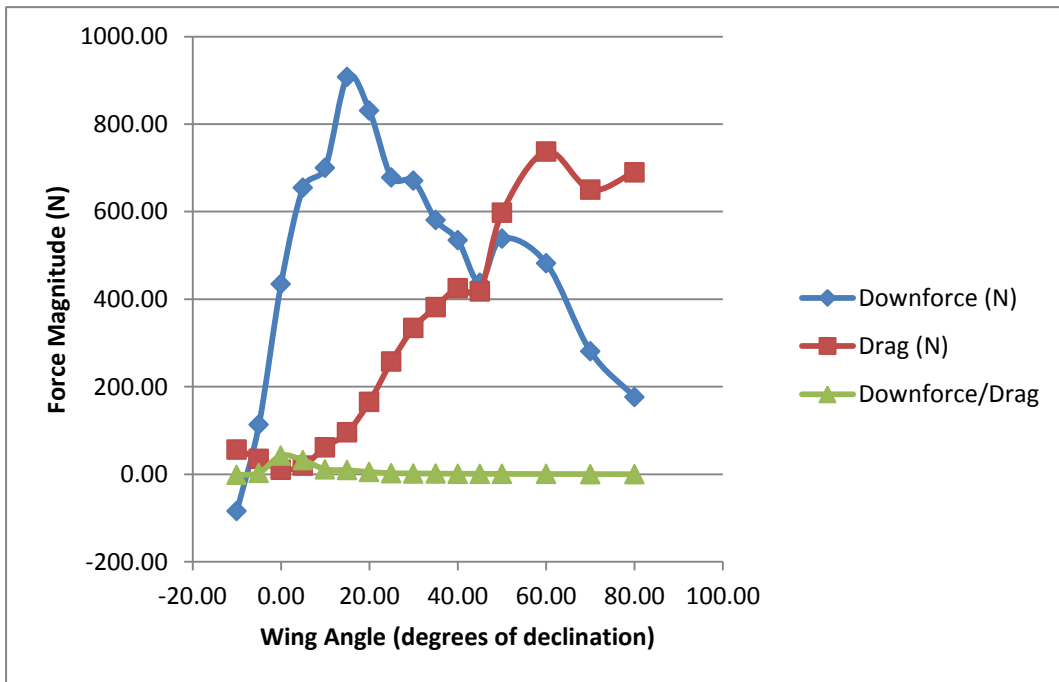


Figure C-9 – Aerodynamic Forces versus Vehicle Speed (60 m/s)

Table C-9 Vehicle Velocity = 60 m/s			
Wing Angle	Downforce (N)	Drag (N)	Downforce/Drag
-10.00	-83.62	56.46	-1.48
-5.00	113.43	35.38	3.21
0.00	434.63	10.16	42.78
5.00	654.55	20.30	32.24
10.00	700.25	61.44	11.40
15.00	907.51	96.07	9.45
20.00	830.85	165.67	5.02
25.00	677.96	257.79	2.63
30.00	671.04	334.32	2.01
35.00	580.95	382.36	1.52
40.00	534.97	425.25	1.26
45.00	437.32	417.95	1.05
50.00	538.50	597.43	0.90
60.00	482.26	737.46	0.65
70.00	281.03	650.36	0.43
80.00	176.48	689.95	0.26

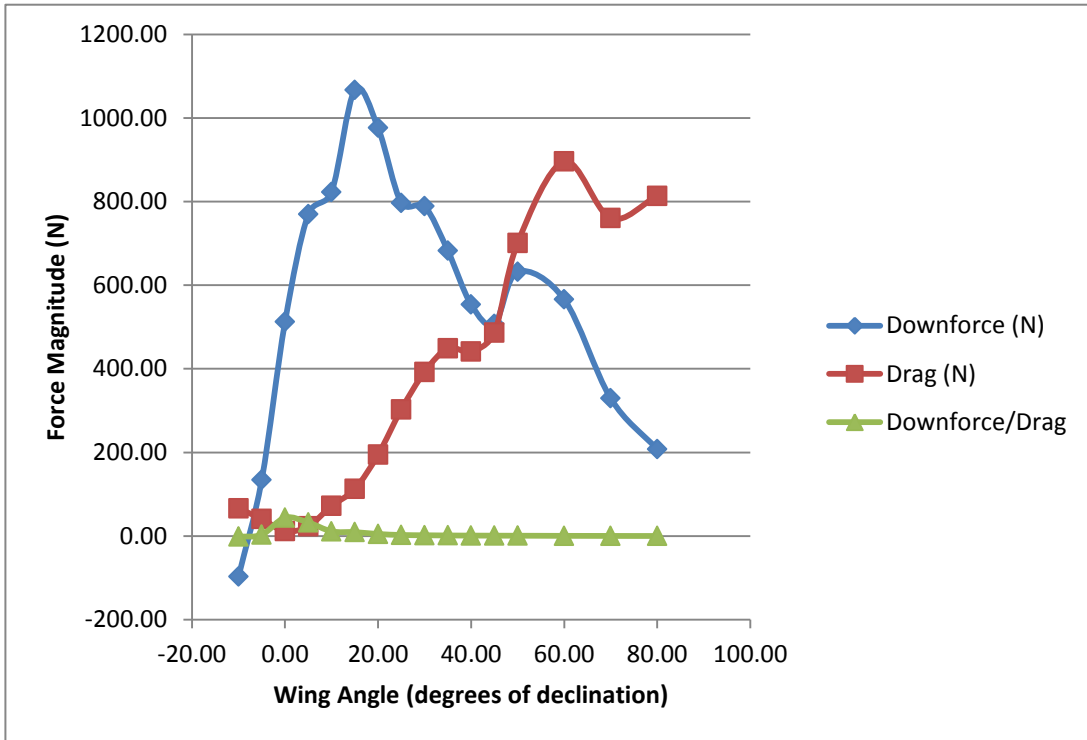


Figure C-10 – Aerodynamic Forces versus Vehicle Speed (65 m/s)

Wing Angle	Downforce (N)	Drag (N)	Downforce/Drag
-10.00	-97.19	66.03	-1.47
-5.00	134.69	41.25	3.27
0.00	512.17	11.62	44.08
5.00	769.64	23.63	32.57
10.00	822.31	72.04	11.41
15.00	1066.67	112.69	9.47
20.00	976.54	194.70	5.02
25.00	796.72	302.90	2.63
30.00	788.59	392.47	2.01
35.00	682.46	449.04	1.52
40.00	553.89	441.21	1.26
45.00	506.94	486.82	1.04
50.00	632.02	701.23	0.90
60.00	566.18	895.90	0.63
70.00	329.46	760.49	0.43
80.00	207.50	813.07	0.26

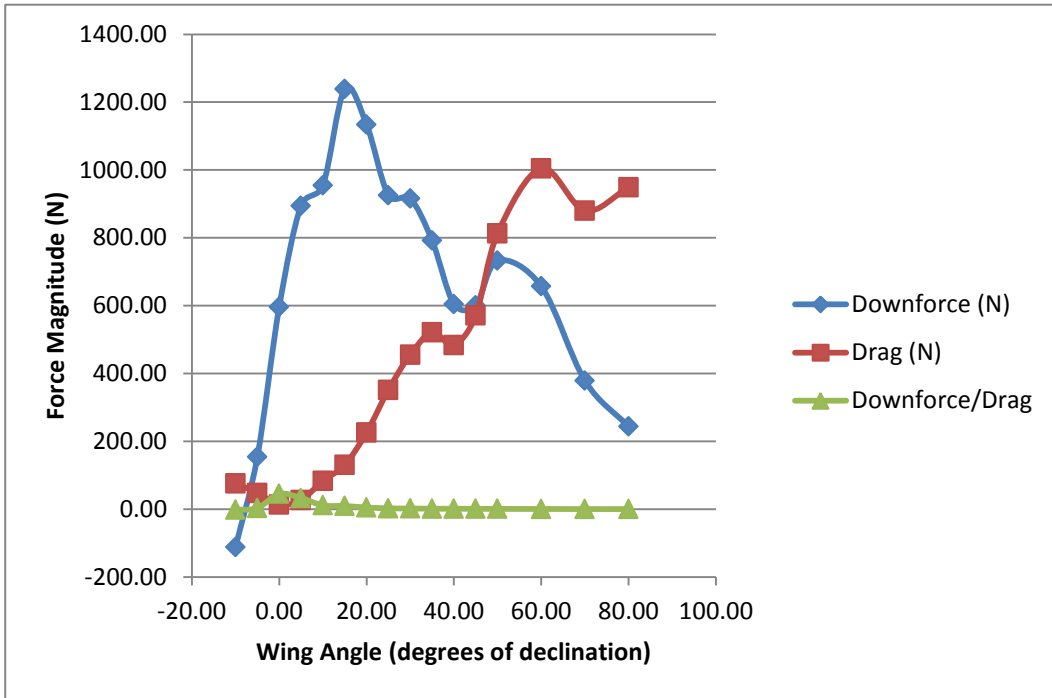


Figure C-11 – Aerodynamic Forces versus Vehicle Speed (70 m/s)

Wing Angle	Downforce (N)	Drag (N)	Downforce/Drag
-10.00	-111.69	76.33	-1.46
-5.00	154.54	47.89	3.23
0.00	596.10	13.17	45.26
5.00	894.44	27.16	32.93
10.00	954.14	83.45	11.43
15.00	1238.80	130.64	9.48
20.00	1134.09	226.04	5.02
25.00	925.04	351.58	2.63
30.00	916.18	455.44	2.01
35.00	792.31	521.18	1.52
40.00	604.86	483.89	1.25
45.00	600.76	571.31	1.05
50.00	732.84	813.22	0.90
60.00	656.99	1004.93	0.65
70.00	378.79	880.22	0.43
80.00	243.53	948.91	0.26

Appendix D – Near Field Strain Results

Table D-1 – Strain Measured versus Applied Load

Mass	Sensors	Measured Strain ($\mu\epsilon$)		
		dx	dy	dx/dy
5 lb.	1	-5		
	2	-40		
	3	33	0	20
	4	25		
	5	17		
10 lb.	1	-10		
	2	-79		
	3	68	1	48
	4	46		
	5	28		
15 lb.	1	-11		
	2	-118		
	3	101	5	72
	4	66		
	5	43		
20 lb.	1	0		
	2	-157		
	3	132	5	97
	4	88		
	5	46		
25 lb.	1	-10		
	2	-201		
	3	169	0	120
	4	92		
	5	62		
30 lb.	1	-15		
	2	-242		
	3	207	0	141
	4	105		
	5	84		
35 lb.	1	-19		
	2	-285		
	3	242	-1	159
	4	112		
	5	101		

Mass	Sensors	Measured Strain ($\mu\epsilon$)		
		dx	dy	dx/dy
40 lb.	1	-26		
	2	-322		
	3	267	2	186
	4	124		
	5	117		
45 lb.	1	-30		
	2	-377		
	3	298	5	192
	4	144		
	5	141		
50 lb.	1	-35		
	2	-430		
	3	330	10	210
	4	162		
	5	155		
55 lb.	1	-42		
	2	-480		
	3	363	12	232
	4	170		
	5	170		

Appendix E – Fibre Composite Properties



Mechanical Properties of Carbon Fibre Composite Materials, Fibre / Epoxy resin (120°C Cure)

Fibres @ 0° (UD), 0/90° (fabric) to loading axis, Dry, Room Temperature, Vf = 60% (UD), 50% (fabric)

	Symbol	Units	Std CF Fabric	HMCF Fabric	E glass Fabric	Kevlar Fabric	Std CF UD	HMCF UD	M55** UD	E glass UD	Kevlar UD	Boron UD	Steel 597	Al. L65	Tit. dtd 5173
Young's Modulus 0°	E1	GPa	70	85	25	30	135	175	300	40	75	200	207	72	110
Young's Modulus 90°	E2	GPa	70	85	25	30	10	8	12	8	6	15	207	72	110
In-plane Shear Modulus	G12	GPa	5	5	4	5	5	5	5	4	2	5	80	25	
Major Poisson's Ratio	v12		0.10	0.10	0.20	0.20	0.30	0.30	0.30	0.25	0.34	0.23			
Ult. Tensile Strength 0°	Xt	MPa	600	350	440	480	1500	1000	1600	1000	1300	1400	990	460	
Ult. Comp. Strength 0°	Xc	MPa	570	150	425	190	1200	850	1300	600	280	2800			
Ult. Tensile Strength 90°	Yt	MPa	600	350	440	480	50	40	50	30	30	90			
Ult. Comp. Strength 90°	Yc	MPa	570	150	425	190	250	200	250	110	140	280			
Ult. In-plane Shear Stren.	S	MPa	90	35	40	50	70	60	75	40	60	140			
Ult. Tensile Strain 0°	ext	%	0.85	0.40	1.75	1.60	1.05	0.55		2.50	1.70	0.70			
Ult. Comp. Strain 0°	exc	%	0.80	0.15	1.70	0.60	0.85	0.45		1.50	0.35	1.40			
Ult. Tensile Strain 90°	eyt	%	0.85	0.40	1.75	1.60	0.50	0.50		0.35	0.50	0.60			
Ult. Comp. Strain 90°	eyc	%	0.80	0.15	1.70	0.60	2.50	2.50		1.35	2.30	1.85			
Ult. In-plane shear strain	es	%	1.80	0.70	1.00	1.00	1.40	1.20		1.00	3.00	2.80			
Thermal Exp. Co-ef. 0°	Alpha1	Strain/K	2.10	1.10	11.60	7.40	-0.30	-0.30	-0.30	6.00	4.00	18.00			
Thermal Exp. Co-ef. 90°	Alpha2	Strain/K	2.10	1.10	11.60	7.40	28.00	25.00	28.00	35.00	40.00	40.00			
Moisture Exp. Co-ef 0°	Beta1	Strain/K	0.03	0.03	0.07	0.07	0.01	0.01		0.01	0.04	0.01			
Moisture Exp. Co-ef 90°	Beta2	Strain/K	0.03	0.03	0.07	0.07	0.30	0.30		0.30	0.30	0.30			
Density		g/cc	1.60	1.60	1.90	1.40	1.60	1.60	1.65	1.90	1.40	2.00			

** Calculated figures

Figure E-1 – Carbon Fibre Properties (performance-composites.com)